ELECTRONIC AND MAGNETIC PROPERTIES OF LAYERED TWO-DIMENSIONAL MATERIALS

by

CHRISTOPHER MEDARD PASCO

A dissertation submitted to Johns Hopkins University in conformity with the requirements for the degree of Doctor of Philosophy

Baltimore, Maryland

January, 2021

Abstract

Two-dimensional materials have recently become an area of considerable interest in the materials science community for both having a variety of properties that can be exploited for the production of devices, and for their potential to host exotic states, especially when combined with magnetism. This work focuses on the synthesis and characterization of two different families of two-dimensional materials, the kagomé layered quantum spin liquid host candidate barlowite, $Cu_{4-x}Zn_x(OH)_6BrF$, and the Van der Waals layered trimerized kagomé paramagnets Nb_3X_8 (X = Cl, Br). In the case of barlowite it was found that while the parent compound was not as geometrically perfect as had been previously assumed, but zinc doping showed promise for hosting a QSL state despite the deviations from perfect hexagonal symmetry. In the Nb_3X_8 family it was discovered that the bromide, like the chloride underwent the same layer rearrangement transition between a paramagnet and a singlet ground state, but above room temperature. Further work revealed that the transition temperature could be tuned between those of the end members by the solid solution $Nb_3Cl_{8-x}Br_x$.

Readers: Collin Broholm, Tyrel McQueen

Dissertation committee

Advisor Professor Collin Broholm

Advisor Professor Tyrel M. McQueen

Professor Kit H. Bowen

Acknowledgements

I would like to thank the people who made this work possible. This includes my Ph D. advisors Professor Collin Broholm and Professor Tyrel McQueen, who have both provided advice and support over the years. In addition I would like to thank my collaborators, without whom much of my work may not have been possible Ben Trump, Thao Tran, Zach Kelly, Christina Hoffman, Ivo Heinmaa, Ravio Stern, Ismail El Baggari, Elisabeth Bianco, Lena F. Kourkouis.

Without a good group of people around you, it would be quite difficult to deal with the stress of graduate school, so I would also like to thank both the members of the McQueen and Broholm groups. Keep up the good work. Finally, I would like to thank my family for their support over the years.

Table of Contents

List of Tables

List of Figures

1. Introduction

1.1 Introduction

Solid-state chemistry is the study of the synthesis, structure and physical properties of extended solid phase materials. These materials typically are non-molecular, consisting of repeating lattices, allowing a greater degree of interaction and on larger scales than generally observed in other areas of chemistry. These interactions result in far more complicated ground states that can yield emergent properties, which ultimately make up the basis for many of the technologies of the modern age. Materials scientists generally attempt to create novel materials, or characterize existing materials to further explore the emergent physics observed in solid state materials.

New technologies often result from the exploitation of novel materials that express known physics in a useful way, the discovery of novel physics in known materials, or the development of new materials with previously unknown physics. Historically many examples of novel physics have been discovered by accident, quite often in previously known materials, as technologies to perform characterization became more sophisticated allowing examinations of materials under new conditions. An example of this is the discovery of superconductivity which occurred in 1911 when attempts were made to determine what would happen to the resistivity of mercury as temperatures approached zero kelvin and it was found that unexpectedly resistances dropped to zero at the finite temperature of 4.19

K. The observation of superconductivity in mercury was only made possible by the development of a technique to liquify helium which occurred in 1908. This discovery then lead to decades of research into other superconductors which continues to this day, as well as a host of new technologies such as MRIs and superconducting Josephson junctions which are used in SQUIDs (superconducting quantum interference devices) which make much of the magnetic properties characterization that we now have access to possible.

With advances in both theoretical frameworks built off of our understanding of quantum mechanical systems and computational power, it has become possible to predict novel physics, and then attempt to identify and synthesize real materials which could host those novel states. An example here is the quantum spin liquid ground state, predicted in 1987, the first candidate material to host it was grown in 2006.

There are many ways to approach these different potential paths to creating useful materials which creates a feedback loop which can be thought of as a materials lifecycle as shown in Figure 1.1.1. One of the simplest ways to start is to identify a particular desired property and then, guided by a theoretical framework, identify a material which should express that property and systematically attempt to synthesize it. Once a material has been synthesized, the resulting material must be identified to determine whether it is the material that was targeted, and if not, what was produced instead. Unexpected materials can then be characterized to determine

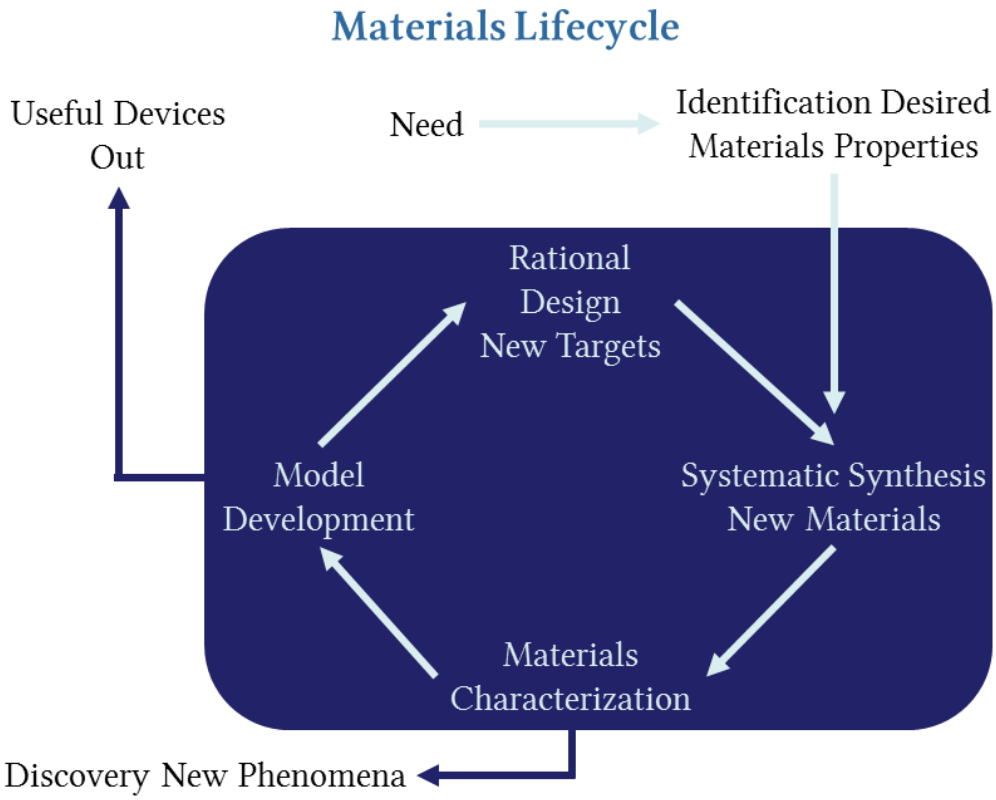

Figure 1.1.1 Feedback loop for the discovery of new materials, courtesy of T.M.M [1]

if they have any interesting or useful properties, feeding back into the materials design cycle.

My research has focused on two major parts of this materials design cycle, the synthesis of materials expected to host theoretical phenomena, and materials characterization. This has taken the form of determining new synthetic routes feeding that information back into the synthesis attempt in some cases. In others I have explored families of materials in an attempt to better understand underlying physics that might be exploitable for specific purposes. Before we dive into the research covered by this dissertation, we will introduce several topics. For more

information on the material covered here there are many excellent textbooks that go into greater detail. [2-5]

1.2 Background

1.2.1 Substitution Series

Frequently theory or experiment may identify a particular crystalline structure that could host the properties that are desired, however a known material does not express the desired characteristics due to the identity of the ions that make up its structure. In these cases substitution of one of the atoms or a site of the chemical compound with a different atom can be attempted in order to access properties that are theoretically predicted. An example of such a scenario presented in this dissertation is barlowite, which has magnetic ions, Cu^{2+}, arranged in a capped kagome lattice, however is theoretically predicted to become a quantum spin liquid if the all or most of the capping copper ions were replaced with nonmagnetic analogs such as zinc.

When substituting an element onto a site in a crystal lattice it is possible to produce a range of stoichiometries. This creates what is called a substitution series and the physical properties of a given material can be tracked as a function of the degree of substitution. This can help inform future experiments about the effects of substitution on the system, be used to compare to other similar series to examine the underlying physics, and reveal the development of any unexpected properties.

Another scenario is that a particular material shows a potentially useful property, but this property is poorly understood and does not occur under a useful set of conditions, or for some other reason the base material is not suitable for some purpose. In this case it may be prudent to see whether the desired property exists in other members of the same structural family of materials that have otherwise more desirable characteristics. This is the case with α-Nb_3Cl_8, a material with a defect CdI_2 structure, which undergoes layer rearrangement at temperatures around T = 90 K with an accompanying loss of magnetism (each Nb_3 metal-metal bonded cluster consists of niobium ions with a formal oxidation state of 2.67, resulting in a single unpaired electron delocalized across the cluster). Investigations of the reasons for this layer rearrangement were hampered by a comparatively large incoherent neutron scattering cross section of natural chlorine isotopes and a difficulty in the production of large crystals, which initially motivated the study of Nb_3Br_8, a material that had been reported to be able to be grown with the same alpha phase structure.

Further work showed that at room temperature, most Nb_3Br_8 was in its beta phase, analogous to the low temperature structure seen in Nb_3Cl_8 after layer rearrangement, and that β-Nb_3Br_8 underwent a transition into the same high temperature alpha structure above room temperature at T = 387 K. This led directly into an interest in whether a solid solution of $Nb_3Cl_{8-x}Br_x$ would have intermediate properties between the two end members. This is another type of substitution series,

however it is not site selective, like in the example of barlowite, but still helps to elucidate the behavior of a family of materials.

Before continuing to discuss the specifics about either of these cases it is important to introduce a context to solid state physics in general, an overview of techniques used in the synthesis, and the tools to characterize those materials. This is not an exhaustive review of the topics that follow in this chapter and focuses primarily on those relevant to the research discussed in the following chapters of this dissertation. Many textbooks cover the topics in the background subchapter in much greater detail.

1.2.2 Quantum Mechanical Considerations

The properties of materials in the solid state are emergent from their underlying quantum behaviors. At an atomic scale many of the properties of a system are quantized into discrete energy levels. Quantization can result in profoundly different behavior than would be expected from classical physics, and in the solid state the long-range interactions can give rise to emergent behavior, such as magnetism from spin. An additional consequence of quantum mechanics is that all subatomic particles have the property of wave-particle duality, in which quantum scale entities can behave as both particles and waves. Though there are many consequences to this, for example, the ability to use subatomic particles like

electrons and neutrons to perform diffraction, the main point of interest in this section is that subatomic particles are described mathematically by a wavefunction.

The electron wavefunction, $\psi(\mathbf{r})$, is the basic unit of information required to understand atomic orbitals. The wavefunction is the state function of the electron system, and the normalized square of the electron wavefunction, $|\psi(\mathbf{r})|^2$ when $\int_{-\infty}^{\infty}|\psi(\boldsymbol{r})|^2\, d\boldsymbol{r} = 1$, is the probability density of the electron, which describes a probabilistic electron cloud. The Schrödinger equations, to which the wave function is a solution, are given as:

$$i\hbar\frac{\partial\psi(\boldsymbol{r},t)}{\partial t} = \hat{H}\psi(\boldsymbol{r},t) \tag{1}$$

$$\hat{H}\psi(\boldsymbol{r}) = E\psi(\boldsymbol{r}) \tag{2}$$

where $\hbar$ is the reduced Planck constant, t is time, $\boldsymbol{r}$ is a vector describing a position in real space from the origin, which is typically defined as the center of an atom, E is the energy of a given system, and $\hat{H}$ is the Hamiltonian, the total energy operator on the system. These equations neglect spin or relativistic effects, and are respectively the time dependent and time independent Schrödinger equations. The time independent equation and a hydrogen atom (having one proton and one electron) are sufficient to derive atomic orbitals, as they are standing waves. From this a series of solutions for the wavefunction (eigenfunctions) can be found, shown in Figure 1.2.1. [4] These orbitals are for those determined for a one electron system; in a many electron system these orbitals can hybridize leading to non-trivial orbital shapes. Orbitals also have either even or odd parity, which is whether or not the

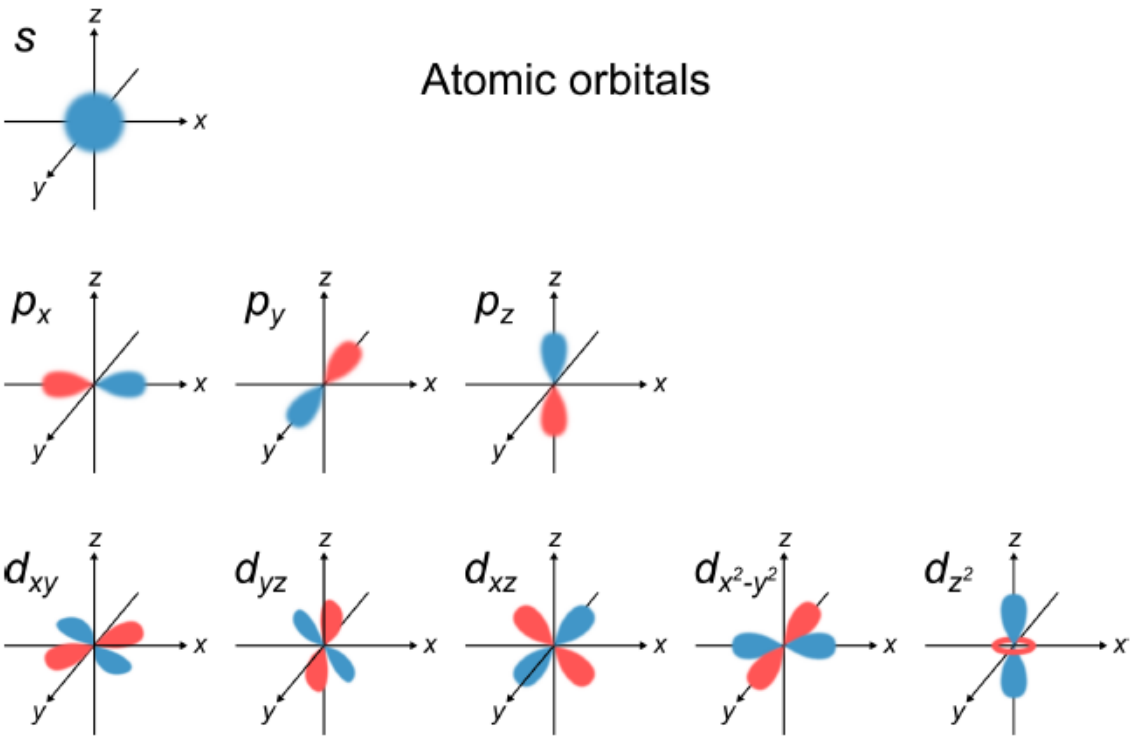

Figure: 1.2.1 Lowest lying *s*, *p*, and *d* subshells as determined for the hydrogen atom shaded blue and red for positive and negative lobes respectively. The *s* and *d* orbitals have even parity, while the *p* and *f* (not shown here) orbitals have odd parity.

application of the parity operator (x, y, z => -x, -y, -z) results in the orbital being unchanged, or swapping the position of the positive and negative lobes respectively. [4] The *s* and *d* orbitals have even parity, while the *p* and *f* orbitals have odd parity.

The Hamiltonians of a simple system like a hydrogen atom can be explicitly solved as it contains no electron-electron or neutron-neutron repulsion terms, though this is not possible when extended beyond two particles. An approximation of the Hamiltonian accounting for the typically most significant fundamental interactions in a real material is given by Eq. (3): [4]

$$\hat{H} = -\sum_i \frac{p_i^2}{2m_e} + \sum_{i,j} \frac{e^2}{|r_i - r_j|} - \sum_n \frac{p_n^2}{2m_n} + \sum_{m,n} \frac{Z_m Z_n e^2}{|R_m - R_n|} - \sum_{m,i} \frac{Z_m e^2}{|R_m - r_i|} \qquad (3)$$

with each of the sums modeling the electron kinetic energy, electron-electron repulsion, nucleus kinetic energy, nucleus-nucleus repulsion, and nucleus-electron attraction respectively for every particle in the system, though excludes the potential effects of spin-orbit coupling, spin-spin interactions, relativistic effects, and treats all modeled particles as point charges. Though usually small, spin-orbit coupling can become significant when atoms with a high atomic number are present in a material. Typically, the nuclear kinetic energy term can also be disregarded as a small correction. Here p is momentum, e is the charge of an electron, m_e is the mass of an electron, m_n is the mass of a nucleus, R and r are the radial distances from the origin of each nucleus and electron species, and Z is the atomic number.

Despite neglecting small corrections, accounting for all the interactions in Eq (3) for any more than two particles, as mentioned before, leads to no exact analytical solutions due to the repulsion terms [4]. Therefore, to model the behavior of many bodied systems, approximations are used, which at the lowest level simply neglect the electron-electron and nucleus-nucleus repulsion terms as negligible like the other small corrections we have already left out. This however only does a good job at describing systems with large separations between light atoms, such as in gasses. In solid state chemistry we often deal with large numbers of heavy atoms with many electrons packed closely together. As a result, the interaction strengths between atoms in solids, especially electron-electron interactions, are much larger and cannot be treated as negligible. The consequences of this strong interaction are the evolution of emergent properties in solids, such as phonons, ordered magnetism,

or even superconductivity. Modelling the behavior of such systems is far more complicated and thus consequently requires other approximations based on the fundamental microstructure of a given crystalline solid (its unit cell and space group), such as density functional theory, which have been constantly advancing.

1.2.3 Chemical Bonding in Solids

Solid materials are the result of a variety of chemical bonds. Two atoms in close proximity will often form a bond of some variety, and in a solid atoms are in usually in very close proximity. Large differences in electronegativity typically result in a bond that is more ionic in character, where electrons are effectively transferred between the bonded atoms, while smaller differences lead to bonds which are more covalent in character, where electrons are shared between atoms. Both can be considered the extreme end members of the far more realistic continuum of polar covalent bonding. Metallic bonding is differentiated by the delocalization of electrons across the bonding network. Sometimes solids are composed of discrete molecules which are too far apart to form these stronger bonds and may be held together by weaker forces such as dipole-dipole interactions, Van der Waals forces, hydrogen bonding or halogen bonding.

In the dipole-dipole interaction polar dipoles with partial negative and partial positive charges, due to the symmetry of molecular units and variations in electronegativity of the atoms composing those molecular units, result in the self-

alignment of those atoms into an energy minimizing lattice. These interactions are usually very weak resulting in compounds with low melting points. Hydrogen and halogen bonding are specific instances dipolar bonding which are often stronger than other examples due to large permanent dipoles arising from the strongly ionic character of many bonds involving hydrogen or the halogens. Halogen-bonding itself actually describes a larger class of bonds known as σ-hole bonding characterized by interactions between permanent dipoles, which can extend to the chalcogenides and pnictides as well, as their effectively large electronegativities can similarly produce large dipoles. Even when crystals are largely defined by strong chemical bonds, these weaker bonds may be observed and can be vital in driving the self-assembly and stabilization of the larger crystalline lattice, such as the role of fluorine in barlowite, despite sitting isolated in channels in the material with no strong bonds at all.

Van der Waals forces are another form of weak bonding that is especially relevant to two-dimensional materials. Van der Waals forces are a blanket term covering a number of weak forces, but perhaps the most relevant are the attractive forces resulting from instantaneous dipoles. Though operating at a further distance than strong chemical bonding and much weaker overall, van der Waals forces scale with the size of the two surfaces in near contact. In two dimensional crystals where each molecular unit is in effect an infinite layer, van der Waals forces can easily hold crystals together along the axis perpendicular to the plane and there can be enough orbital overlap for ordering parameters to involve multiple layers and not

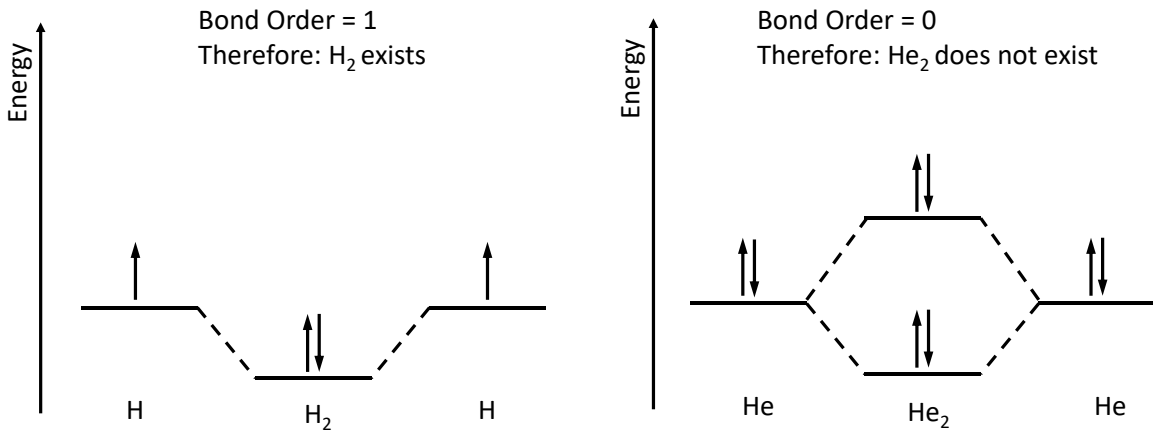

Figure 1.2.2 Atomic orbitals of H_2 and a hypothetical He_2 combining in a molecular orbital diagram. Linear combinations of orbitals with a lower energy than the initial atomic orbitals are bonding orbitals and those with a higher energy are antibonding. Bond order can be estimated as 0.5 x electrons in bonding orbitals – 0.5 x electrons in antibonding orbitals.

just remain in plane, despite the weak bonding. A consequence of this in two dimensional materials is that conductivity in the out of plane direction is often weaker than the in-plane direction.

In the strong bonding limit, where atoms are close together, overlap in their wavefunctions produces molecular bonding orbitals. These molecular bonding orbitals are a hybridization of the atomic orbitals of the atoms that are bonding. The simplest examples of this process can be seen for H_2 and He_2, the former of which is a favorable molecule, while the latter is not for reasons seen in figure 1.2.2. The electrons in figure 1.2.2 are shown by convention by up or down arrows, corresponding to their spin ($m_s = \pm ½$). For H_2 single electrons in the 1s energy level combine into a σ bonding orbital with an energy lower than that of free hydrogen ions which is what makes it a favorable combination. In its ground state the electrons in the molecular orbital are of opposite spin pairing as a spin singlet. He_2

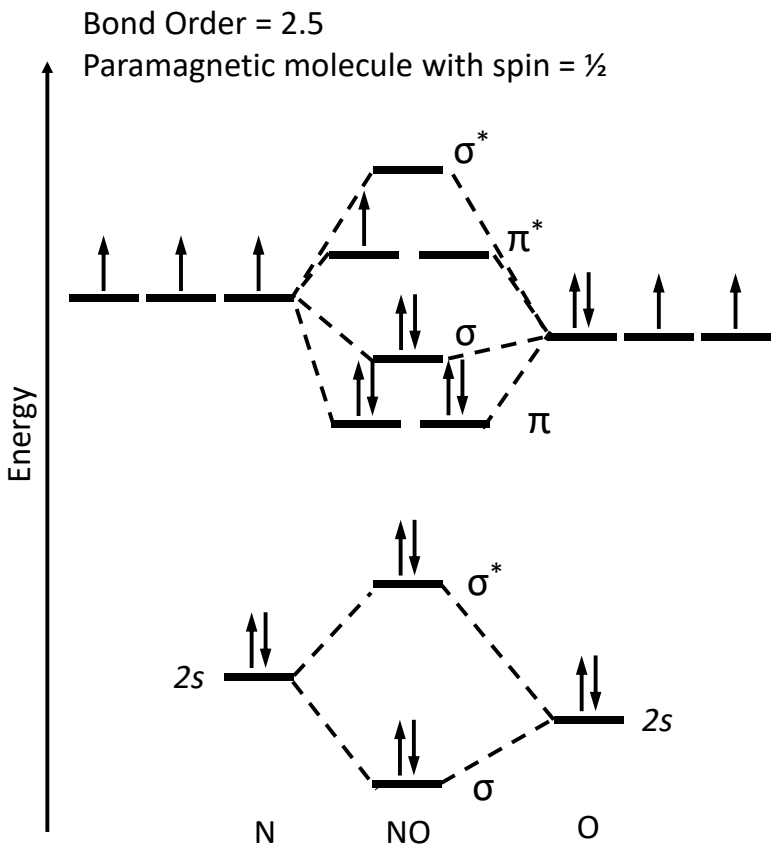

Figure 1.2.3 Atomic orbitals of NO combining in a molecular orbital diagram. With a single unpaired electron the molecule is paramagnetic with a spin of ½. In truth this diagram is a simplification of the NO molecular orbitals to provide consistency in the methods of generating them, as the 2*s* energy levels of N and O are in reality far enough apart in energy that they produce their own non-bonding orbitals rather than mixing.

on the other hand would have two electrons in the 1s+1s bonding orbital and two elections in the 1s-1s antibonding orbital. The bond order of a molecular bond can be determined in this method by the formula ½(*bonding* e^- - *antibonding* e^-), so for the case of hydrogen you have a bond order of 1. In a hypothetical He_2 you could can see in 1.2.2 would have energy both the low lying σ bond but also a filled higher energy σ* antibonding orbitals, resulting in a bond order of 0, another way to state

that there is no bond. A more complex example is provided for NO, as seen in figure 1.2.3.

This concept of molecular orbitals becomes extended when considering solid materials. As the number of atoms in an extended lattice increases the number of available energy states increases as well. Initially there are an increasing number of discrete energy levels, however as the material progresses towards the bulk these energy levels become effectively continuous. This can be described as a density of states (DOS), obtained by integrating over the band, as shown for an *s* orbital in figure 1.2.4. This example shows a single band and a single orbital around the Fermi level, which describes the top filling level of electrons at the ground state (T = 0 K). In any real material is at a finite non-zero temperature, materials with bands that cross the Fermi level like the example in figure 1.2.4 will have some thermal population of the excited states above the Fermi level. At a basic level, materials with bands that cross the Fermi level will be metals, while those with a gap at the Fermi level are insulating.

As can be seen by the filling of the band in figure 1.2.4, bands can also be described as a function of bonding and anti-bonding character. The example provided in 1.2.4 shows a one-dimensional chain of *s* orbitals at with the limits being momentum space from $k = 0$ for the fully bonding and $k = \pi/a$ where a is the interatomic spacing for the fully anti-bonding case. Between these extremes are intermediate levels of bonding/antibonding character with the energy of the band

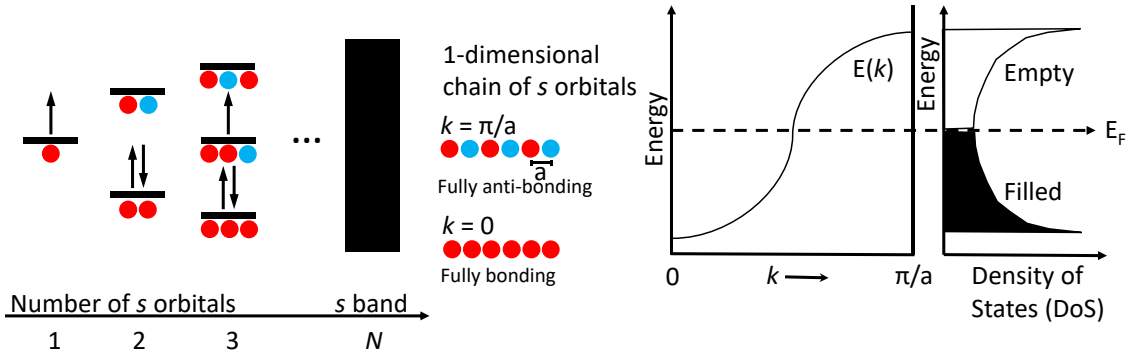

Figure 1.2.4 As the system approaches the bulk more and more discrete energy levels are required to describe the possible bonding and antibonding orbitals. This produces an effective continuum of discrete states within a particular energy range knowns as a band. The density of the discrete energy levels within the band is known as the Density of States (DoS). The shape of a band is described as a continuum in momentum space, *k*, and integrating over the band is necessary to correctly describe the shape of the DoS. At the ground state bands are filled up to the fermi level.

changing as a function of *k*. By integrating over the band the DoS of a material can be determined.

The example in 1.2.4 describes a single band for a single orbital in a single dimension. Real materials are three dimensional and so band structures will need to be constructed between several points in momentum space. These points represent the various π/a points in various different directions in a crystalline lattice where *a* is the lattice spacing. Additionally, as more orbitals are introduced there will be more bands, many of which may have some degree of overlap. Electronic properties are typically defined by the shape of the band structure, and the interaction between bands near the Fermi level. Calculations of real band structures are typically done with density functional theory (DFT) which uses approximations as exact solutions are intractable.

1.2.4 Magnetism

In insulating materials that do not have unpaired electrons one observes a weak, negative, temperature independent magnetic response. This small contribution to the magnetic behavior of the system is diamagnetism and is observed to contribute to the magnetic response of all materials as full electronic orbitals oppose applied fields. The effect of diamagnetism is generally much weaker than other forms of magnetism with the exception of superconductors, which are perfect diamagnets and expel all magnetic fields. In materials that do have unpaired electrons there are a variety of magnetic states that can be formed, the simplest of which are paramagnetism, ferromagnetism, antiferromagnetism and ferrimagnetism, shown in Figure 1.2.5.

Paramagnetism is the typical state of a magnetic material above its ordering temperature. Unpaired spins align randomly, undergoing dynamic thermal fluctuations when not in the presence of an applied field resulting in a net magnetic moment of zero. When a field is applied the electron spins will partially align with the field, however their alignment competes with thermal fluctuations, resulting in a decreasing response with increasing temperature for insulators. This temperature dependence follows the Curie-Weiss law, discussed in 1.3.1. When conduction electrons are responsible for a paramagnetic response, this results in Pauli paramagnetism which is a temperature independent positive magnetic response.

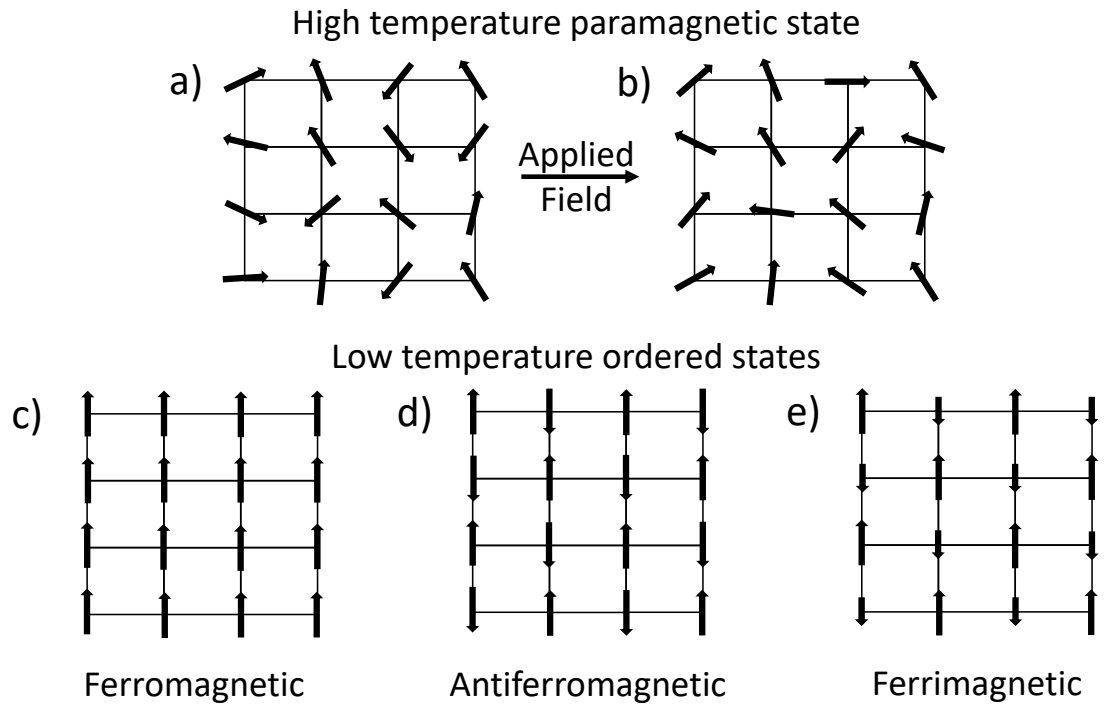

Figure 1.2.5 (a) A paramagnetic material has randomly oriented spins without an applied field and (b) partially aligned in response to a field but above its ordering temperature. The three simple types of order are (c) ferromagnetic in which spins co-align, (d) antiferromagnetic in which spins anti-align and (e) ferrimagnetic in which spins of different magnitude are antialigned resulting in a net magnetic moment. More complicated order is possible, such as non-commensurate magnetic structures, and the different ways of producing antiferromagnetic order are often not equivalent.

Below a critical temperature a paramagnetic state may give way to long range magnetic order. When the ordered spins align parallel to each other in a material, this is ferromagnetism and the ordering temperature is known as the Curie temperature. In real materials ferromagnetism exists in domains with boundaries that can shrink or grow depending on their alignment to an externally applied field, resulting in a net magnetization and permanent macroscopic moment so long as the

material is kept below its Curie temperature. This results in an observable hysteresis in the field response of a material to changing fields.

When ordered spins align antiparallel this is known as antiferromagnetism and the transition temperature is known as the Néel temperature [6]. As the spins on adjacent sites cancel each other out the material will have no macroscopic net magnetic moment. This results in the magnetic signal vanishing as the material becomes insensitive to applied fields, and had been considered technologically less useful than ferromagnets. The field of spintronics however has seen recent advances in materials such as Mn_2Au in which an antiferromagnetic lattice protects spin memory from stray fields, using anisotropic magnetoresistance to read Néel vector orientation.

Ferrimagnetism exists when spins of unequal magnitude are anti-aligned, similarly to antiferromagnetism. This occurs when there are are at least two sites with different magnetic ions that have antiferromagnetic correlations between each other. The smaller spin partially cancels out larger spin, resulting in a net ferromagnetic moment that is smaller than would otherwise be expected.

The above provides a simple picture of magnetism, which can be complicated by a number of factors. The geometries of real materials for example result in many very distinct types of antiferromagnetic ordering and many forms of interesting short range order in bulk magnetic systems can also exist, such as magnetic skyrmions however these are not generally relevant to this dissertation. One of these complications that is tangentially relevant is canted antiferromagnetism, in which

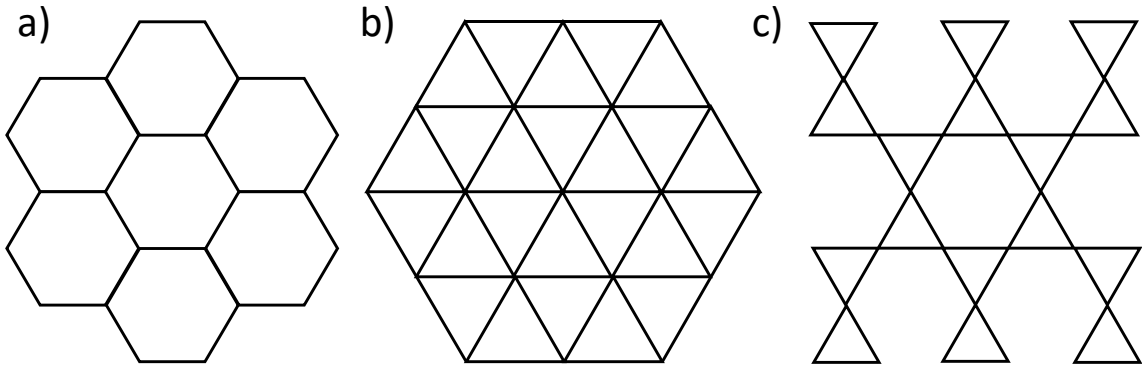

Figure 1.2.6: Examples of potentially frustrated of geometrically frustrated lattices (a) honeycomb, (b) triangular, (c) kagomé

the primary interaction of spins in a material is antiferromagnetic, however there is a slight tilt to the spins which gives the material an overall small ferromagnetic component as a function of tilt angle, as seen in the low temperature phase of barlowite. Partial and competing order, multiple degenerate ground states, and magnetic frustration can also complicate the real states of materials and potentially give rise to novel physics and applications.

1.2.5 Magnetic Frustration

Unpaired electron wavefunctions can overlap and interact to form the ordered magnetic states shown in Figure 1.2.5. In ordinary materials the transition temperature between the paramagnetic state and the ordered state is generally close to the absolute value of the Weiss constant determined from the high temperature paramagnetic behavior of the compound. When spins are arranged in a lattice such that there is not a single lowest energy ground state a material is likely to be geometrically frustrated which can significantly decrease the ordering temperature.

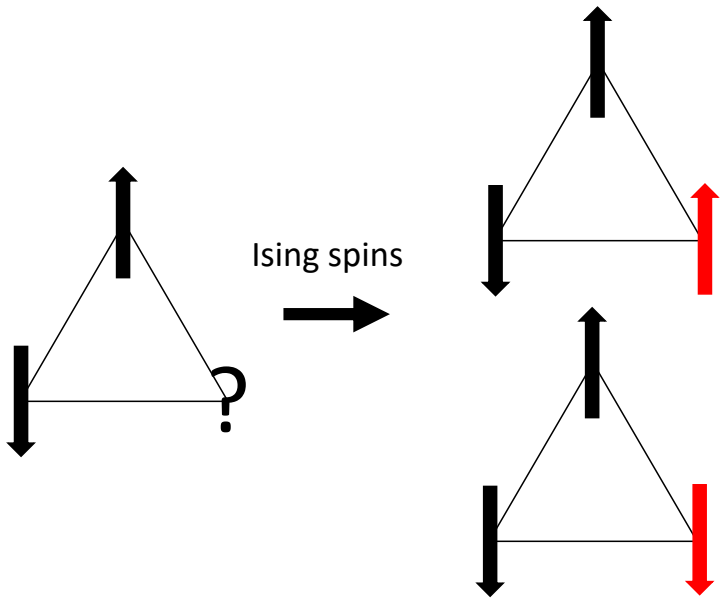

Figure 1.2.7 When attempting to place an Ising like spin on a triangular lattice there is no way to fill the triangle so that it has a net moment of zero, additionally both orientations are degenerate in energy.

Generically frustration is more likely to be interesting when correlations between electrons are strong, normally implying a high ordering temperature. Figure 1.2.6 shows the two-dimensional magnetic sublattices which can lead to magnetic frustration, the most important of which are the triangular lattice (Figure 1.2.6 b) and the kagomé lattice (Figure 1.2.6 c).

The simplest example of geometric frustration is the triangular lattice antiferromagnet, in which the exchange coupling, *J*, between the magnetic sites is isotropic. If you assign two of the sites as having an up and a down spin then you are unable to pick an orientation of an Ising-like spin on the third site such that the triangle will have a n et magnetic moment of zero as shown in Figure 1.2.7. Either choice of spin on this triangle will result in a ground state of equal energy to the opposite choice, i.e. they are degenerate. For a classical system, if extended to a

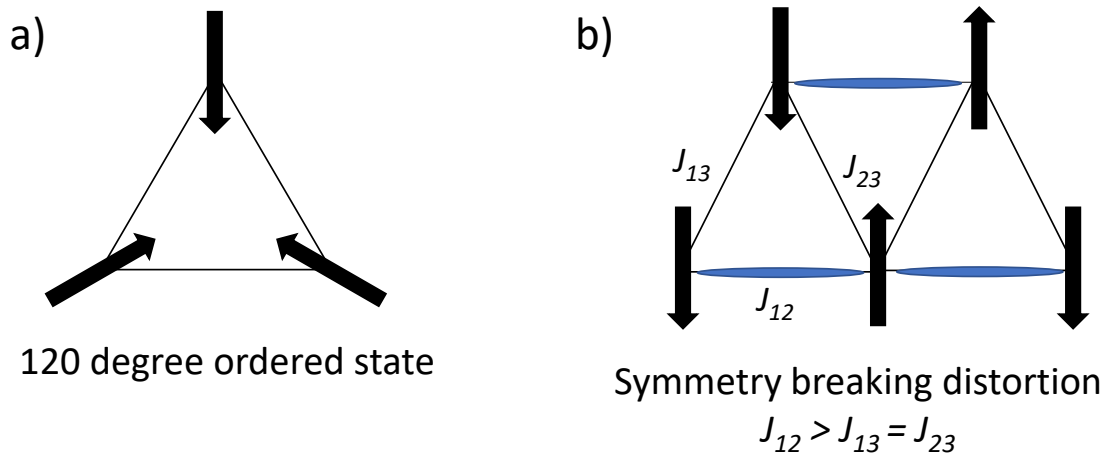

Figure 1.2.8 Two common ways in which magnetic ordering may occur in 2 dimensional triangular lattices, a) a 120º ordered state of Heisenberg like spins and b) symmetry lowering distortions which change the strength of magnetic exchange parameters between sites allowing for a lowest energy ordered state. Another version of this allows for the formation of singlets between the distorted sites resulting in a non-magnetic ground state.

larger lattice, you end up with a degenerate set of ground states in which short range order is possible, but that precludes long-range order. In quantum systems the ground state is instead a superposition of a large number of spin configurations.

As previously mentioned, normal antiferromagnets typically have a Néel temperature close to that of their Weiss constant. In systems with geometrically protected frustration this ordering temperature is typically suppressed by quantum fluctuations to much lower temperatures than would otherwise be expected. Most geometrically frustrated systems do appear to order eventually, the possible ground states for the two-dimensional triangular lattice for example are shown in Figure 1.2.8. A material that behaves classically might also become a spin glass, a state with frozen disordered spins that lacks any long-range order, rather than breaking global symmetries and taking on a more traditional form of magnetic order.

As shown in Figure 1.2.8 (a) one way in which a geometrically frustrated state can order for the two-dimensional triangular nets is the 120º ordered state. This is only possible under the condition where the exchange interactions, *J*, are equal between all three sites. As the frustrated state tends to be energetically unfavorable, the more common way that these systems order is by undergoing a symmetry breaking structural distortion that removes the frustrated state. The structural distortion, changing distances and angles between magnetic units and their exchange pathways, alters the magnitude of the magnetic exchange interactions between sites giving the new values $J_{12} > J_{13}$, in the example shown in Figure 1.2.8 (b). Now that J_{12} is stronger in our example, after assigning a spin value for atom 1 below the material's ordering temperature, we can assign spins for atoms 2 and 3 in the example, with 2 ordering antiferromagnetically with atom 1 and atom 3 aligning ferromagnetically. When extended to a full lattice this leads to long range magnetic order as long as the exchange interactions are strong. Other ways in which frustration can be avoided include orbital ordering in which symmetries are broken by the breaking of orbital degeneracies, giving rise to periodic patterns of occupation of specific orbitals.

In order to access the more interesting geometrically frustrated ground states, it's important to find materials that do not undergo distortions that can relieve magnetic frustration. A material that was considered to meet these requirements considered in this work is zinc substituted barlowite. Unsubstituted barlowite has an apparently perfect kagomé lattice of spin ½ Cu^{2+} ions with a spatially disordered

capping Cu^{2+} ion. This randomly positioned capping Cu^{2+} causes local anisotropy in the exchange parameters of the kagomé network and barlowite orders at around T = 15 K. Theory suggests that when substituting Zn^{2+} for Cu^{2+} the only site which is substituted is the capping site. Zn^{2+} is non-magnetic and doesn't undergo Jahn-Teller distortion, which means that in theory a perfect spin ½ kagomé lattice is left with the cap equidistant from each member of the kagomé network. This results in all magnetic exchange parameters being not only strong and isotropic, but the other atoms in the network connecting the two-dimensional kagomé layers together should not have any favorable symmetry lowering distortions that might otherwise relieve the geometric frustration.

1.2.6 Quantum Spin Liquids

At low temperatures where quantum fluctuations dominate the interactions in a geometrically frustrated magnetic material that has not ordered can host potentially useful degenerate quantum ground states. A possible ground state for a frustrated material is one characterized by valence bonds in which every pair of free electrons in the system form singlet bonds with 0 overall spin, first described by Anderson [7]. The spins in these bonds are maximally entangled without necessarily being entangled with other spins. In the classical limit these are localized static bonds, producing a valence bond solid (VBS). In a VBS the localized static bonds typically

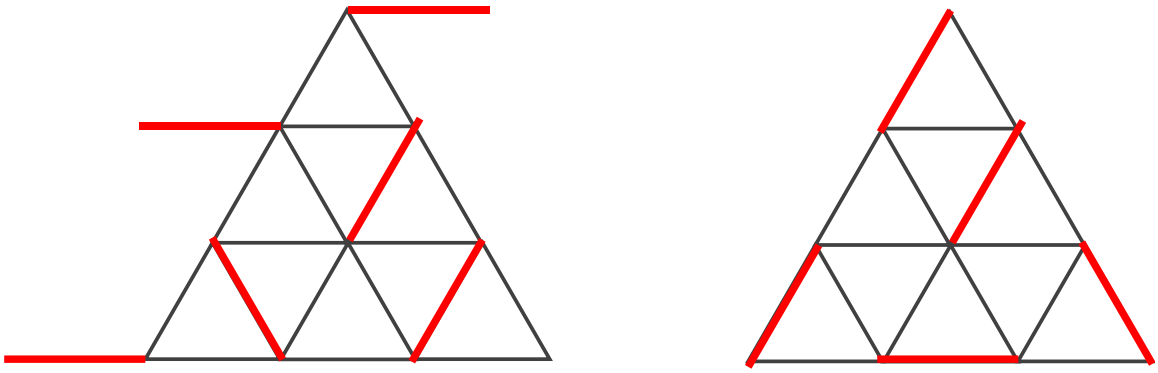

Figure 1.2.9 The classical spin liquid could be in either of these states where the red lines represent singlet bonds between sites, or any other equal energy degenerate state, however the quantum spin liquid is a superposition of all possible low energy states, also allowing long range entanglement of spins.

break short range lattice symmetries, and the state lacks the long-range entanglement of the quantum spin liquid (QSL).

In order to go from this classical limit to a more interesting state quantum mechanical fluctuations need to drive resonance of the bonds between equal energy states originally described as a resonating valence bond (RVB) state. This results in a ground state consisting of a superposition of many different arrangements of spin singlet bonds. There are a number of consequences to this superposition, the first of which is that, unlike the VBS ground state, translational symmetry is not broken in the RVB ground state since there is no local order. This also allows for long-range entanglement of spins in the lattice, i.e. the entanglement of spins which are not nearest neighbors. Since these singlets are maximally entangled this superposition should theoretically give rise to novel topological properties, and the RVB state theoretically plays a role in the physics of high temperature superconductors.

An important trait of QSLs is that they support excitations with fractional quantum numbers. The most important of which is the spinon, a charge neutral excitation carrying a spin $S = ½$. There are two sources of spinons in QSLs, defects that result in lone sites not participating in singlet bonds, or the breaking of a singlet bond to produce a pair of spinons. Ordinarily it is energetically expensive to move free spins through a material, however in the gapless QSL spinons are able to propagate freely through the solid by rearrangement of local valence bonds. Spinons can be searched for using inelastic neutron scattering to examine the spin excitation spectrum of a solid, making it a useful tool to indicate a potential QSL ground state.

Distinguishing a QSL from a VBS or any other model featuring static but essentially random distributions of bonds is not trivial. As mentioned previously evidence of a spinon continuum is one piece of evidence in favor of a material possessing a QSL ground state. Other evidence has to be considered as well to make a positive claim of a QSL ground state since there isn't a single defining trait that an be easily tested for. To develop a QSL state there needs to be strong interactions between magnetic sites but an ideal quantum spin liquid will not develop magnetic order at any temperature, requiring magnetic susceptibility measurements to be performed. Should those measurements suggest both strong correlations through a large Curie-Weiss temperature and a lack of magnetic order, more sensitive measurements such as NMR or μSR may be called for. There are additionally many different models of potential QSL states which may be distinguished between by

specific heat measurements which provide information about the low energy density of states. Thermal transport may also be potentially useful to identify whether excitations in the lattice are localized or free to propagate.

1.3 Synthesis and Characterization

1.3.1 Introduction to synthesis

In solid state chemistry typical synthesis methods involve heating reactants to high temperatures in order to overcome energy barriers and get them to react. Generally speaking the simplest solid state syntheses are attempts to produce the thermodynamic product. This can be defined using the Gibbs free energy equation:

$$\Delta G = \Delta H - T\Delta S$$

where ΔH is the change in enthalpy (the internal energy of the system), ΔS is the change in entropy (the disorder inherent to the system), and ΔG is the Gibbs free energy of the system. For any given set of reactants, the reaction should in principle be spontaneous when ΔG is negative, though this will not be the case if there is not sufficient energy in the system to overcome its activation barriers, as in the example of diamond and graphite.

The diamond to graphite pathway has a negative ΔG value, which means that the decomposition of diamond to graphite is thermodynamically favored, however diamonds do not decompose to graphite under standard temperatures and pressures. This is because there is a very large energy barrier (E_a) for this reaction pathway

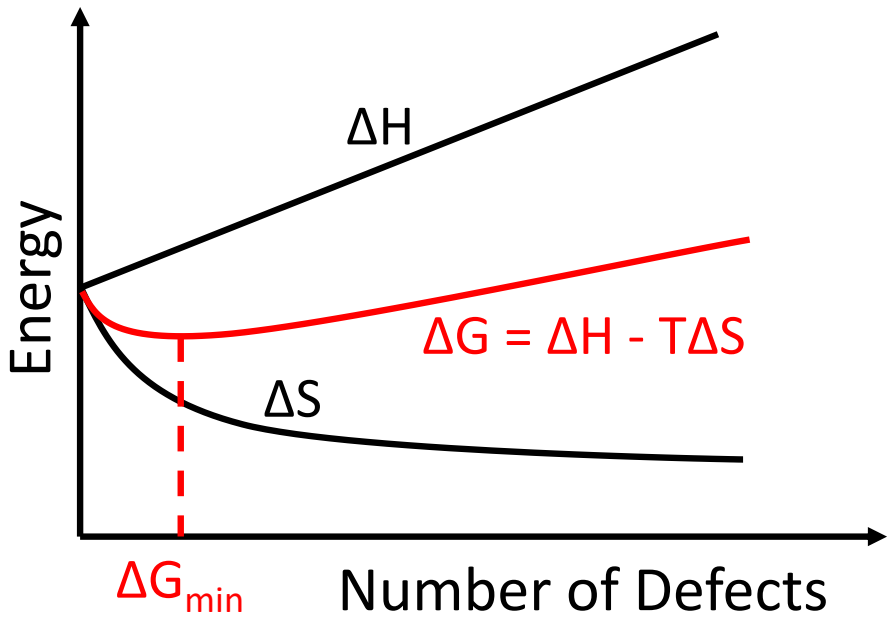

Figure 1.3.1 ΔG as a function of the number of defects. Due to the effects of entropy and enthalpy ΔG typically reaches a minimum at a finite non-zero number of defects, changing the reaction conditions such as temperature can alter the location of ΔG_{min}

and there isn't enough thermal energy at room temperature to overcome this barrier, diamonds tend to remain in a kinetically favored metastable state. So for simple solid state synthesis reactions it is necessary to have an energetically favorable target, and provide enough thermal energy to the system to overcome any large activation barriers to make a reaction spontaneous.

Most synthesis techniques rely on finding a way to produce thoroughly mixed stoichiometric product from initially unmixed sometimes off stoichiometry starting materials. The easiest way to get mixing to occur at the atomic level is for a reaction to occur in a liquid or gas phase, however with sufficient heat and mechanical homogenization diffusion can also occur in solid phases. In all cases it is generally

more favorable for some defects to form in as grown materials due to the relationship of the Gibb's free energy to enthalpy and entropy. As more defects are incorporated into a structure the entropy becomes larger. Altering the reaction conditions, such as the gas environment, or the temperature of the reaction can alter the defect concentration at which the minimum Gibb's free energy occurs. The enthalpy of formation of various types of defects are typically not equivalent and often have a temperature dependence. Sufficiently high synthesis temperatures can often assist in minimizing the number of defects in a product. [8]

$$G = G^* + N_D \Delta H_D - T N_D \Delta S_v - T \Delta S_c(N_D) \quad (4)$$

Equation 4 provides a somewhat simplified equation for the Gibb's free energy (G) as a function of the number of defects. G^* is the free energy of a theoretically perfect crystal, N_D is the number of defects, ΔH_D is the enthalpy change per defect, ΔS_v is the change in vibrational entropy per defect and $\Delta S_c(N_D)$ is the change in the configurational entropy as a function of the number of defects. As mentioned previously, not all defects are equivalent, at large enough concentrations defects interact with each other, and even terms like enthalpy are not necessarily static over broad temperature ranges.

The simplest and most widely used solid-state synthesis method, often referred to as "shake and bake" chemistry, begins with stoichiometric mixtures of powdered reactants which are ground together with a mortar and pestle, and then frequently pressed into a pellet followed by heating those reactants at temperatures in the hundreds to well over a thousand degrees Celsius for periods of time between

several hours to several weeks, though timeframes on the lower end of this scale are typical. The driving issue faced when using this sort of reaction is the diffusion of elements through a solid, in order to mix the elemental reactants at an atomic level to produce a crystal lattice. Finely grinding the reactants together to produce an isotropic mixture of the elements with the smallest possible unit volumes and largest possible surface areas per unit volume of the reactant particles helps to minimize barriers to diffusion and total diffusion distances. Depending on the materials being used, intermittent grinding may be required after each of several heating cycles to get the reaction to run to completion.

It may also be necessary to protect the reactants from atmospheric oxygen or moisture depending on the identity of those reactants and/or the targeted oxidation states of reactants in the final product. The most common cases are where either the most oxidized state of a metal ion is not being targeted in the final product, or non-oxide anions are incorporated in the final product. There are several ways that this may be done, the exact method often depending on the nature of the specific reaction. One method is to heat the reactants in a tube furnace under a flowing inert or reactant gas. This is most common when there is little or no risk of the product or reactants with fixed masses vaporizing or otherwise being lost. The other common method is to seal reactants in a vessel that is inert to the reactants being used and is either evacuated or backfilled with an inert gas. The most common material used in this method is quartz as it's comparatively easy to work with. When there is a concern about the reactants potentially reacting with the quartz itself

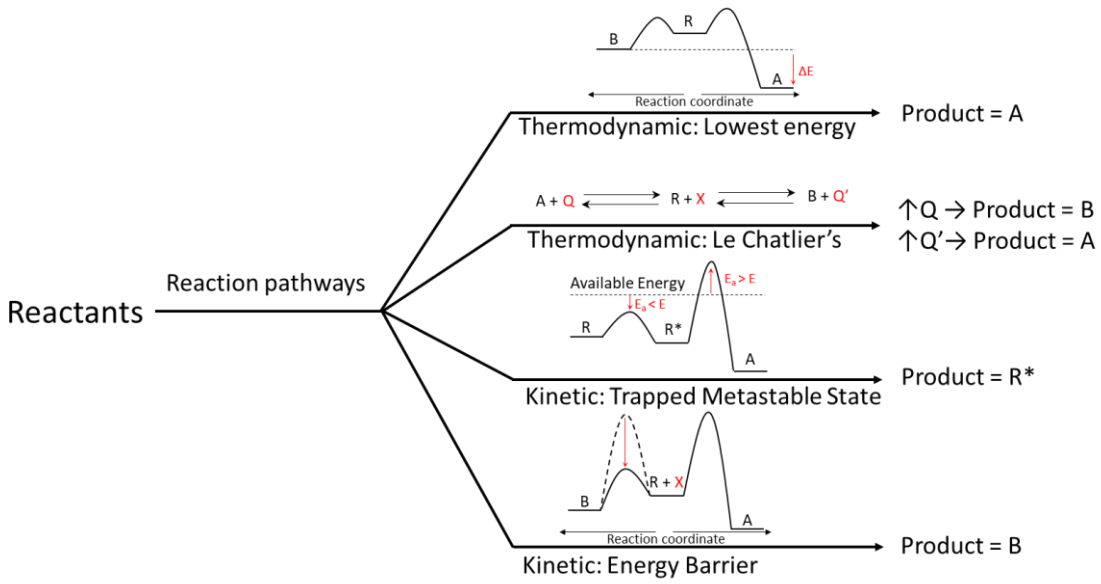

Figure 1.3.2 Common simplified reaction pathways which can be used to control the product of a given reaction. [9]

crucibles of various materials can be used to hold the reactants, and the inside of the quartz ampule can also be carbon coated by cracking ethanol or acetone.

There are many different ways to control reactions in order to produce the desired product. The previously described shake and bake method generally results in the product with the lowest thermodynamic energy, as shown in the top most pathway of Figure 1.3.2, a simplified description of how reactions can be controlled. Real world circumstances often mean that the simplest synthetic methods are insufficient to achieve the desired results, and it's also important to note that the product of the shake and bake type reaction is almost always a powder. Frequently the reason to use other methods is that crystals of a material may be needed, and some of those other methods will be discussed in the subsections to follow after this general introduction.

Continuing to explore the pathways shown in Figure 1.3.2, Le Chatelier's principle is another thermodynamic route of control which is most often exploited in solution chemistry but can be relevant to other synthetic methods. It is the basic principle that states that if a system is in equilibrium then changing a constraint, concentration is provided as the example in 1.3.2, however it can also be a constraint like pressure or temperature. When a constraint is shifted the equilibrium will shift to counteract the effect of the changed constraint.

There are three generic ways in which kinetic control is typically achieved in solid state synthesis, the first two of which align with what is shown in Figure 1.3.2. If there is some condition for which the internal energy of an intermediate state can be made to be lower than that of the starting reactants and a sufficiently high energy barrier between that metastable state and the final lowest energy configuration, then the reaction can be run at comparatively low temperatures to yield the kinetic product. The kinetic product doesn't have to be an intermediate, just have a lower activation barrier than the thermodynamic product and a lower internal energy than the initial reactants, as shown in fourth route in Figure 1.3.2. A final way to get a product which is a trapped metastable state at room temperatures is to grow it under conditions where it is in fact the thermodynamic product, and then quench the reaction to room temperature, rather than slowly cooling it which may allow it to convert to a thermodynamically stable phase it would ordinarily pass through on cooling.

1.3.2 Hydrothermal Synthesis

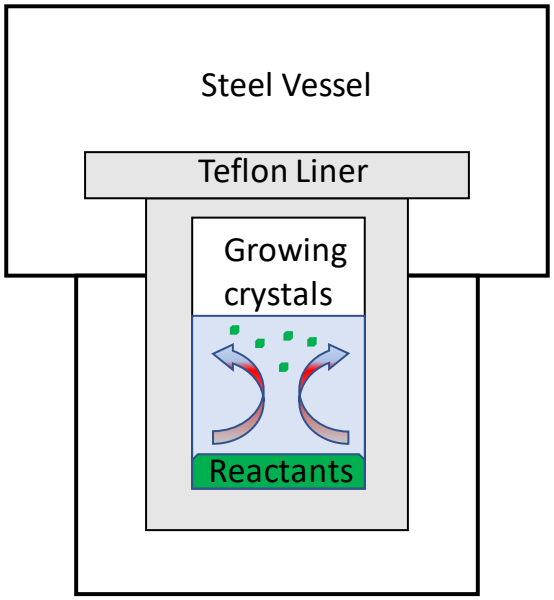

Figure 1.3.3 Diagram showing the set up for a typical hydrothermal synthesis reaction, in which a temperature difference within the vessel drives crystal growth. Small temperature gradients create flows within the reaction vessel, moving dissolved materials from the hotter zones at the bottom to cooler zones at the top where they're less soluble, favoring crystal growth in these cooler areas.

Hydrothermal synthesis is a method to grow crystals in a liquid solution that are either difficult to grow or inaccessible through other synthetic routes and is one of the common ways that crystals are deposited in nature. Depending on the materials involved, there are several advantages to hydrothermal synthesis over the solid phase techniques previously described. Reactants can vary from slightly soluble to fully soluble in whatever liquid medium is used. This means that the problems of slow diffusion rates in shake and bake synthesis are not an issue in hydrothermal syntheses. This generally has the effect of greatly decreasing activation energy barriers, allowing reactions that would normally only occur at temperatures of a thousand degrees Celsius or higher to happen at temperatures of scales around one

hundred to a couple hundred degrees Celsius. One way to already see how this could be useful is if the product you're targeting would decompose at temperatures far below those that would be required to get its precursors to react with a shake and bake method.

There are a few different ways in which hydrothermal synthesis can be carried out. One of the most common set-ups, shown in Figure 1.3.3, involves placing reactants within an inert vessel, or into an inert liner which can be placed into said vessel, known as an autoclave. This then allows the materials to be heated under autogenous pressure, which has two primary effects. Like temperature, pressure can modify the equilibrium of reactions occurring within the autoclave, generally favoring systems with decreased entropy. Pressure also ensures that the liquid medium remains a liquid up to temperatures well above its boiling point under standard pressure, or in the case of larger autoclaves designed to handle higher temperatures and pressures, a super critical fluid. Autoclaves that use Teflon liners have an operational limit of T = 240 ºC, above which the Teflon begins to soften. Variations on this sort of set up include using other materials and geometries for vessels, such as Inconel alloys for high temperatures and pressures, or quartz tubes, which can be used with either vertical or horizontal temperature gradients, providing large separations between the reactants and growth zones.

The specific example provided in Figure 1.3.3 relies on the existence of an internal temperature differential in the vessel. This is the most common technique in hydrothermal synthesis and specifically exploits the effects of temperature on

fluid dynamics and solubility. At the hotter zone at the bottom of the vessel reactants are dissolved creating a saturated solution at that temperature. The reactants are then carried to the cooler zone by currents resulting from differences in density between the hot and cooler liquids. Once in the cooler region the saturated solution becomes supersaturated as the solubility of most ions decreases at cooler temperatures. The excess dissolved material then either nucleates out a new seed crystal, or deposits on an existing seed crystal, with the growth dependent on the competition between these two mechanisms. The ideal case is one where growth is far more favored than nucleation, and there are many factors which can play a role in this. This method can be used in both cases where the initial material (nutrient) and the product are the same material, or where unique reactants are dissolved and the final product is less soluble than the reactants at the growth zone, a hybrid method with the metastable phase technique below.

Another way that hydrothermal synthesis can be used involves heating a solution until all reactants are fully dissolved and then slow cooling the resultant solution. Similar to the above this involves creating a supersaturated solution, but controlling the degree of super saturation by control of the ramp rate of the temperature. As the solution cools nucleation will occur, ideally not much nucleation if the ramp rate is appropriately slow, and crystals will begin to grow. In some cases this method can result in a significant amount of control over the actual growing conditions, however, to be effective it requires that there exist conditions under which all possible products will be fully soluble in the nutrient solution. This limitation

means that it is typically not possible to both seed these reactions and have the advantages that control over the growth profile can provide. This can limit the size of crystals that can be grown through slow cooling, though a single growth cycle may be enough to produce crystals of a useful size if nucleation can be sufficiently depressed.

The third generic method of hydrothermal synthesis is known as the metastable phase technique. It exploits differences in solubility between a normally stable starting material and the desired product under the growth conditions used. Under the growth conditions the nutrient compounds are thermodynamically less stable than the desired product and dissolves in solution. The desired product begins to crystallize out of solution as the dissolved ions begin to exceed the solubility of the desired product under the growth conditions. The majority of nucleation and growth continues until the nutrient compounds are consumed and the ionic content of the solution drops to a stable equilibrium with the final product, at which point any further deposition of material should be balanced by dissolution of the desired product back into solution. While this technique is generally sufficient for the synthesis of polycrystalline material, it is often combined with one of the above techniques when attempting to grow single crystals for various further experiments.

In the real world it is not always possible to achieve ideal synthetic conditions. Barlowite provides an example of a particularly challenging scenario, in which the final product is far less soluble than the nutrients are under most reaction conditions in which barlowite can be synthesized at all. The primary consequence of this seems

to be that nucleation competes heavily with growth, meaning that growth targeting 400 mg of barlowite typically produces more than one hundred thousand very small single crystals. Furthermore, the reaction that produces barlowite proceeds even at comparatively low temperatures, though the reaction takes longer and produces lower quality crystals. Most efforts to minimize nucleation either prevented barlowite from growing, or had a minimal effect, which led to trying something a bit different, serial seeded hydrothermal synthesis.

A commonly used technique to increase crystal size is through seeding. Some initial growth produces small but clean crystals and then the growth, or a similar profile is run again, with the addition of one or a few of these previously grown crystals as seeds. In many cases, a single growth cycle will then be sufficient to produce crystals large enough for further experiments as when nucleation rates are low the majority of new material will deposit on the preexisting seed. In the case of barlowite material would deposit on seed crystals like in any other growth, but the overwhelming amount of nucleation had two main impacts which limited the amount of growth seen in any one cycle. New crystals scavenge the vast majority of the nutrients in any one cycle and nucleation can occur on existing crystals, which eventually sheathes them in a layer which prevents further growth of the original seed crystal for that cycle.

Initially a fairly large number of crystals were selected from a typical growth and seeded into the next. In the next few growths, the primary challenge was finding those seeds among the new crystals and then mechanically cleaning their surfaces

without damaging or losing the tiny crystals. The utilization of lower nutrient concentrations and enhanced fluid movement through the use of stir bars and enhanced thermal gradients inhibited the growth of new crystals, making the task of locating preexisting crystals easier until they had grown large enough to see by eye. Though these techniques did encourage growth on preexisting crystals, nucleation was still a problem and enhanced shear forces from greater fluid motion unfortunately reduced the quality of crystal surfaces, requiring more material to be removed between cycles, until growth slowed down. After fourteen of these cycles the surfaces of the existing crystals had to be etched with hydrobromic acid to restore them and allow growth to continue. Further growths used only low reactant concentrations and ethanol as a competitive ligand on the Jahn-Teller distorted Cu^{2+} site to slightly reduce nucleation, however the seeded crystals were now easily distinguishable from the other smaller crystals produced in each synthesis, and this continued for thirteen additional growth cycles, for a total of twenty-seven, before all tracked crystals were larger than the minimum size required for single crystal neutron diffraction.

Serial hydrothermal synthesis has a number of considerations that have to be made beyond normal seeded hydrothermal synthesis. Because the crystals are repeatedly subjected to additional growths, the effects of small imperfections such as twinned crystallites can be magnified, meaning considerable attention has to be paid to cleaning the crystals between cycles. Mechanical scraping of the crystal surfaces can be effective at removing crystallites, but is done at the risk of damaging

the surfaces of the crystals potentially creating more nucleation sites for crystallites with potentially different orientations to grow in the future, though such scratches can also heal if the new material deposits in the same orientation as original crystal. Mechanical removal of crystallites is also likely to leave behind crystal dust which adheres to the crystals and similarly provides new nucleation sites with a high likelihood of being misaligned with the original crystals, which when removed leave behind holes that are likely to capture more crystal dust during cleaning and further roughen the crystal surfaces. Removing this crystal dust is best accomplished through short (~15-30 second) sonication cycles, in a dispersant of some with a reasonably low surface tension to discourage the adherence of small particles to existing surfaces. For barlowite the liquid used was an equal mixture of deionized water and ethanol, though toluene is generally a good choice.

1.3.3 Chemical Vapor Transport

Another common technique to grow crystals is chemical vapor transport (CVT). The most common setup for this, shown in Figure 1.3.4 is to seal a powder of either reactants, or the material one wants to crystallize into an evacuated quartz tube, potentially along with a transport agent, and then to place the entire setup in a thermal gradient. A simple overview is that for most materials the reactants will be placed in the hot zone, and crystal growth will occur in the cold zone. What happens between these two locations is that the reactants will enter the gas phase in some

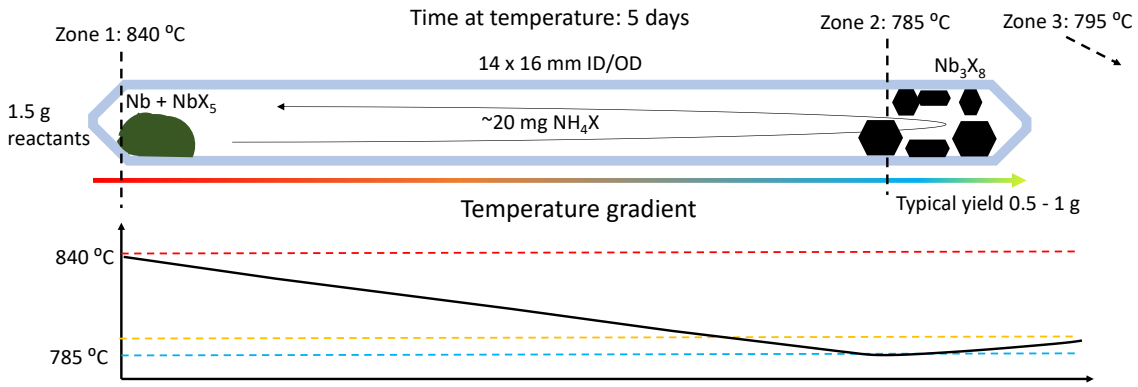

Figure 1.3.5 Schematic showing an example set up of chemical vapor transport (CVT) reactions for a material discussed later in this dissertation. Reactants are sealed in a quartz ampule under vacuum along with a small amount of transport agent. The tube is heated under a temperature gradient and the transport agent decomposes, in this case to NH_3 and HX gas, which dissolves small amounts of the reactants at the hot end and transports them to the cold end where they are deposited either as new seed crystals or onto crystals actively growing.

manner, then be transported to the growth zone, where they then can either nucleate a new seed or be deposited onto an existing seed. Similar to hydrothermal synthesis the problems of slow diffusion that can plague shake and bake methods are generally not an issue, because material is transported in the gas phase, though defects are still common, affected by the actual mechanisms by which growth occurs. These factors are often poorly understood and difficult to predict when attempting to synthesize a new material.

There are several factors involved in the effective control of CVT. Most materials will not undergo self-vapor transport, meaning that a transport agent needs to be added. Even materials that can undergo self-vapor transport may benefit from the addition of a transport agent which can speed up and change the energetics of growth, resulting in different parameters and yields. A transport agent is a material

which decomposes into a gas phase at elevated temperatures in which a given material might be "soluble." The most common transport agents are those which contain a halide species like $TeCl_4$, NH_4Cl, and I_2. $TeCl_4$ decomposes into a mixture of Te and Cl_2 gas, with the Cl_2 acting as a transport agent, while for NH_4Cl, the active species is HCl. Different transport agents can have radical effects on the morphology and growth behavior of crystals, though generally speaking the actual identities of the gas phase species and the mechanisms involved are often complicated and not well understood, making the selection of transport agents a somewhat empirical search, and with some agents you may risk incorporating them in their entirety or one of their components which should also be a consideration. Some more obscure transport agents may have more complicated gas phases than those already listed, forming complexes with reactant materials in order to transport them, and may have different mechanisms of action under different temperature ranges and concentrations.

Temperature is another important consideration for CVT. At lower overall temperatures the risk of defects tends to be greater than at higher temperatures. Large temperature gradients speed up growth rates, however gradients that are too large may similarly increase the likelihood of defects. For some materials, a desired phase is only stable within a particular temperature range, and so the growth zone must fall within this range. The temperature of the growth zone can also affect whether nucleation or growth is favored. Many materials grow best when the

temperature of the growth zone is either just below the decomposition temperature of a material or just above the temperature at which the desired phase is stable, however this is not a hard rule, and such information may not be known ahead of time, and might be different under CVT conditions, with low pressures and a transport agent.

Like in hydrothermal growth, seeding can be an effective way of growing larger crystals in CVT. When it works it can be an effective technique to produce large and high-quality crystals. It is important that the surface of seed crystals be as pristine as possible, which means then when not dealing with oxides, the crystals typically should never be exposed to air, as most materials will gain an oxide layer on exposure to air or moisture, which can inhibit further growth. Some materials can't be seeded for reasons such as decomposition in the presence of a transport agent occurring before reaching transport conditions. In these cases, the only things that can be done is to fine tune the reaction conditions to produce viable crystals in a single growth step or to introduce a non-soluble seed to initiate growth on.

While a powerful tool in synthesis, CVT does have some disadvantages. With a typical length of about a week to a couple month reaction times are generally longer compared to many shake and bake and hydrothermal reactions, though there are some outliers with those techniques as well. Residual moisture and oxygen contamination of air sensitive reactants are some of the more common problems in CVT which can radically alter the behavior of the transport and the phases that are

grown at a particular temperature. Finally, setting up a seeded reaction is more difficult than for hydrothermal methods, and requires changes to a tube, either by necking to a small diameter, or incorporating a physical barrier such as quartz wool which can carry residual moisture, that affects gas flow and might introduce new elements, meaning that preliminary experiments used to grow seed crystals might not be fully indicative of how a seeded growth will progress.

1.3.4 Crystallography

After a reaction has been run to completion one must identify what has been produced. When dealing with an extended phase solid material this can be done by diffraction with non-ionizing radiation, such as x-rays, electrons and neutrons, of which x-rays and neutrons will be discussed in this section. X-rays scatter off of the electron cloud, which has a size comparable to the wavelength of an x-ray. This results in two main consequences for x-rays, scattering is dependent on the number of elections in an atom (Z) and scattering intensity drops off with angle. This means that light atoms are generally hard to see with x-rays and total scattering patterns are often dominated by heavier atoms in a system where there are large differences in the Z numbers of elements. When considering structural data, neutrons scatter off of atomic nuclei which are much smaller than the wavelength of the neutrons used in diffraction. The intensity of neutron scattering is consequently defined by the scattering cross sections, both coherent and incoherent, of the elements involved,

and is independent of angle. Neutron scattering cross sections do not follow a trend like Z number for x-rays and therefore both heavy and light atoms can be seen. Even isotopes of a particular atom can have very different neutron scattering cross sections. One of the most relevant examples to consider is hydrogen and its isotope deuterium, both of which are virtually invisible in x-ray scattering, but behave quite differently in neutron scattering. Hydrogen has a small coherent cross section of 1.7583 barn and the largest incoherent cross section of any element by a large margin of 82.03 barn [10], meaning structural studies with neutrons are dominated by noise if a sample has a high hydrogen content, but deuterium has a larger positive cross section of 5.592 barn with a much smaller incoherent cross section of 2.05 barn, meaning that deuterium is provides a larger signal when attempting to isolate its location in a structure and the data overall is far less noisy [10]. Neutrons have spin, so are also able to scatter magnetically. In this case the neutrons are scattering off of the electron cloud, rather than the point like nucleus of an atom, and so have a form factor that decreases with angle.

While intensities are the function of the identity of the atoms in a unit cell, diffraction patterns are dependent on its lattice structure. Neutrons and x-rays are useful because they have wavelengths on a similar length scale as the distances within an ordered solid. Their wave-like properties allow them to undergo constructive and destructive self-interference dependent on the incident vector of radiation, shown in Figure 1.3.4 and described by Bragg's law:

$$n\lambda = 2d \sin\theta \quad (5)$$

where n is any integer, λ is the wavelength of the incident radiation, d is the lattice spacing, i.e. the distance between repeating units in each of the principle directions, and θ is the scattering angle. In the simplified two-dimensional representation shown in Figure 1.3.5 lattice spacing is also the distance between layers, and it can be observed that only specific values of θ satisfy the Bragg condition for any value n. Though the simplified figure with interference off only a couple of layers would produce broad maxima, real materials have a very large number of repeating units that are interfering with each other, leading reflections to present as sharp peaks around the angles that satisfy the Bragg condition and primarily destructive interference with small contributions from incoherent scattering elsewhere. More

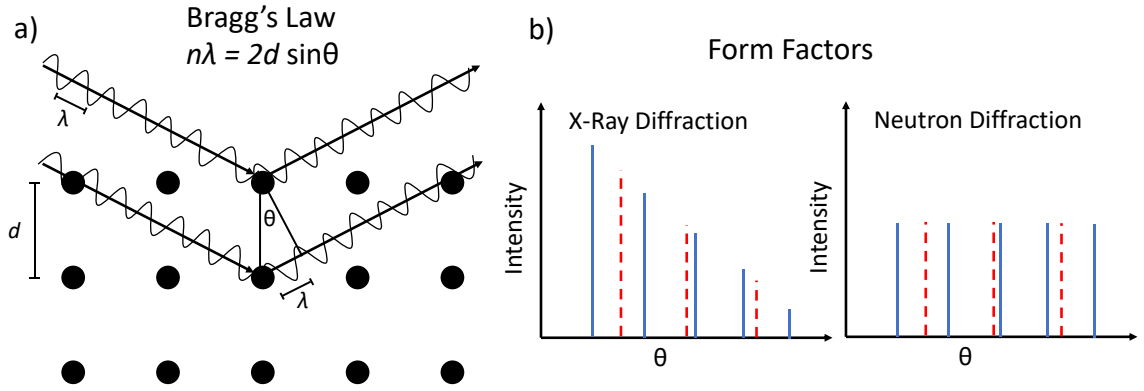

Figure 1.3.5 a) Simplified representation of a crystalline lattice with incoming x-ray photons diffracting resulting in constructive interference only around the conditions where Bragg's law $n\lambda = 2d \sin\theta$ is satisfied. Diffraction is a function of self-interference of individual particles allowing even lab scale instruments to provide large signal to noise ratios. b) Form factors for different types of diffraction, x-rays diffract off of electron clouds which are similar in size to the x-rays resulting in a decaying form factor with increasing angle. Neutrons which diffract off atomic nuclei have a flat form factor, though due to their spin, neutrons can also diffract off of magnetic sites with a similar form factor to x-rays.

explicitly, peaks are observed centered at each allowed value θ, with some peak width, $\delta\theta$ inversely related to the thickness of a sample divided by the wavelength of the incident radiation. This typically is a negligible contribution to peak width for even small single crystals, but is a consideration when dealing with powder samples due to small crystallite sizes. The exception to this is that diffuse scattering can be observed in crystals with disorder.

To determine a crystal structure, it is necessary to sample over a large number of angles and orientations. The two most general ways to do this are powder diffraction and single crystal diffraction. In powder diffraction a finely ground powder of material is expected to represent all orientations at once, so scanning through θ allows one to observe all reflections independent of orientation. In single crystal diffraction all peaks within a certain range of θ for a given incident angle to the crystal will be observed at once and recorded for each incident angle as the crystal is rotated in space. Powder diffraction is generally faster and doesn't require clean crystals, though single crystal diffraction tends to provide more detailed structural information with fewer convoluting factors than powder diffraction. In both cases peak positions will be a function of the unit cell, and depending on the symmetry of the lattice there may be systematic absences, locations where you would expect a peak from Bragg's law, however, some symmetry element of the lattice results in a structure factor of zero. Symmetry elements that can give rise to systematic absences are non-primitive lattice centering and the presence of glide

and screw symmetries. The atoms in a particular lattice can sit on sites with various allowed symmetries, which are described by Wyckoff positions. The combination of general reflection conditions from the symmetry elements of the cell, along with conditions from special Wyckoff positions in the cell define the allowed reflections for a given unit cell, more information can be found in the *International tables for Crystallography* [11].

In powder diffraction, peak sharpness is a function of crystallite size and crystallinity. As mentioned above, as the number of sites which are allowed to interfere approaches the infinite limit, the observed reflections will narrow towards the ideal limit of an infinitely sharp Bragg peak, though other effects prevent even single crystals from actually presenting with infinitely sharp peaks. When crystallite sizes are small in a powder, the peaks can be severely broadened, while large crystallites may see broadening below instrumental limits. Crystallinity is the other main sample dependent factor related to peak broadening, and can take either the form of disorder that results a range of effective lattice parameters, or nonuniform strain.

Factors that affect peak width do not have an effect on the total integrated intensity of a given peak. When the distribution of orientations in powder diffraction is ideal, the identity of the atoms within a given structure and the overall form factor are the only considerations in peak intensity. Under these conditions every material, depending on its composition and structure will have a unique and

calculable diffraction pattern, however there are other deviations from the ideal that can make this difficult. When the distribution of orientations is not random, i.e. when there is a preferred orientation, the intensities of peaks dependent on their orientations can change drastically. Stacking faults can also affect peak intensities making it a greater challenge to solve structures from patterns where there is a large degree of either. Two-dimensional Van der Waals layered materials in particular are subject to both significant preferred orientation and the development of stacking faults when ground, making single crystal diffraction far more reliable for solving their structures.

Single crystal diffraction can also reveal information that would be hidden in powder diffraction. Since single crystal diffraction provides data from specific orientations it provides less ambiguous symmetry information about each orientation. Because reflections from many orientations overlap in powder diffraction, weak reflections may be hidden and systematic absences in a particular direction can be missed because other peaks share a particular angle, potentially causing unit cells of the wrong size or symmetry to be chosen. Additionally, powder diffraction will not show evidence of pseudo-merohedral twinning which can be inferred in single crystal diffraction by increased mosaicity of overlapping spots, and inconsistencies in peak intensity.

Twinning by merohedry and twinning by pseudo-merohedry are special cases of twinning [12]. In both cases the twinning results in direct overlap of the reciprocal

lattices, which can masquerade as a higher symmetry group while appearing generically to be a single crystal. The reason for this is that in both merohedry and pseudo-merohedry the twinning is along a symmetry element of the crystal lattice. In twinning by merohedry the apparent symmetry and the actual symmetry are part of the same crystal class. In pseudo-merohedry the lower symmetry group has lattice parameters that are close to those of a higher symmetry class, such as a monoclinic cell with $\beta \approx 120^{o}$ and $a \approx c$ which may have a three-component twin around *b* producing a pseudo-3-fold axis and an apparent hexagonal symmetry. This particular type three component pseudo-hexagonal twinning can also occur with orthorhombic space groups and is known as a trilling twin.

1.3.5 Transmission Electron Microscopy

Another way to examine atomic structure is to use electrons as your probing agent rather than photons. Electrons scatter more strongly than X-rays and neutrons, but can be transmitted through a thin enough sample, typically with a sample thickness on the order of less than 100 nm. Using electrons this way is known as transmission electron microscopy (TEM) and can be a very informative technique. Shown in figure 1.3.6 is a schematic diagram of the beam generation and magnetic lensing in a TEM with set ups for imaging mode shown in 1.3.6b and diffraction mode in 1.3.6c. In imaging mode a TEM, especially an aberration corrected TEM, can provide real-space images of atomic structures with sub-nanometer resolution. In

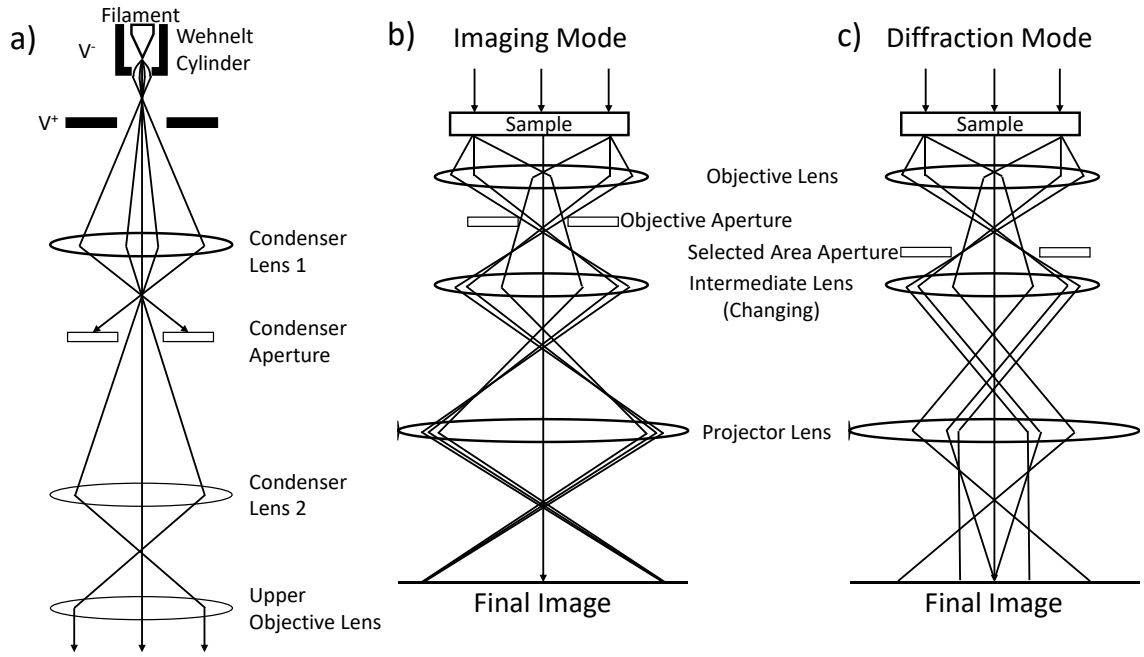

Figure 1.3.6 a) TEM beam generation and lensing. A bias voltage extracts electrons from the filament, after which they are condensed, accelerated and eventually collimated before reaching the sample. Upon reaching the sample they diffract and transmit with the lower lens assemblage determining whether a b) real space image or c) diffraction pattern are observed.

diffraction mode single crystal diffraction patterns can be obtained by scattering off the electron clouds of the sample [5].

Figure 1.3.6a demonstrates the basic set up of a TEM through electron generation up until the collimated electron beam hits the sample. Typically a filament of either a material with a very high melting point like tungsten or a very low work function is used to produce loosely bound electrons which are extracted by a comparatively small voltage bias. Once extracted the electrons are focused and accelerated typically by a series of magnetic lenses to a final electron current of 100-300 keV.

Electrons, unlike photons and neutrons have both a charge and spin. The consequences of this are that like photons and unlike neutrons they scatter off the electron cloud of an atom when considering the structure of a lattice, but that they're also sensitive to magnetic order, like neutrons. Unlike both photons and neutrons, electrons are also sensitive to charge, and have been used to directly image charge disproportionation in structures. Also unlike both photons and neutrons, its both possible and easily practical to obtain extraordinarily small spot sizes (less than 50 nm) for the beam, allowing for probes of local symmetry, without averaging over the bulk as is done for both single crystal neutron and x-ray techniques and by default TEM requires much smaller samples than either. When preparing samples there are two main techniques, thinning a solid sample until it's transparent to the electron beam or grinding a sample and dispersing it across a holey carbon grid as is often done with polycrystalline powders.

There are a variety of techniques that can be applied for the purpose of capturing real space images of an atomic structure. At the most basic level what is done by the instrument is shown in 1.3.6b, in which a series of lenses project the image either onto film or a digital CCD. Great care must be taken when attempting to acquire high resolution TEM images for several reasons. The first is that the sample must be sufficiently isolated from any ambient vibration, since the even small vibrations can contribute considerable blurring over the exposure time of the image. Also, since electrons are strongly scattering, and given the amount of lensing required to

focus the beam both before and after the sample, the beam must be aligned and stigmated properly. Aberration correction must also be performed to adjust for spherical and chromatic aberrations due to imperfections in both the magnetic lenses and a finite energy distribution of the electron beam. Thermal vibrations of the lattice itself can also be reduced by using a cryo-cooled stage, further improving image quality.

When performing TEM in diffraction mode, or Selected Area Electron Diffraction (SAED), the objective and intermediate lenses are arranged to focus all beam paths that leave the sample with the same angle onto the same spots in reciprocal space. An electron diffraction pattern is a cut of the Ewald sphere, however, because samples are extremely thin the diffraction intensity should be treated as a relrod parallel to the beam in reciprocal space, rather than a point. This relrod can intersect the Ewald sphere over a range of angles, rather than a single angle, which can result in diffraction intensity when not exactly aligned with a particular plane, and sometimes diffraction from additional planes at higher d values in reciprocal space in electron diffraction [5]. For example, you may be looking at a 0kl plane, but potentially see spots from a 1kl plane as well. In addition, because electrons scatter strongly, additional disorder can be observed as diffuse scattering. All of this makes structural analysis non-trivial for TEM diffraction, but also makes it a powerful complementary technique to other diffraction techniques, and to provide local information about a structure.

1.3.6 Magnetization

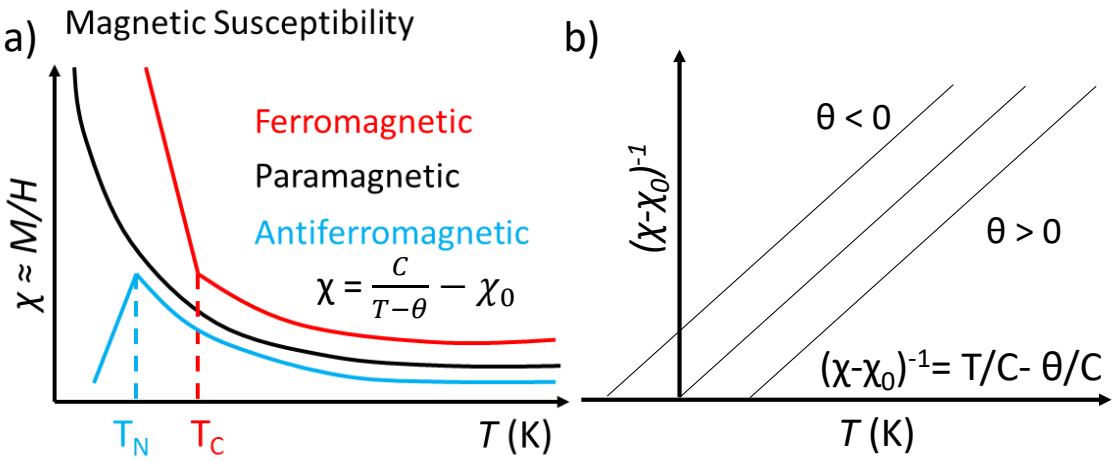

Figure 1.3.7 a) The magnetic susceptibility trends are shown for paramagnetism, ferromagnetic order and antiferromagnetic order. Ferromagnetic order occurs at the Curie temperature (T_C) and antiferromagnetic order at the Neel temperature T_N. b) Curves linearized for Curie-Weiss analysis allowing for the determination of interaction strength and sign. This linearization is generally done on the high temperature portion of data away from any transitions as the Curie-Weiss law breaks down as T approaches θ.

The magnetic susceptibility of materials is typically determined by approximation from magnetization data, $\chi \approx M/H$ which is sufficient for the purposes of this discussion. The magnetization of a material can either be the same in all directions, or anisotropic, in which the crystalline direction plays a role in magnetic susceptibility, which is reasonably common for layered materials. The magnetic response of a material is dependent on the spin and number of spin centers of material, and how they order with one another.

The first type of magnetic response is diamagnetism, which is a weak negative response for a material that has no unpaired spins. This negative response is a result of quantum mechanical effects of electron orbitals, opposing an applied field. As a

result, all materials have a diamagnetic contribution, however this is typically negligible compared to contributions from other forms of magnetism in magnetic materials. It should be noted that superconductors are perfect diamagnets, expelling all magnetic fields through the Meisner effect.

When magnetic sites exist in a material, above the ordering temperature there is competition between disorder due to thermal fluctuations which randomize spin orientation and the alignment of spins with an applied field. This is paramagnetism and results in an inverse relationship between magnetic susceptibility and temperature for insulating materials. When the free spins are conduction elections, then this results in Pauli paramagnetism, which is temperature independent. The approximate functional form of the high temperature paramagnetism is given by

$$\chi_{m.} - \chi_0 = C/(T-\theta) \tag{6}$$

where $\chi_{m.}$ is the magnetic susceptibility per mole magnetic ion, C is the Curie constant which is proportional to the square of the effective moment ($p_{eff} = \sqrt{8C}$), and θ is the Weiss temperature, which is a measure of the strength of the magnetic interactions in the material. Rearranging equation 6) as:

$$\frac{1}{\chi_m - \chi_0} = \frac{1}{C}T - \frac{\theta}{C} \tag{7}$$

Allows you to linearize and determine values of both C and θ. The sign of θ reflects the nature of the magnetic correlations in a material, when the sign in negative the

material should order ferromagnetically and when positive it should order antiferromagnetically.

There are many possible complications to this analysis, such as partial order or multiple degenerate magnetic ground states, but only one exception is particularly relevant to the purposes of this dissertation. Low lying excited magnetic states can present as an upturn in susceptibility with increasing temperature as those excited states are populated.

1.3.7 Heat Capacity

The specific heat of a material is the amount of energy required to change the internal temperature of a material by a fixed amount. Thermodynamically there are two forms of heat capacity, constant pressure $C_p = (\frac{\partial Q}{\partial T})_p$ or constant volume $C_v = (\frac{\partial Q}{\partial T})_v$, where Q is the internal energy. Experimentally it tends to be much easier to measure heat capacity at constant pressure than it is to measure it at constant volume. This is generally done using a physical properties measurement system (PPMS), though it is worth noting that at low temperatures there isn't much difference between C_p and C_v. Contributions to heat capacity come from conduction electrons as well as phonons (lattice vibrations), which each have different functional forms that contribute to the total heat capacity. Heat capacity is also related to the amount of entropy in a system as $C_p = T(\frac{\partial S}{\partial T})_p$. As a consequence,

heat capacity can provide a great deal of information about the bulk properties of a system, as well as any transitions it might go through [3]

$$C_{electronic} = \gamma T \tag{8}$$

$$C_{Einstein} = 3sR(\frac{\theta_E}{T})^2 \frac{\exp{(\frac{\theta_E}{T})}}{[\exp{\left(\frac{\theta_E}{T}\right)} - 1]^2} \tag{9}$$

$$C_{Debye} = 9sR(\frac{T}{\theta_D})^3 \int_0^{\frac{\theta_D}{T}} \frac{(\frac{\theta}{T})^4 \exp{\left(\frac{\theta}{T}\right)})}{\left[\exp{\left(\frac{\theta}{T}\right)} - 1\right]^2} d\frac{\theta}{T} \tag{10}$$

Equations 8, 9, and 10, show the respective contributions of duction electrons, Einstein phonon modes and Debye phonon modes to the overall heat capacity. Einstein and Debye refer to phonons with optic and acoustic modes respectively, which are lattice vibrations with small and large dispersions in frequency. In this context θ is a temperature corresponding to the characteristic frequency of each type of vibration, and *s* is the oscillator strength, the number of oscillators of that particular type. The total number of oscillators should add up to the number of atoms per formula unit. At the low temperature limit, when not considering entropy from a transition or other contributions to heat capacity like Schottky anomalies the total heat capacity should be approximately $C_p = \gamma T + \beta T^3$. This allows for an easy determination of the electronic specific heat and works as a starting place to determine phonon contributions. The book written by A. Tari [x] is a good place to

find further details about heat capacity and the derivation of the formulas presented here.

When determining the magnetic contributions to specific heat there are two common ways the problem is approached in practice. Measuring a non-magnetic analog should account for the phonon contributions to heat capacity, within a small margin of error, given that the masses of the non-magnetic ions substituting for the magnetic ions in the material of interest are not identical. When no non-magnetic analog exists fitting the high temperature portion of heat capacity data, assuming no Einstein modes are present, can be a practical solution. When subtracting out either a non-magnetic analog or high temperature fit, what is left behind should be the heat capacity due to magnetic order, which can be integrated to find the associated entropy of a particular transition.

1.3.8 UV-Vis Absorbance Spectroscopy

UV-Vis absorbance spectroscopy is a type of absorbance spectroscopy particularly useful for observing allowed electronic excitations in materials. When compounds have a band structure that has gaps between occupied and unoccupied electronic states which are allowed transitions in its band structure and those gaps correspond to an energy in the range of ultraviolet to visible light, then excitations from its ground state to allowed excited states can be observed by measuring the absorbance of photons of light with a

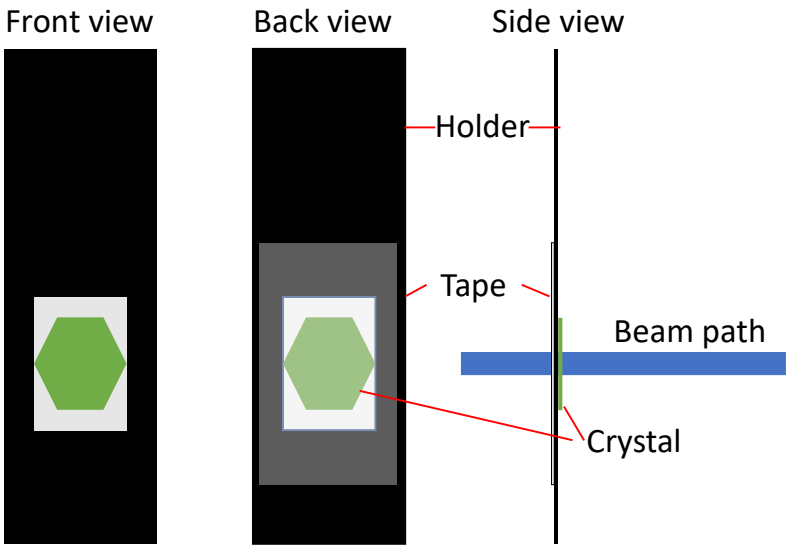

Figure 1.3.8 Sample holder designed to allow measurement of translucent solid samples in a UV-Vis absorbance spectroscopy unit capable of operating only via transmission.

corresponding energy in a UV-Vis spectrometer. This can allow a quick and direct probe of the energy levels of the band structure around the fermi level. UV-Vis spectroscopy is generally performed on solutions, which provide much of the technique's additional utility, however this will not be covered within the confines of this dissertation.

Performing UV-Vis spectroscopy on a solid sample can be done in two ways. For instruments that can operate in reflectance mode solid samples of arbitrary thickness can be measured, however such instruments are less common than those which operate solely with a transmission geometry. In such cases a sample can still be measured, so long as the sample can be thinned sufficiently to transmit light. When working with mechanically exfoliatable

materials this is often best achieved by thinning the sample onto a piece of transparent tape as shown in figure 1.3.8.

1.3.9 Attenuated Total Reflectance Infrared Spectroscopy

Attenuated total reflectance infrared spectroscopy (ATR-IR) is a technique utilizing crystalline materials with high indexes of refraction in contact with a sample to induce total internal reflection and generate and evanescent wave. This evanescent wave penetrates only a short distance into a sample, limiting the total path length through the sample, avoiding issues of strong IR attenuation transmission techniques face as well as avoiding the additional complication of sample thickness effects on absorbance spectra.

Mid-IR spectroscopy, between 4000 and 400 cm^{-1}, is itself is a probe of vibrational modes which involve a change in dipole moment. The characteristic frequencies at which vibrational modes occur is a factor of both bond stiffness and the reduced mass of the components involved in the vibrational modes. This factor in particular allows the use of isotopes to positively identify the nature of certain stretching frequencies by comparing samples with different isotopes substituted, though this is most dramatic when substituting D for H. IR active modes for a material can be determined through group theory, which means that using ATR-IR spectroscopy to measure IR-active gamma point phonon modes can serve as a quick probe of lattice symmetry as was done for Zn doped barlowite in this dissertation.

1.4 Conclusions

The work presented in the following chapters describes the characterization of the structure and properties of two different families of two-dimensional materials. The first is barlowite, a quantum spin liquid host candidate. Though the overall structure is not perfectly hexagonal as previously reported, the kagomé layers are not apparently distorted. To at least moderate levels of zinc substitution on the interlayer site the symmetry breaking distortions appear to be preserved, however despite this deviation from perfect hexagonal symmetry, the physics of the kagomé layers appears mostly undisturbed, as seen in the comparison to the behavior of the herbertsmithite series making barlowite a good system to further probe the physics of QSLs. In addition the method used to produce large single crystals for neutron scattering experiments should extendible to the production of Zn^{2+} substituted samples.

The other material is the $Nb_3Cl_{8-x}Br_x$ family which was first of interest for Nb_3Cl_8, which undergoes a transition between a high temperature paramagnetic state and a low temperature singlet ground state. Nb_3Br_8 was found to undergo the same transition between a high temperature paramagnetic phase and a low temperature singlet ground state observed in Nb_3Cl_8. The temperature of this transition can be continuously tuned between that of the two end members by varying the Cl/Br ratio in $Nb_3Cl_{8-x}Br_x$. There is a significant benefit to any study of the physics in the low temperature phase of this family from the fact that β-Nb_3Br_8

appears to share the same magnetic properties as β-Nb_3Cl_8 without any evidence of distortion from rhombohedral symmetry in its low temperature phase. In terms of device making the properties can be continuously tuned between those of the end members, the compounds are effectively stable in the bulk on the timescale of years, and large single crystals of any composition in the series can be rapidly grown.

Further work on the Nb_3X_8 family of materials to uncover the exact nature of the ground state is still ongoing. Modelling of the singlet-triplet excitation gap shows reasonably close agreement between fits to magnetic susceptibility and to μSR data, though the μSR data is considered more reliable. From the μSR data the gap found to be 14.0(15) meV for Nb_3Cl_8 and 34.5(3) meV for Nb_3Br_8. Additional work on the chalcogenide substituted Nb_3QCl_7 member of the Nb_3X_8 family of materials resulted in the synthesis of Nb_3SCl_7 and Nb_3SeCl_7, neither of which had been previously reported. Nb_3SeCl_7 shares a structure with Nb_3TeCl_7, which was expected, while Nb_3SCl_7 shares a structure with Ta_3SBr_7. The structure of this sulfur analog has a ferroelectric orientation at room temperature, and evidence from synthesis suggests a very high temperature ferroelectric to non-ferroelectric transition.

2. Single crystal growth of $Cu_4(OH)_6BrF$ and universal behavior in quantum spin liquid candidates synthetic barlowite and herbertsmithite

This work was co-written with the following authors and is published under the following citation:

Physical Review Materials **2**, 044406 (2018)

https://doi.org/10.1103/PhysRevMaterials.2.044406

C.M. Pasco[1,2], B.A. Trump[1,2], Thao T. Tran[1,2], Z.A. Kelly[1,2], C. Hoffmann[3], I. Heinmaa[4], R. Stern[4], and T.M. McQueen[1,2,5]

[1]Department of Chemistry, The Johns Hopkins University, Baltimore, MD 21218

[2]Institute for Quantum Matter, Department of Physics and Astronomy, The Johns Hopkins University, Baltimore, MD 21218

[3]Oak Ridge National Laboratory, Oak Ridge, TN 37831

[4]National Institute of Chemical Physics and Biophysics, Akadeemia tee 23, 12618 Tallinn, Estonia

[5]Department of Materials Science and Engineering, The Johns Hopkins University, Baltimore, MD 21218

2.1 Introduction

Quantum spin liquids (QSL) represent a new class of magnetic behavior characterized by long-range entanglement and have attracted considerable attention [13-16]. The suppression of classical long-range antiferromagnetic order by geometric frustration has been considered a promising route to the production of materials which could host a QSL state [17-19]. One of the most studied candidates for hosting this state is synthetic herbertsmithite (HBS), $ZnCu_3(OH)_6Cl_2$, a spin-1/2 kagomé antiferromagnet and the end member of the Zn^{2+} substitution series of the $Zn_xCu_{4-x}(OH)_6Cl_2$ paratacamite family [10-30]. HBS possesses copper kagomé planes which are separated from each other by non-magnetic Zn^{2+} ions in the interlayer. Recent work has shown that there are residual Cu^{2+} ions (~15%) on the interlayer, complicating investigation of the low energy physics of the S=1/2 kagomé lattice [28-30].

Synthetic barlowite, $Cu_4(OH)_6BrF$, is another copper S = ½ kagomé compound also reported to harbor perfect Cu^{2+} kagomé layers [31-33]. In contrast to synthetic herbertsmithite, the layers of synthetic barlowite directly overlap (AAA stacking) each other rather than being staggered (ABC stacking), resulting in a trigonal prismatic arrangement of hydroxide ions surrounding the interlayer copper/zinc site (instead of octahedral as in synthetic herbertsmithite). Theoretical work has indicated that the substitution of Zn^{2+} or Mg^{2+} on the interlayer sites of barlowite can be accomplished with significantly less disorder than seen in herbertsmithite

[34, 35]. Recent experimental reports have shown that the substitution of Zn^{2+} in the structure is possible and results in the possible formation of a spin liquid ground state [36, 37]. There are no reported methods for producing Zn substituted single crystals of synthetic barlowite suitable for single crystal neutron scattering studies.

Here we report the successful preparation of synthetic barlowite single crystals, with a technique that allows scaling to arbitrarily larger sizes. Using a combination of diffraction techniques complimented by magic angle spinning ^{19}F and ^{1}H NMR spectroscopy, we resolve the previously reported positional disorder of the interlayer Cu^{2+} ions in $Cu_4(OH)_6BrF$ and find that the appropriate crystallographic symmetry of the room temperature phase is orthorhombic, *Cmcm*. Infrared spectroscopy measurements of the O—H and F—H stretching frequencies demonstrate that the orthorhombic symmetry persists upon substitution of Zn^{2+} for Cu^{2+} at least up to a Zn^{2+} substitution of 0.46.

We also compare pure and Zn substituted barlowite, $Cu_{4-x}Zn_x(OH)_6BrF$, against the herbertsmithite compositional series, $Cu_{4-z}Zn_z(OH)_6Cl_2$, using specific heat and magnetic susceptibility measurements. Both series contain nearly perfect copper kagomé layers which are isolated from each other by interlayer ions. The striking similarities in the behavior of these two series implies a universality of the evolution of a QSL state on these materials despite the presence of small symmetry breaking distortions seen in synthetic barlowite. Thus synthetic barlowite provides a useful

comparison to probe the physics of synthetic Cu^{2+} kagomé minerals and the development of potential QSL states in such materials.

2.2 Experimental

2.2.1 Polycrystalline Synthesis

What is referred to as polycrystalline samples are large collections of very small single crystals each with typical volumes around 0.001 mm^3. Polycrystalline samples of $Cu_4(OH)_6BrF$ were grown through a hydrothermal reaction of 2 mmol copper carbonate basic (malachite $CuCO_3Cu(OH)_2$), with 4 mmol hydrobromic acid (HBr) and 4 mmol of ammonium fluoride (NH_4F) in 19 mL deionized water (DI H_2O) at 393K in a 23 mL Parr acid digestion vessel with PTFE liner for two to three days. At the end of the reaction the acid digestion vessels were removed from the furnace and allowed to cool in air to room temperature. It was also found that allowing the malachite and ammonium fluoride to react in the distilled water for 15 minutes before adding the HBr resulted in higher quality batches of polycrystalline sample, as did substitution of 3 mL of DI H_2O with 3 mL of ethanol (EtOH). Immediately following addition of HBr the vessels were sealed and the contents thoroughly mixed by shaking. Deuterated polycrystalline samples were grown in the same manner with the substitution of D_2O for DI H_2O, DBr for HBr and singly deuterated ethanol, EtOD (CH_3CH_2OD), for EtOH.

Zn^{2+} substitution was performed by including zinc carbonate basic (hydrozincite, $Zn_5(CO_3)_2(OH)_6$) at a 3:1 Cu:Zn ratio. The two samples measured using this method had 45.8(5)% and 46.3(5)% substitution of the interlayer copper site with zinc as determined by inductively coupled plasma mass spectrometry (ICP-MS). Additional hydrozincite in the reaction did not appear to improve the substitution of the interlayer site. Using 4 mmol of 1-Bromo-2,5-pyrrolidinedione in place of HBr with all other conditions the same as listed for the earlier Zn^{2+} substitution reaction resulted in a 6% substitution of the interlayer copper site with zinc, using 1 mmol did not produce a usable sample.

2.2.2 Single Crystal Growth

The synthesis of deuterated mm-scale single crystals was carried out through seeded, serial hydrothermal synthesis. There were two distinct stages to the growth of large single crystals: the first was used for cycles 1-14, the second was used for cycles 15-27.

1. Cycles 1-14

Initially 23 seed crystals, made using the polycrystalline method, with volumes around 0.004 mm^3 were placed in a 23 mL Parr acid digestion vessel with PTFE liner with 0.5 mmol $CuCO_3Cu(OH)_2$, 1 mmol NH_4F and 1 mmol DBr in 19 mL D_2O with a magnetic stir bar. The vessel was placed in a 393 K sand bath for 3 days with stirring before removing the vessel and allowing to cool to room temperature. After

each growth cycle the crystals were mechanically cleaned of smaller crystals attached to their surfaces, then rinsed with water and ethanol to remove powder that remained on the surfaces. This process resulted in crystals up to 0.04 mm^3. Attempts at further growth using this method reduced the quality of new growth.

2. Cycles 15-27

The crystals were resurfaced by etching with DBr followed by mechanical removal of surface material. Five crystals were tracked through subsequent growths as shown in Fig. 1. The same procedure as was used for cycles 1-14 was used with the following changes: (1) no stirring, (2) oven heating, and (3) replacement of 2 mL of D_2O with 2 mL of CH_3CH_2OD (EtOD). Following each cycle the crystals were mechanically cleaned and then sonicated in a 1:1 mixture of distilled water and ethanol to remove any powder that remained on the surface. This process was repeated using the crystals obtained from each prior cycle.

2.2.3 Characterization

The Cu:Zn ratio measured with an Agilent Inductively Coupled Plasma Mass Spectrometer with helium as the cell gas.

Powder x-ray diffraction (PXRD) data were collected at room temperature using a Bruker D8 Focus diffractometer with a LynxEye detector using Cu Kα radiation (λ = 1.5424 Å). Rietveld refinements on PXRD data were performed using Topas 4.2 (Bruker) [38]. Visualization was done in Vesta [39].

Single crystal X-ray diffraction (SXRD) data was collected at T = 110 K using the program CrysAlisPro (Version 1.171.36.32 Agilent Technologies, 2013) on a SuperNova diffractometer equipped with Atlas detector using graphite-monochromated Mo Kα (λ = 0.71073 Å). CrysAlisPro was also used to refine the cell dimensions and for data reduction. The temperature of the sample was controlled using the internal Oxford Instruments Cryojet. The structure was solved using SHELXS-97 and refined using SHELXL-97. [40]

Neutron powder diffraction data were collected using the BT-1 32 detector neutron powder diffractometer at the NCNR, NBSR. A Cu(311) monochromator with a 90° take-off angle, λ = 1.5397(2) Å, and in-pile collimation of 15 minutes of arc were used. Data were collected over the range of 3-168° *2-Theta* with a step size of 0.05°. The sample was loaded in a vanadium can sample container of length 50 mm and diameter 6 mm Data were collected under ambient conditions. Rietveld refinements were performed using GSAS [41] in EXPGUI [42].

Single crystal neutron diffraction (SND) data was collected on the TOPAZ beamline [43] at Oak Ridge National Laboratories Spallation Neutron Source at T = 100 K. Experiment planning [44, 45], visualization of data and indexing of the UB matrix was done using Mantid [46, 47, 48]. Data reduction and peak integration was done using ReduceSCD and anvred3. Refinement of single crystal neutron diffraction data was done using SHELXL-97 [40].

Synthetic barlowite samples were prepared for electron diffraction by grinding and dispersing the resultant power on a holey carbon coated Cu grid. Electron diffraction was performed using a Phillips CM300 atomic resolution transmission electron microscope with a field emission gun and an accelerating voltage of 300 kV operating in diffraction mode with a bottom mounted Orius SC1000A CCD detector and an exposure time of 3 seconds. Images were analyzed using ImageJ [49].

Magnetic susceptibility on powder samples and specific heat data using the short pulse semiadiabatic method on single crystals and pressed pellets were collected on a Quantum Design Physical Properties Measurement System (PPMS).

IR spectra were collected using an iD5 diamond ATR Accessory on a Thermo Scientific Nicolet iS5 FT-IR Spectrometer using OMNIC software. Allowed IR-active modes were determined using the Bilbao crystallographic server. [50]

The magic-angle spinning (MAS) NMR spectra were recorded in a $\mu_0 H = 4.7$ T magnetic field around room temperature (RT) with spin echo pulse sequence on a Bruker AVANCE-II spectrometer using home built MAS probe for 1.8 mm od rotors. The spinning speed of the sample was 40 kHz (therefore the real temperature is probably slightly higher than RT), ^{1}H resonance frequency was 200.06 MHz, with TMS reference. The ^{19}F resonance frequency was 188.25 MHz, with a CCl_3F reference. The computer fit was performed within Bruker Topspin program.

2.3 Results

Figure 2.3.1 (a) shows the change in size of five single crystals of $Cu_4(OH)_6BrF$ as a function of the number of growth cycles. The volume of each crystal grows quadratically with the number of cycles, Figure 2.3.1 (b), implying that significantly larger crystals are possible by this technique. The power law, shown in the inset, suggests that the growth rate is surface area limited.

PXRD measurements of ground single crystals and polycrystalline powders of $Cu_4(OH)_6BrF$ (not shown), and NPD measurements of polycrystalline $Cu_4(OD)_6BrF$

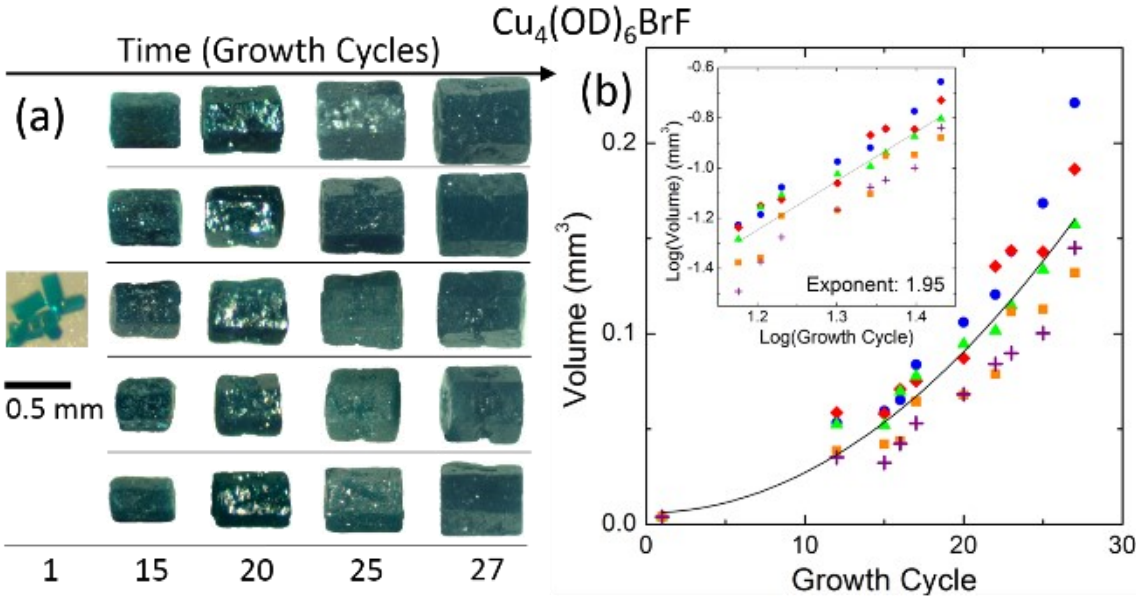

Figure 2.3.1 (a) The five largest deuterated crystals followed over time. (b) Volumes of the crystals over time, the inset is a log-log plot from growth cycle 15 to 27 showing that the exponent of the growth rate is ~2, suggesting the growth rate is limited by the surface area of each crystal.

(not shown) are in excellent agreement with previous reports, and are indexable with the previously reported *P6₃/mmc* hexagonal unit cell [21].

SXRD data were collected on single crystals of barlowite. Weak reflections, not indexable by the reported *P6₃/mmc* structure, are clearly visible in the precession images, Figure 2.3.2 (a,b). In addition, our SXRD data shows that some, but not all, observed reflections exhibit a high degree of mosaicity. The high mosaicity does not affect spots at random but appears to affect a subset of the reflections significantly more than others, which is potentially indicative of twinning. SND also produces reflections which cannot be indexed in *P6₃/mmc* but are well correlated to those observed in the SXRD precession images. The highest symmetry

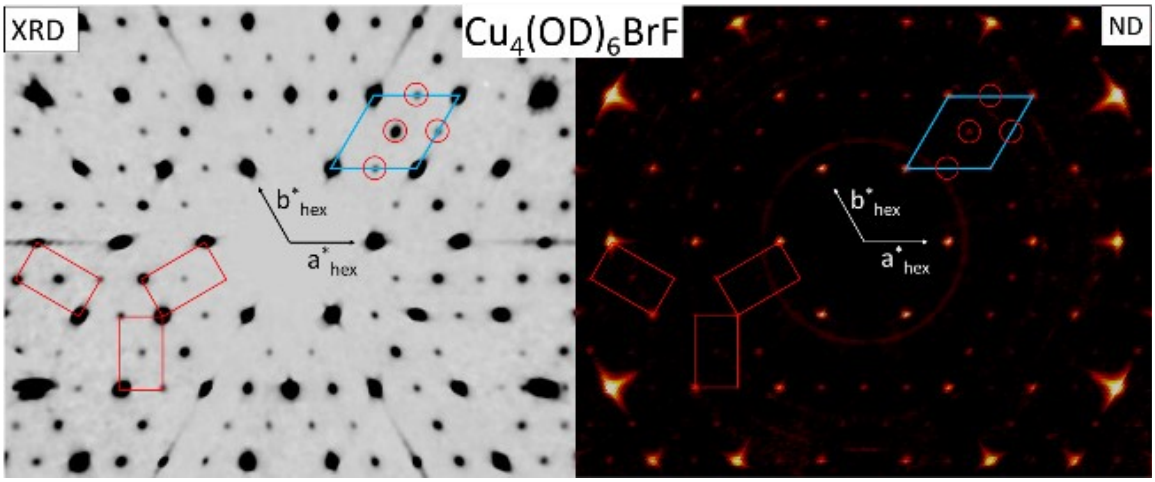

Figure 2.3.2. (left) SXRD precession image indexed in *P6₃/mmc* in the (hk0) plane. (right) SND reciprocal space layer image indexed in *P6₃/mmc* in the (hk0) plane. The blue rhombus shows the unit cell reported for *P6₃/mmc* with peaks that it does not index circled in red. The red rectangles show the unit cells for the three *Cmcm* twins by pseudomerohedry. The SND reflection intensities are shown on a logarithmic scale, visible as well are powder rings from the sample mount.

unit cell compatible with the SXRD and SND data is an orthorhombic cell, space

group *Cmcm*, with a = 6.67 Å, b = 11.52 Å, c = 9.26 Å. Inclusion of the appropriate twin law, ([-1 -1 0], [-0.5 -0.5 0], [0 0 -1] 3), allows this cell to index all observed reflections, with low mosaicity spots indexed by a single twin and high mosaicity spots indexed by multiple twins, Fig. 2.3.2 (a,b). This particular type of twinning by pseudomerohedry, with a *Cmcm* structure masquerading as the higher symmetry space group, $P6_3/mmc$, is well-known in related materials [51, 52]. Recent powder neutron studies of the low temperature structure of synthetic barlowite have also indicated an orthorhombic space group, proposed to be *Pnma*, from the evolution of magnetic peaks below T = 15 K, though we find *Pnma* unable to describe the room temperature structure [37].

There is a second way that the additional reflections observed in the SXRD data can be fit, an enlarged hexagonal unit cell with lower symmetry, such as $P6_3/m$. This was tested for using electron diffraction (ED) shown in Figure 2.3.3. ED measures a much smaller region of the sample than other diffraction methods and thus can resolve diffraction patterns from individual twin domains. The collected ED patterns are well indexed by the *Cmcm* cell and conclusively rule out a larger hexagonal cell with $P6_3/m$ symmetry as it cannot generate the observed diffraction data. Synthetic barlowite is susceptible to degradation in an electron beam and so more detailed analysis could not be made, although it should be noted that $P6_3/mmc$ does not fit the observed pattern of intensities.

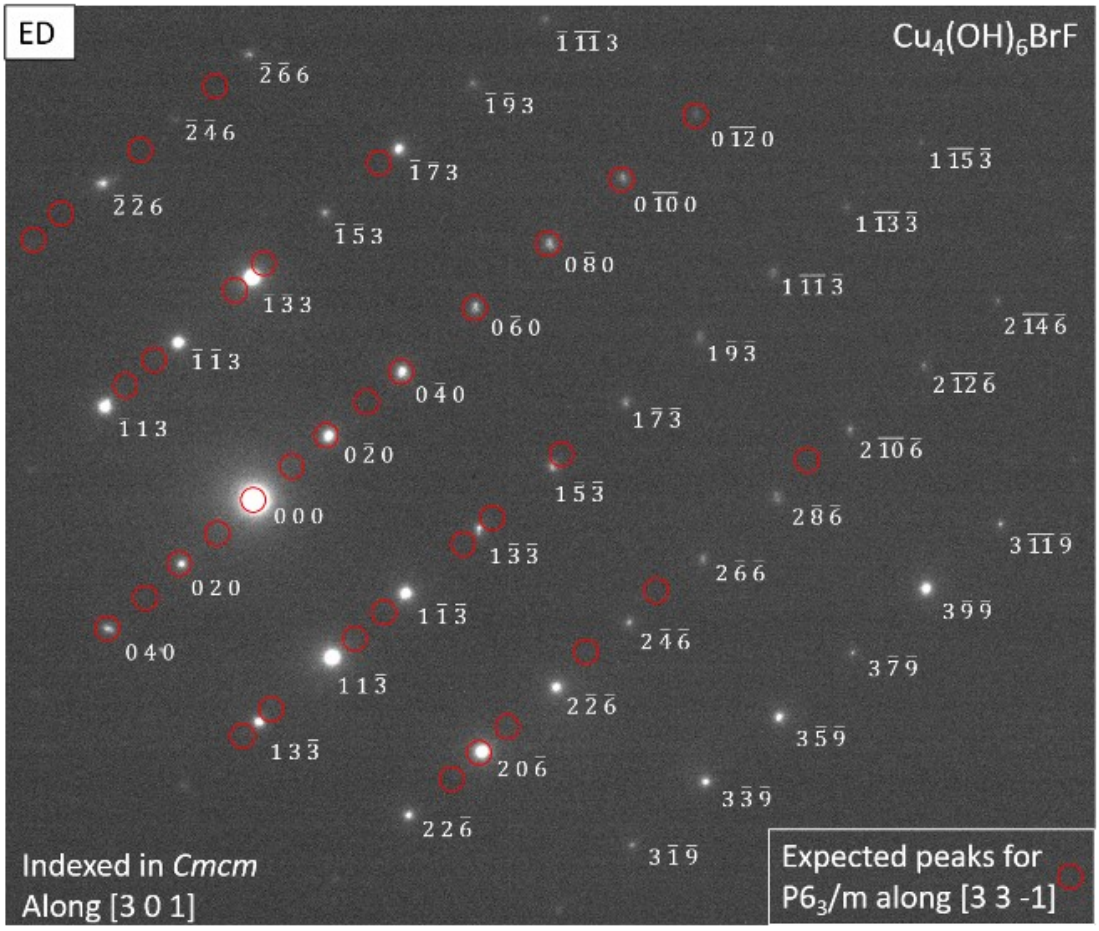

Figure 2.3.3. Electron diffraction pattern indexed to the *Cmcm* cell in white. Doubling the *a* and *b* axes of the reported *P6₃/mmc* and dropping the symmetry to *P6₃/m* cell results in expected bragg reflections (red circles) in poor agreement with the observed pattern.

The final structure of synthetic barlowite, from refinement of the SND data in the space group *Cmcm*, is given in Table 2.1. This model adequately describes the data from all diffraction measurements. For *Cmcm* the overall refinement parameter was $R(F_0) = 0.0603$ which is a significant improvement over the $R(F_0) = 0.0824$ obtained for the disordered *P6₃/mmc*, further supporting the choice of *Cmcm*. Lower symmetry subgroups of *Cmcm* were also examined but did not improve the

Table 2.3.1 Refinement of SND data to twinned *Cmcm*.

Space group		*Cmcm*		ρ_{calc}(g/cm^3)	4.31
a (Å)		6.665(13)		Z	4
b (Å)		11.521(2)		Total reflections	5939
c (Å)		9.256(18)		Unique Reflections	665
α (°)		90		Parameters	55
β (°)		90		R_{int}	0.1389
γ (°)		90		GooF	1.225
Temperature		100 K		$R(F_0)$	0.0603
Crystal Size (μm)		628x628x670		$R_w(F_o)^2$	0.1327
Atom	Site	*x*	*y*	*z*	U_{iso} (Å^2)
Cu(1)	4*b*	½	0	0	0.0114(16)
Cu(2)	8*d*	¼	¼	½	0.0124(9)
Cu(3)	4*c*	1	0.3713(4)	¾	0.0077(7)
Br	4*c*	0	0.3327(8)	¼	0.0143(11)
F	4*c*	0	0.9923(15)	¼	0.0127(12)
O(1)	8*f*	½	0.2979(8)	0.4125(9)	0.0099(13)
O(2)	16*h*	0.8045(9)	0.4010(5)	0.9052(5)	0.0107(7)
D(1)	8*f*	½	0.3762(7)	0.3696(13)	0.0258(19)
D(2)	16*h*	0.6865(1)	0.4374(7)	0.8656(5)	0.0244(10)

refinement (e.g. $P2_1/m$ with $R(F_0)$ = 0.0604 despite adding an additional 48 refineable parameters).

The *Cmcm* structural model is also in agreement with local measurements from magic-angle spinning (MAS) ^{1}H and ^{19}F NMR performed on a powder sample of synthetic barlowite. MAS suppresses line broadening from crystalline anisotropy and allows for greatly enhanced sensitivity to local structural orders. A typical MAS NMR spectrum consists of a resonance at an isotropic chemical shift value and several spinning sidebands at frequencies separated from the main line by a multiple of sample spinning frequency. One chemical shift should be observed for

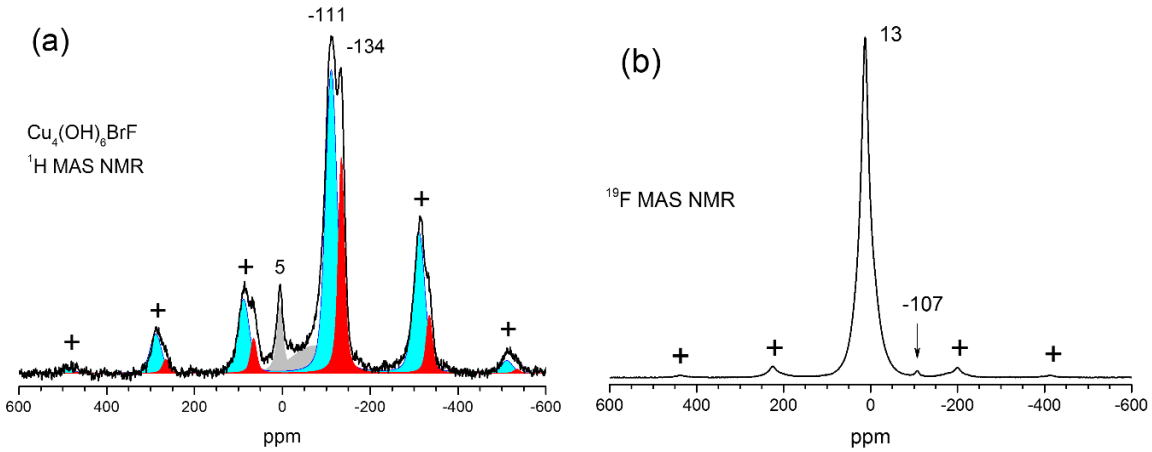

Figure 2.3.4 The x axis shows the measured chemical shift and the y axis is an arbitrary intensity. (a) ^{1}H MAS NMR spectrum of $Cu_4(OH)_6BrF$ powder sample showing two hydrogen resonance lines at -111 (cyan) and -134 ppm (red) together with their spinning sidebands noted by +. The intensity ratio of the two resonances is 70:30. The peak at 5 ppm and a broad line noted in gray represent a proton background of the probe. (b) ^{19}F MAS NMR spectrum of the same sample shows a single fluorine line with a small chemical shift of 13 ppm and a tiny resonance at -107 ppm of unknown origin.

each crystallographically independent atomic position. In the highly symmetry constrained hexagonal *P6₃/mmc* space group only a single isomer shift should be expected for ^{1}H. The ^{1}H MAS-NMR spectrum of $Cu_4OH)_6BrF$, Fig. 2.3.4 (a), clearly shows two distinct resonances at -111 ppm and -134 ppm, in addition to the spinning sidebands and a signal from probe background, making it inconsistent with *P6₃/mmc*.

The intensity ratio 70:30 of the two resonances, as found from the computer fit, is close to the ratio 4:2 expected for *Cmcm* structure. Distribution of the spinning sideband intensities yields considerable anisotropy of the chemical shift (here magnetic hyperfine shift) tensor. The principal values of the tensors are estimated

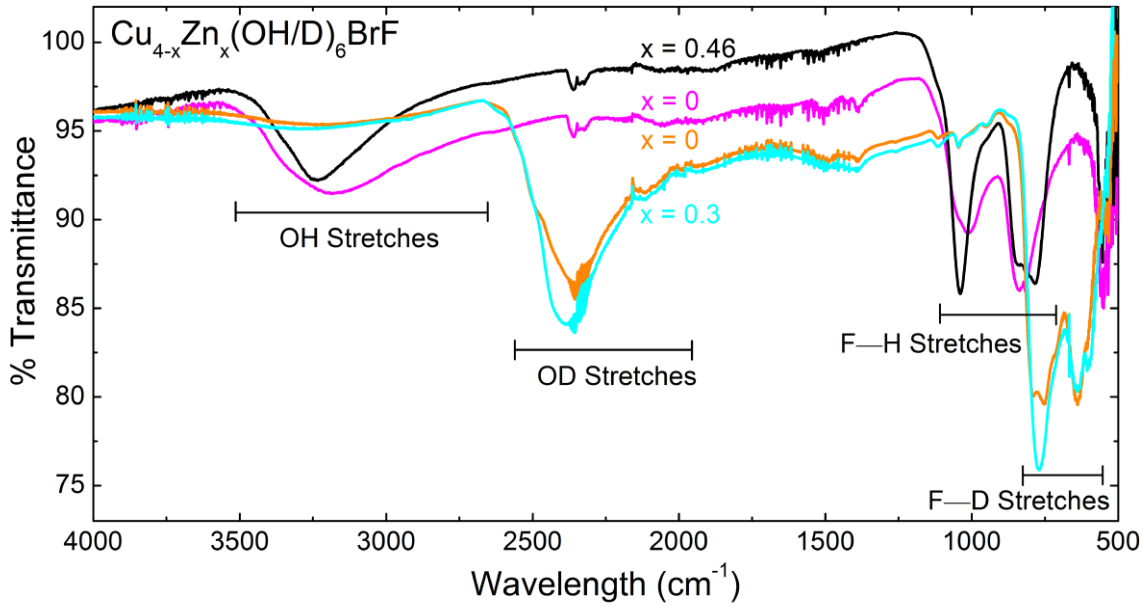

Figure 2.3.5 ATR-IR measurement reported in transmittance mode. Partial Zn^{2+} substitution is marked by a sharpening and a shift to higher wavenumber for the OH stretches and a shift to lower wavenumber for the F-H stretches.

Table 2.3.2 locations of transmittance minima of ATR-IR peaks

Sample	O-^{n}H peak	F—^{n}H peaks		
x=0, ^{1}H	3182 cm^{-1}	1044 cm^{-1}	1012 cm^{-1}	839 cm^{-1}
x=0.4, ^{1}H	3236 cm^{-1}	1039 cm^{-1}	840 cm^{-1}	781 cm^{-1}
x=0, ^{2}H	2350 cm^{-1}	789 cm^{-1}	752 cm^{-1}	639 cm^{-1}
x=0.3, ^{2}H	2382 cm^{-1}	770 cm^{-1}	639 cm^{-1}	601 cm^{-1}

as {310, -300, -345} ppm and {210, -295, -315} ppm for the two lines. The ^{19}F MAS-NMR spectrum, Fig. 4(b) shows a single fluorine resonance in agreement with the *Cmcm* structure. In both ^{1}H and ^{19}F measurements, there is broadening beyond the expected instrumental resolution. In magnetic materials this is caused usually by the magnetic susceptibility of the powder particles [53]. Further the observed ^{1}H chemical shifts agree with the structure from SND: D1 (8 per cell) has closer Cu^{2+} and F^{-} ions than D2 (16 per cell) and should therefore have a larger hyperfine shift.

Thus, the stronger line at -111 ppm should belong to D2 sites and the weaker line at -133 ppm belongs to D1, as expected from the ratios of intensities.

We found that measurement of Γ-point phonon modes by attenuated total reflection infrared spectroscopy (ATR-IR) was a versatile measurement technique to probe the symmetry of synthetic barlowite when doped with Zn, i.e. $Zn_xCu_{4-x}(OH)_6BrF$. Representative data for hydrogenated and deuterated samples at x = 0, 0.3, and 0.4 are shown in Figure 2.3.5. Absorption bands for O—H(D) and F—H(D) are clearly resolved at 3200 cm^{-1} (2400 cm^{-1}) and 1000 cm^{-1} (700 cm^{-1}) respectively, and tabulated in Table 2.2.

In *P6₃/mmc* there should only be two modes observable in IR related to the F—H(D) stretches, $1E_{1u} + 1A_{2u}$, however three distinct absorption peaks are clearly resolved. The observation of three IR active modes related to the F—H(D) stretches is expected for the *Cmcm* structure, as the reduction in symmetry results in $B_{1u} + B_{2u} + B_{3u}$ modes for the F—H(D) stretches, consistent with the observed data. The clustering of two of these three modes close together is also expected, as the *Cmcm* structure is very close to having the higher $P6_3/mmc$ symmetry. Zinc substitution is found to slightly reduce the stretching frequencies, as expected, but does not change the number of observed modes. This implies that up to x = 0.5, the orthorhombic symmetry is maintained at room temperature. The significant broadening in the O—H(D) region precludes detailed analysis, but the overall shape is consistent with expectations for the *Cmcm* structure.

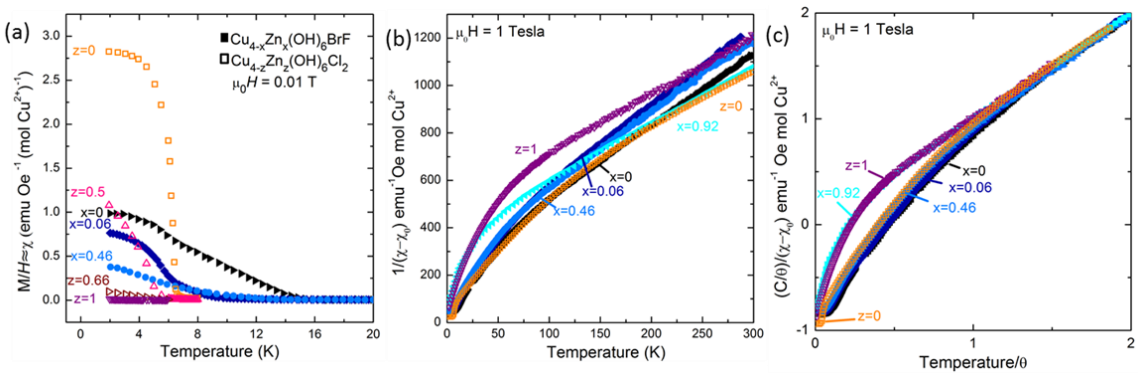

Figure 2.3.6 Symbols and colors are consistent for (a) through (c). Solid symbols represent $Cu_{4-x}Zn_x(OH)_6BrF$ data going from black to light blue with increasing zinc content. Hollow symbols represent $Cu_{4-z}Zn_z(OH)_6Cl_2$ data going from orange to purple with increasing zinc content. (a) χ_{mol} for Zn^{2+} substitution series of barlowite compared to the herbertsmithite series. (b) Curie-Weiss analysis of all data sets. (c) Inverse susceptibility normalized for $C/|\theta|$ versus $T/|\theta|$, highlighting universal behavior at low x, z and high x, z. Data for z = 0, 0.5 0.66 from ref. [20, 54], data for x = 0.92 from ref. [36]. For (a), data for z = 1 from [20].

To explore similarities and differences between these two quantum spin liquid candidates, DC magnetization measurements on powder samples of the Zn substituted barlowite series were carried out from T = 2-300K. A comparison of the susceptibility, estimated as $\chi \approx M/H$, to literature data on the synthetic herbertsmithite family, measured at $\mu_0H = 0.01$ T is shown in Fig. 6(a). In synthetic barlowite, Zn^{2+} substitution suppresses both the magnitude of the ferromagnetic response at low temperature, and the temperature of the transition. This is similar to the behavior of $Zn_zCu_{4-z}(OH)_6Cl_2$, although the suppression of the ordering temperature is more pronounced in the case of $Zn_xCu_{4-x}(OH)_6BrF$.

Curie-Weiss analysis of the high temperature regime of each $Zn_xCu_{4-x}(OH)_6BrF$ sample is shown in Figure 2.3.6 (b), with corresponding parameters in Table 2.3.

Table 2.3.3. Values from the Curie Weiss analysis. Linearized between 150 and 300K with the exception of z = 0 sample which was linearized between 200 K and 300 K. Values for z = 0, x = 0.92 done from reanalysis of data in refs. [54] and [36]

Sample	C	θ (K)	χ_0
x = 0	0.34	-78	1.5E-4
x = 0.06	0.31	-82	1.1E-4
x = 0.46	0.32	-89	9E-5
x = 0.92	0.42	-153	9E-5
z = 0	0.43	-155	3E-5
z = 1	0.42	-200	-6E-5

Increased Zn substitution lowers the temperature at which deviations from the Curie-Weiss law are observed, and the observed Weiss temperature becomes more negative. The Weiss temperatures of the barlowite series are a factor of ~2 smaller than that of herbertsmithite, suggesting ~two times weaker in-plane magnetic interactions.

The normalized plot of Fig. 2.3.6 (c) provides a more meaningful comparison between synthetic barlowite and synthetic herbertsmithite. For $T/|\theta| > 1$, all curves follow linear behavior, as expected. Deviations from Curie-Weiss behavior are observed below $T/|\theta| = 1$ for all samples except the endmembers of both the herbertsmithite and barlowite Zn^{2+} substitution series in which deviation occurs around $T/|\theta| < 0.3$. This suggests that interactions between kagomé and interlayer copper ions are crucial in governing the observed magnetic behavior.

Zero field heat capacity (HC) measurements for T = 1.8 K to 300K further highlight the similarities between the two material families. As non-magnetic

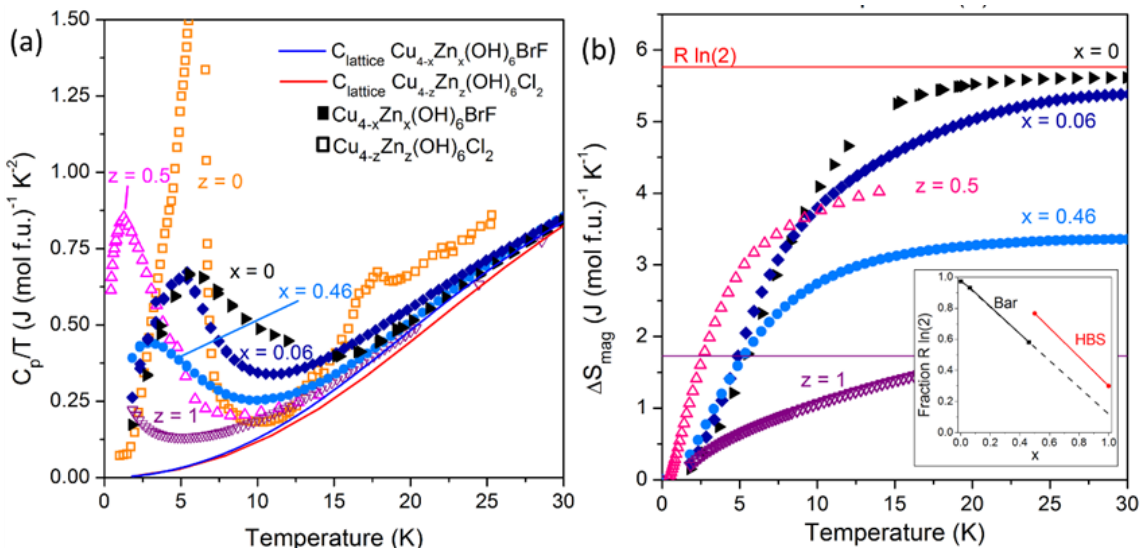

Figure 2.3.7 Symbols and colors are consistent for (a) and (b). Solid symbols represent $Cu_{4-x}Zn_x(OH)_6BrF$ data going from black to light blue with increasing zinc content. Hollow symbols represent $Cu_{4-z}Zn_z(OH)_6Cl_2$ data going from orange to purple with increasing zinc content. (a) Heat capacity divided by temperature as a function of temperature under zero field for the barlowite substitution series compared to members of the herbertsmithite series. barlowite shows a similar shift in its antiferromagnetic transition towards lower temperature as seen in the herbertsmithite series. Approximated lattice contributions are shown in blue for barlowite and red for herbertsmithite. The data for the z = 0 series is cut off peaking at 3.5 J mol^{-1} K^{-2}. Data for z = 0 from ref. [54] and data for z = 0.5 from ref. [23] (b) Recovered magnetic entropy as a function of temperature is shown for both series, with R ln(2) shown at the top and a line showing the total recovered entropy for z = 1 where it is cut off by the inset. The inset shows the recovered entropy as a fraction of R ln(2) with the barlowite series in black and the herbertsmithite series in red compared to the measured molar fraction of zinc with the dashed line projected from the linear behavior at the substitution levels measured, the projected remnant magnetic entropy at full substitution is significantly less than seen in herbertsmithite.

structural analogs are unknown, the high temperature data, T = 25-300K, was fit to a three component Debye model to estimate the lattice contributions. The lattice contributions estimated in this manner are shown as solid lines in Fig. 7(a). There are numerous similarities and differences between the two series.

The only material to show a sharp lambda anomaly, indicative of a proper phase transition, is $Cu_4(OH)_6Cl_2$. In contrast, $Cu_4(OH)_6BrF$ only shows a broad hump below the T = 15 K transition seen by magnetization measurements. This likely reflects the high degree of twinning found in synthetic barlowite, and matches the behavior of $Zn_zCu_{4-z}(OH)_6Cl_2$ for $z>0.33$ [20]. Similarly broad phase transitions have been observed in related materials with disorder including $FeSc_2S_4$ [55] and $Yb_2Ti_2O_7$ [56].

In both materials families, the observed low temperature peak in C_p/T shifts to lower temperatures and decreases in magnitude as Zn^{2+} substitution increases. Subtraction of the approximated lattice contribution and integration of C_p/T vs. T yields estimates for the changes in magnetic entropy at low temperature in each sample shown in Figure 2.3.7 (b). $Cu_4(OH)_6BrF$ recovers very near R ln(2) in magnetic entropy. This suggests that only ¼ of the Cu ions lose their entropy at the T = 15 K transition. It is thus alluring to attribute the ordering in synthetic barlowite as arising from the interlayer Cu^{2+} (1/4 of all Cu ions). As Zn^{2+} is substituted, the recovered magnetic entropy is suppressed in a manner very similar to what is seen in synthetic herbertsmithite. The non-zero low temperature magnetic entropy in z = 1 $Zn_zCu_{4-z}(OH)_6Cl_2$ is attributed to the residual Cu^{2+} known to exist on the interlayer site [29]. Comparing the recovered entropy against the measured ratio of Cu to Zn from ICP-MS provides an indirect indication of the site selectivity of the Zn substitution. Promisingly for the barlowite series the recovered entropy far more

closely matches the measured Zn^{2+} substitution than that seen in the herbertsmithite series as shown by the inset in Fig. 2.3.7 (b), suggesting more selective substitution at the interlayer position.

2.4 Discussion

Figure 2.4.1 shows a comparison of the orthorhombic *Cmcm* structure of $Cu_4(OH)_6BrF$ to the previously reported, disordered, *P6₃/mmc*, model. Both structures share virtually identical kagomé layers, and in both, the trigonal prismatic coordination of the interlayer ions is highly unfavorable for either Cu^{2+} or Zn^{2+}, requiring a displacement of the interlayer ion from its "ideal" position within the center of the trigonal prism into a distorted octahedral position. In *P6₃/mmc* there are three equivalent distorted octahedral sites available to each interlayer copper and it is disordered across them.

The impact of the *Cmcm* model is very similar, but symmetry constraints no longer enforce the degeneracy of these three sites. The result is the ordering of the interlayer coppers into distinct positions. This ordering is coupled to a change in bonding of the fluorine atoms that sit in the hexagonal channels. In the previously reported structure, the F^- ion sits in the center of a cage of OH^- ions, with no direct bonding to any neighbors. This chemical coordination is extremely rare, having previously only been observed in a highly constrained zeolite [57]. If instead of being constrained to the center of the channel, the F^- ions displace towards a pair of

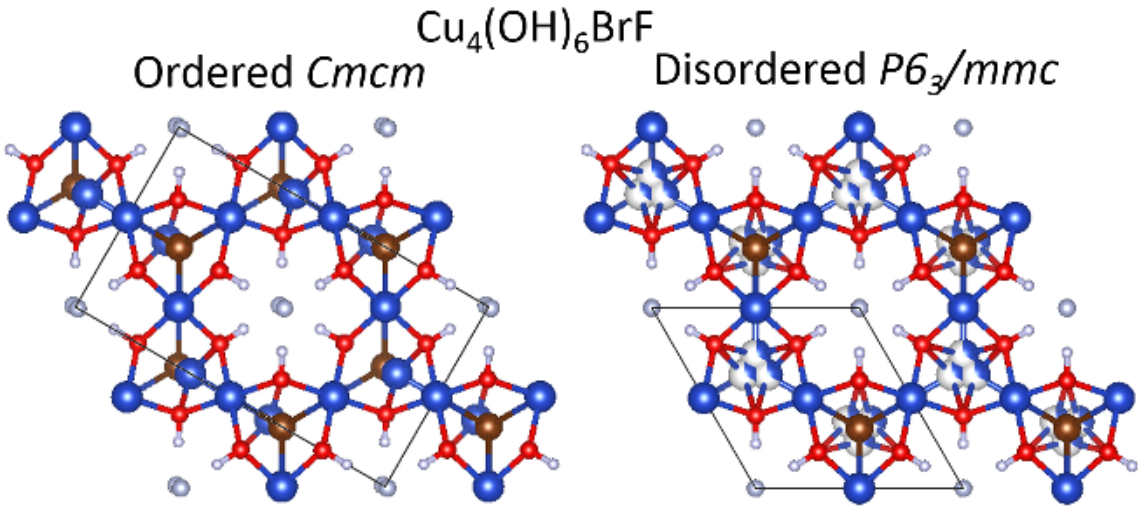

Figure 2.4.1 Shown along the c-axis of the lattice is (left) the ordered *Cmcm* structure, and (right) the previously reported disordered *P6₃/mmc* structure [19]. The *Cmcm* structure results in local ordering of the interlayer coppers (blue) and distortion of the fluorine (white, center of channels) towards one pair of hydrogens (white, attached to oxygen atoms, red).

OH^- ions, it can form optimal H—F hydrogen bonds. This is exactly what happens in the *Cmcm* structure, with corresponding motions of the interlayer Cu^{2+} ions to accommodate the change in OH positions.

Remarkably, despite this deviation from perfect hexagonal symmetry, the physics of the kagomé layers appears mostly undisturbed, as seen in the comparison to the behavior of the herbertsmithite series. Since the gapped quantum spin liquid should be a stable phase on the kagomé lattice, it is not surprising that it should be stable against a small structural change.

While more work will be needed to fully characterize the $Cu_{4-x}Zn_x(OH)_6BrF$ substitution series, indirect evidence from recovered magnetic entropy suggests Zn substitution occurs with less disorder than observed in the herbertsmithite. This

suggests that synthetic barlowite may allow the QSL state to be probed with fewer complications from remnant magnetic impurities than herbertsmithite. This work also demonstrates the viability of serial hydrothermal synthesis in the production of large single crystals, which makes possible the synthesis of large single crystals of Zn substituted barlowite sufficient to allow future inelastic neutron scattering studies of the QSL state in this promising material.

2.5 Acknowledgements

We acknowledge stimulating discussions with Collin Broholm. We thank Maxime Siegler for assistance with the single crystal x-ray diffraction measurements, Craig Brown for assistance with the powder neutron diffraction measurements, and R. Campbell-Kelly at the Westinghouse Electric Company Columbia Fuel Fabrication Facility for performing ICP-MS measurements. Work at the Institute for Quantum Matter was supported by the U.S. Department of Energy, Office of Basic Energy Sciences, Division of Material Sciences and Engineering under grant DEFG02-08ER46544. A portion of this research used resources at the Spallation Neutron Source, a DOE Office of Science User Facility operated by the Oak Ridge National Laboratory. We acknowledge the support of the National Institute of Standards and Technology, U. S. Department of Commerce, in providing the powder neutron diffraction facilities used in this work. Certain commercial equipment, instruments, or materials are identified in this paper to foster understanding. Such identification does not imply recommendation or endorsement

by the National Institute of Standards and Technology, nor does it imply that the materials or equipment identified are necessarily the best available for the purpose. This research used resources of the Advanced Photon Source, a U.S. Department of Energy (DOE) Office of Science User Facility operated for the DOE Office of Science by Argonne National Laboratory under Contract No. DE-AC02-06CH11357. TMM acknowledges support of the David and Lucile Packard Foundation. I.H. and R.S. are supported by the Estonian Research Agency grants IUT23-7 and PRG4, and the European Regional Development Fund project TK134.

3. Tunable Magnetic Transition to a Singlet Ground State in a 2D Van der Waals Layered Trimerized Kagomé Magnet

This work was co-written with the following authors and is published under the following citation:

ACS Nano **13**, 8, 9457-9463 (2019)

https://doi.org/10.1021/acsnano.9b04392

Christopher M. Pasco[1,2], Ismail El Baggari[3], Elisabeth Bianco[4], Lena F. Kourkoutis[4,5], Tyrel M. McQueen[1,2,6,*]

[1]Department of Chemistry, The Johns Hopkins University, Baltimore, MD 21218, United States

[2]Institute for Quantum Matter, Department of Physics and Astronomy, The Johns Hopkins University, Baltimore, MD 21218, United States

[3]Department of Physics, Cornell University, Ithaca, NY 14853, United States

[4]Kavli Institute at Cornell for Nanoscale Science, Cornell University, Ithaca, NY 14853, United States

[5]School of Applied and Engineering Physics, Cornell University, Ithaca, NY 14853, United States

[6]Department of Materials Science and Engineering, The Johns Hopkins University, Baltimore, MD 21218, United States

3.1 Introduction

The discovery of graphene has recently sparked a surge of interest in other two dimensional (2D) semiconductors, such as MoS_2 and other transition metal dichalcogenides (TMDs), which exhibit a variety of properties that can be exploited in the production of devices [58]. One feature that makes these materials particularly desirable is that their layers are stacked by Van der Waals (VdW) forces which can make exfoliation relatively trivial. Variations in the basic properties of the atoms used within the family of TMDs have led to a range of potential applications [58]. Generically, TMDs share similar band structures, a lack of magnetic behaviors, and complex phenomena associated with quantum materials. One way to gain access to magnetic physics is to look at 2D semiconductors outside of the TMD family. One such potential variation is the trimerized kagomé magnet, in which metallic clusters of atoms carry a net magnetic moment and are embedded in a larger lattice with low dimensional exchange pathways between them [59].

Geometrically frustrated magnetic materials are those in which magnetic units are embedded in a lattice in such a way that there is not a single lowest energy configuration of spins. When the interactions between these spins is strong, the inability to satisfy competing exchanges can, to avoid long range order, result in the formation of exotic ground states such as valence bond solids [13], and spin liquids [14]. They can also drive significant structural distortions to break the frustrating symmetry such as dimerization in the spin-Peierls distortion [60]. Recently,

significant interest has revolved around 2D magnetic materials, including single layer ferromagnets such as CrI_3 [61] and Fe_3TeGe_2 [62], and the Kitaev spin liquid candidate α-$RuCl_3$ [63]. Typically, the magnetic units are spins localized to individual ions, however, this is not true in the case of the trimerized kagomé magnet, where the free spins are delocalized across a metal-metal bonded cluster of ions, such as in $LiZn_2Mo_3O_8$ [64, 65].

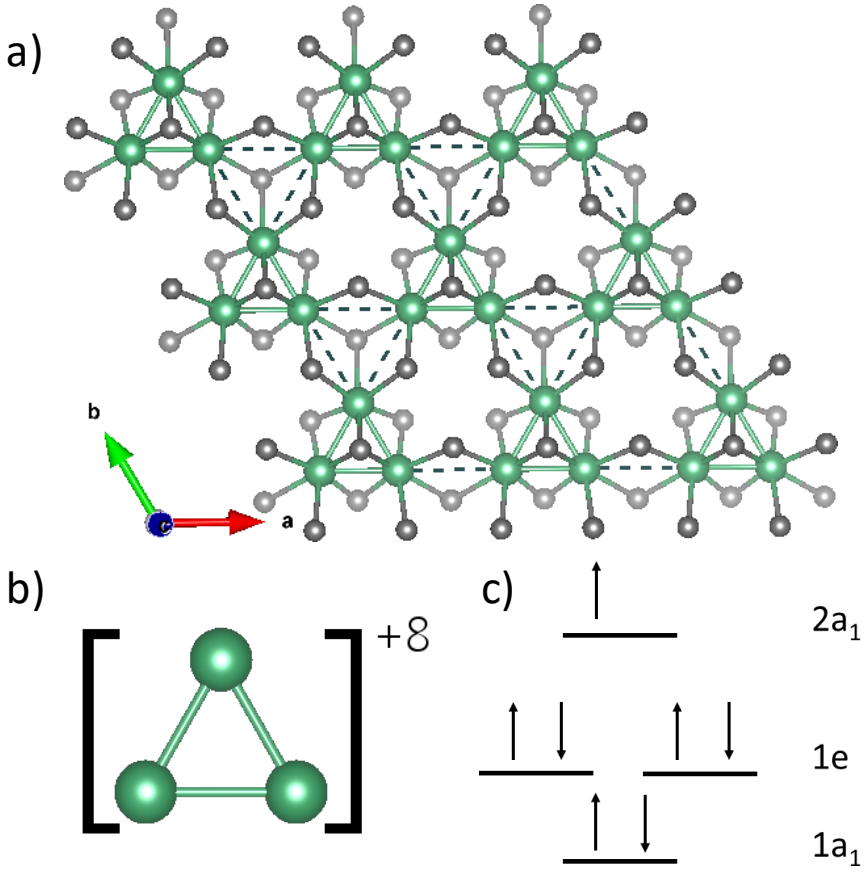

Figure 3.1.1 a) Single layer of Nb_3X_8 showing the trimerized kagomé structure of individual layers. The Nb atoms (green) are connected by a solid line showing the metal-metal bonds and a dashed grey line indicating unbonded triangles. Dark grey atoms are halides above the plane of Nb_3 clusters, and light grey atoms are halides below the plane. b) An individual Nb_3 cluster and its charge. c) Simplified molecular orbital diagram for the cluster showing a single unpaired electron.

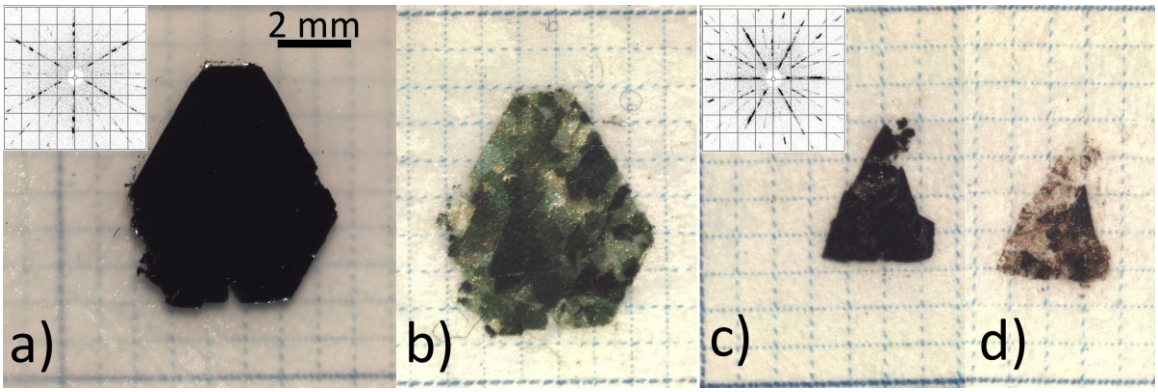

Figure 3.1.2 a) and c) are first exfoliations of Nb_3Cl_8 and Nb_3Br_8 crystals, respectively on a 1 mm grid, with backscatter Laue diffraction patterns of each in the (hk0) plane included as insets. b) and d) show the same samples after repeated exfoliations until they were thin enough to transmit light.

Originally reported in the 1960s [66-68], the Nb_3X_8 family of materials hosts a trimerized kagomé lattice, in which each Nb_3 trimer is held together by strong metal-metal bonds, sharing a single unpaired electron, as seen in Figure 3.1.1. These effective S = ½ units are arranged in a geometrically frustrated triangular network. In 1992 it was reported that Nb_3Cl_8 undergoes a magnetic phase transition around T = 90 K [69]. At room temperature Nb_3Cl_8 behaves like a paramagnet, undergoing a first order phase transition to an apparently non-magnetic, *i.e.*, singlet, low temperature phase [70, 71]. Individual layers are only weakly bound to each other by VdW interactions, and as a consequence these materials are also readily exfoliatable as seen in Figure 3.1.2.

In this article, we report the discovery that Nb_3Br_8 also undergoes a magnetic transition from a high temperature paramagnetic phase to a singlet phase above room temperature, at T = 382 K. In addition, for the continuous solid solution $Nb_3Cl_{8-x}Br_x$, the temperature of this phase transition can be tuned from T = 92 K to

T = 387 K. The UV-visible optical absorption peaks are also systematically varied. Single crystal X-ray diffraction (SXRD) shows that the magnetic transition from the high temperature, paramagnetic state (α phase) to the low temperature, singlet state (β phase) is accompanied by a rearrangement of the stacking sequence between VdW layers of the native heterostructure. This is consistent with the results of atomic resolution scanning transmission electron microscopy (STEM) imaging of the end members α-Nb_3Cl_8 and β-Nb_3Br_8. Thus, the Nb_3X_8 family represents a group of 2D-exfoliatable materials with magnetic and optical properties tunable over a range that includes room temperature and visible light, making it potentially useful for the production of devices.

3.2 Results and Discussion

3.2.1 Structure (SXRD and STEM)

The structures of both α-Nb_3Cl_8 and β-Nb_3Br_8 are well known [66, 68]. As referenced earlier, α-Nb_3Cl_8 is known to undergo a phase transition at T = 92 K to a non-magnetic β phase, however, the exact description of the structure of this low temperature phase has varied between reports. This is likely due to significant remnants of the high temperature phase as stacking faults after the transition [70]. For Nb_3Br_8 has been reported that an α variant isostructural to α-Nb_3Cl_8 was occasionally found in samples grown at T = 400 K, though it does not appear to have been extensively studied [67]. It is worth noting that this is very close to the temperature at which β-Nb_3Br_8 was found to transition into a high temperature phase

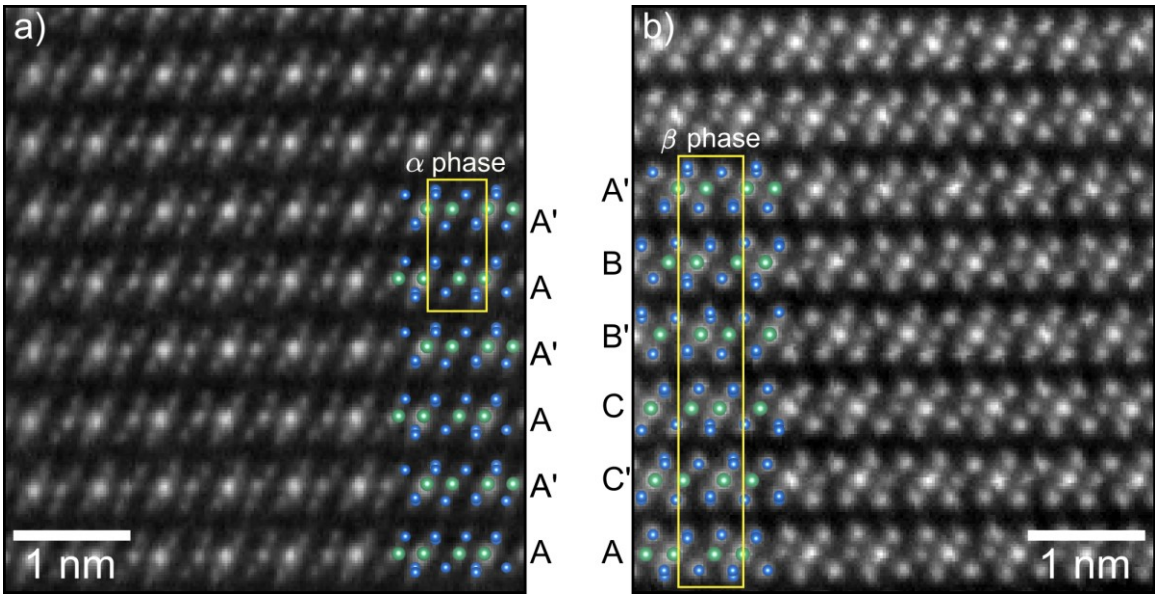

Figure 3.2.1. a) STEM image of α-Nb_3Cl_8 along (100) at T = 93 K with structural overlay. d) STEM image of β-Nb_3Br_8 along (100) showing the low temperature beta phase at T = 300 K with structural overlay. Unit cells are indicated by the yellow rectangles for each phase. In the structural overlays Nb atoms are shown in green and the halides in blue. Brighter spots in the Nb rows in the STEM images are where two Nb atoms in the unit cell are overlaid in this projection, while the dimmer spot comes from a single Nb atom per unit cell.

in this work. This suggests that poor crystallinity due to the low temperature synthesis conditions may have trapped Nb_3Br_8 in its high temperature phase.

Given the apparent tunability of the transition temperature with stoichiometry, $Nb_3Cl_4Br_4$ was selected to study the high and low temperature phases with single crystal x-ray diffraction (SXRD). The high temperature phase α-$Nb_3Cl_4Br_4$ undergoes its transition to β-$Nb_3Cl_4Br_4$ at T = 194 K, so diffraction patterns were taken of the same crystal at T = 300 K and T = 110 K. It was found that the high temperature phase was isostructural to α-Nb_3Cl_8 (Table 3.2.1) and the low temperature structure was isostructural to β-Nb_3Br_8 (Table 3.2.2). Chlorine and bromine were restricted to occupy identical positions within the structure and their

Table 3.2.1 Abbreviated refinement parameters for α-$Nb_3Cl_4Br_4$ refined with anisotropic thermal parameters

MW (g/mol)	740.15	Z	2
Crystal System	Trigonal	Temperature	293 K
Space Group	*P-3m1*	λ (Å)	0.71073
Color	black	Total refl.	16834
$a = b$ (Å)	6.9133(2)	Unique refl.	930
c (Å)	12.7267(3)	Parameters	29
α (°)	90	R_{int}	0.0393
β (°)	90	GooF	1.289
γ (°)	120	$R(F_o)$	0.0164

Table 3.2.2 Abbreviated refinement parameters for β-$Nb_3Cl_4Br_4$ refined with anisotropic thermal parameters.

MW (g/mol)	740.15	Z	6
Crystal System	Trigonal	Temperature	110 K
Space Group	*R-3m*	λ (Å)	0.71073
Color	black	Total refl.	3289
$a = b$ (Å)	6.9034(4)	Unique refl.	222
c (Å)	38.035(2)	Parameters	29
α (°)	90	R_{int}	0.0290
β (°)	90	GooF	1.253
γ (°)	120	$R(F_o)$	0.0121

occupancies were allowed to refine with the restraint that each site would remain fully occupied. The structures determined by SXRD for the high and low temperature phases, along with the average site occupancies, can be seen in Figure 3.2.2a for the high temperature phase and 3.2.2b for the low temperature phase. Highlighted there is the fact that the low temperature phase can be thought of as pairs of layers in the same arrangement as the high temperature phase which are then staggered with each other as to produce a 6 layer unit cell. Labels for the β-phase in Figure 3.2.1 are chosen to preserve the layer orientation and arrangement of the α-phase to allow useful comparison. Cross-sectional STEM imaging of the

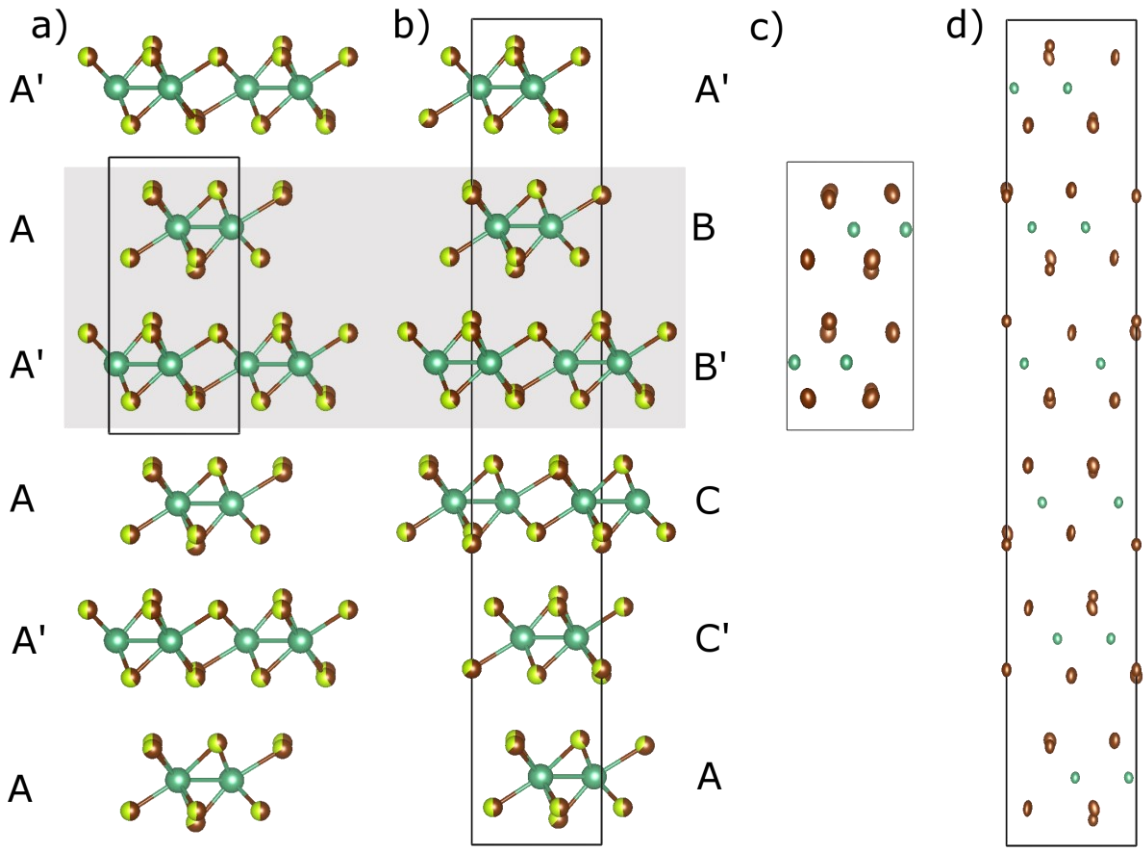

Figure 3.2.2 a) High temperature alpha phase showing AA' stacking of $Nb_3Cl_4Br_4$. b) Low temperature beta phase showing AA'BB'CC' stacking of $Nb_3Cl_4Br_4$. The highlighted pair of layers show how the β phase consists of staggered pairs of layers related to each other by the AA' stacking seen in the α phase, also demonstrated by the labeling scheme used. Green represents niobium, yellow is chlorine and brown is bromine. c) and d) show the unit cells with anisotropic thermal parameters for the α and β phases respectively. The stoichiometry for the particular sample used, determined from the high temperature SXRD was $Nb_3Cl_{3.99}Br_{4.01}$.

end members, Nb_3Cl_8 and Nb_3Br_8, directly shows the staggering of the layers in the alpha and beta phase, respectively. In this orientation, the metal atomic columns exhibit two intensity values in STEM, with the bright columns containing more Nb atoms in projection.

Since the SXRD data was taken on a single crystal, it could be used to elucidate some details about the mechanism of the transition. The relationship between the

Table 3.2.3 Bromine site occupancies determined through single crystal x ray diffraction for α and β $Nb_3Cl_4Br_4$. There are 4 unique halide sites for both the α and β phases of the Nb_3X_8 family of materials. Two of the sites are replicated only once per formula unit and are the intracluster and intercluster capping halides. The other two sites are replicated three times per formula unit and each serve to bridge a pair of Nb atoms. These sites are the intracluster and intercluster bridging halides. The occupancies found for these sites in the mixed halides serve as unique chemical tag in single crystal x-ray diffraction, allowing a single sample to be tracked above and below its transition temperature to provide some restraints on the mechanisms by which the transition can occur. The small discrepancies between α and β are likely due in part to the rough absorption correction on the β phase data and consequences of the stacking faults seen in the low temperature phase.

Phase	α-$Nb_3Cl_4Br_4$	β-$Nb_3Cl_4Br_4$
Intracluster cap	0.6485	0.6462
Intercluster cap	0.6617	0.6580
Intercluster bridge	0.5021	0.5035
Intracluster bridge	0.3975	0.4020

individual halide sites and the Nb_3 trimers could be tracked as the halide substitution is not entirely random. The reason for this is believed to be the different potentials for each of the four unique halide sites in the structure, which plays a defining role in the site selectivity of chalcogenide substitution in the Nb_3QX_7 (Q = S, Se, Te; X = Cl, Br, I) family of materials.[16] Only one halide site in the structure of the high temperature phase is chlorine rich, which are the intracluster bridging halides, with occupancies provided in table 3.2.3. In the beta phase the intracluster bridging halides remain the sole chlorine rich site in dictating that the transition must be a mechanical shift of the individual layers and not a change in chemical bonding of individual layers by passing through a kagomé structure from one trimerized kagomé to the other.

3.2.2 Magnetic Susceptibility

Previous work [70] has shown negligible orientation dependence on magnetic susceptibility for Nb_3Cl_8, therefore samples were prepared as described in the methods section depending on instrument requirements to probe different temperature ranges and the data was combined into Figure 3.2.3. Above T = 300 K susceptibility data was collected on oriented single crystals and below T = 300 K data was collected on randomly oriented assemblages of single crystals. Contributions from the sample holder were subtracted out by measuring a blank.

The magnetic susceptibility of the high temperature phase of the series can be approximately fit to a single universal Curie-Weiss curve, $\chi_{f.u.} = C/(T-\theta) - \chi_0$, which can be seen in Figure 4. This curve for the series average yields a Weiss temperature of θ = -23.0(1.0) K and a Curie constant C = 0.376(4) emu • K • Oe^{-1} • mol f.u.$^{-1}$, which corresponds to an effective moment, p_{eff} = 1.733(9) μ_B, consistent with S_{eff} = ½. While this universal curve qualitatively does a good job at describing the susceptibility over the entire range of x in $Nb_3Cl_{8-x}Br_x$, it is difficult to tell how closely these values, particularly θ, might conform to the individual fits. As a consequence of the small overall moment, S = ½ per Nb_3X_8 unit, significant uncertainties in θ result from a high sensitivity of the calculated θ to small changes in χ_0 as the susceptibility becomes nearly linear at higher temperatures. The low temperature phase is accompanied by an almost total loss of magnetization,

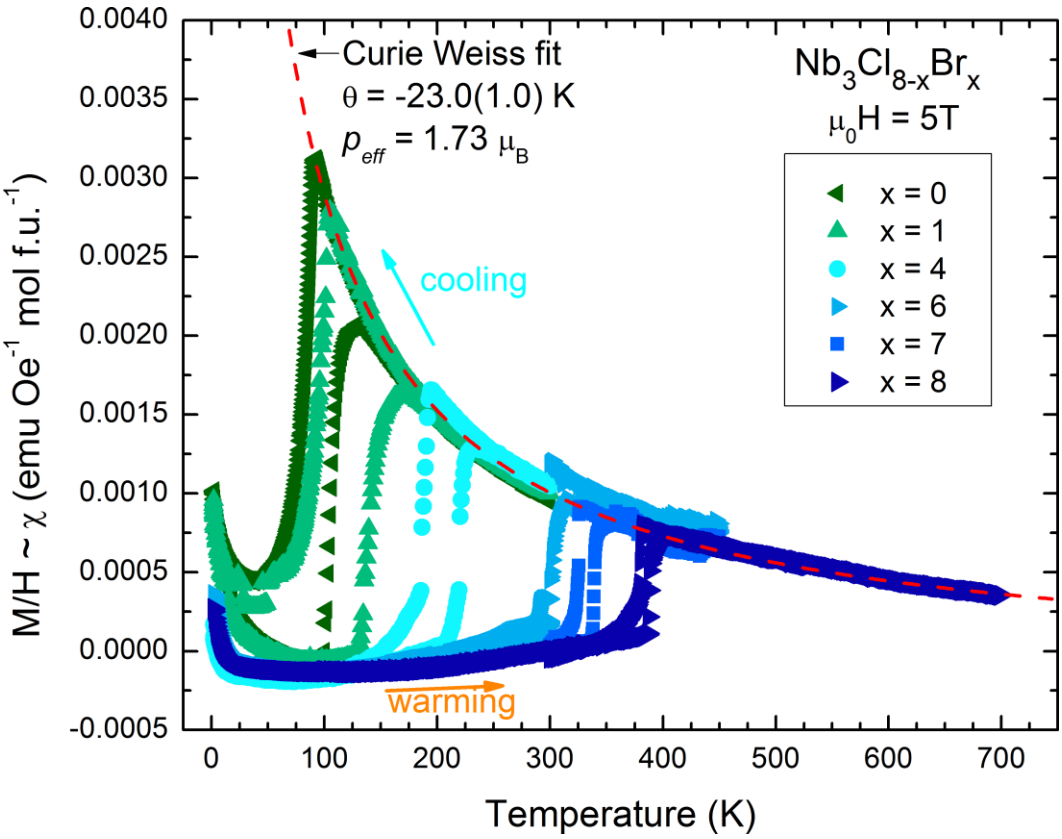

Figure 3.2.3 Magnetic susceptibility as a function of temperature for $Nb_3Cl_{8-x}Br_x$ samples from x = 0 to x = 8. Hysteresis between warming and cooling can clearly be seen and a universal curve for the paramagnetic regime is included as a dashed red line. This gives for the series a θ = -23(1) K and p_{eff} = 1.733(9) μ_B consistent with S = ½ per molecular unit.

consistent with the formation of a singlet ground state with a thermal gap to an excited triplet state. The upturn seen in the low temperature regime is attributed to a small number of defect spins from impurities, stacking faults, or edge states which account for between 0.5% and 1.7% of the high temperature spins for all samples. This was determined by fitting the Curie tail. Transition broadening was observed in samples with higher proportions of impurity spins and is typically dependent on many microscopic details including disorder.

Table 3.2.4 Hysteresis as a function of stoichiometry for $Nb_3Cl_{8-x}Br_x$. The hysteresis is defined by the difference between the temperatures at which the transition begins on warming and cooling. This is consistent with what is expected for a first order phase transition. The increased hysteresis in samples with more disorder (mixed halides), especially at transitions that occur at lower temperatures, is also consistent with the apparent mechanism of the transition as some form of mechanical shift rather than a rearrangement of chemical bonds through a breathing mode. The exact mechanism by which this occurs, especially when considering the low temperatures at which it happens in samples with high amounts of chlorine, is still being investigated.

The broadening is the temperature range over which the transition occurs once it does begin. Two samples show significant transition broadening, Nb_3Cl_8 and Nb_3Cl_7Br, The broadening is sample dependent and thus likely arises from details of the defects and disorder present[15]. All samples in which a single crystal were measured instead of an assembly of crystals show less broadening, suggesting that inconsistencies between individual crystals also plays a role in aggregate measurements.

Stoichiometry	Hysteresis (K)
x = 0	8.5 K
x = 1	27 K
x = 4	15.5 K
x = 6	15 K
x = 7	14 K
x = 8	5 K

For all compounds measured, the transition between a high temperature paramagnetic state and the low temperature state is accompanied by hysteresis, consistent with a first order phase transition, though the hysteresis of the transition is greater for mixed halides than the end members of the $Nb_3Cl_{8-x}Br_x$ family, as shown in table 3.2.4. Across the series, the temperature of the transition on warming varies nearly linearly with bromine composition as can be seen in Figure 3.2.4 (a). This demonstrates that the transition can be tuned in a predictable way by varying the stoichiometry of the compound. As previously stated, greater hysteresis is observed for the mixed halides, which could be at least partly attributable to

increased supercooling before switching phases due to uneven halide sizes increasing the resistance to structural rearrangement.

3.2.3 PXRD

To verify the sample identity, PXRD were taken on a representative sample of each composition produced in this work. Rietveld refinement was not attempted due to the difficulty in addressing the convolution of preferred orientation and stacking defects on the resulting patterns, though lattice parameters were tracked over the compositional range, the results of which can be seen in Figure 3.2.4. For samples in the α-phase at room temperature the 002 and 101 peaks were used to determine values for lattice parameters *c* and *a,* respectively. For samples in the β-phase at room temperature the 006 and 010 peaks were used to determine the lattice parameters *c* and *a* respectively. $Nb_3Cl_2Br_6$, which has a transition above room temperature on warming and below on cooling, was heated to well above its transition temperature prior to collecting PXRD data on it to ensure it would be in its α-phase.

From Figure 3.2.4 (b), it can be seen that the *a* lattice parameter, which is the same as the distance between the center of each cluster within a layer, varies linearly with substitution of bromine for chlorine. This is in very good agreement with Vegard's law which is an empirical rule that states that, at the same temperature, if the crystal structures of two compounds are the same (which is true for individual layers of $Nb_3Cl_{8-x}Br_x$), and in the absence of any other effects, then a solid solution

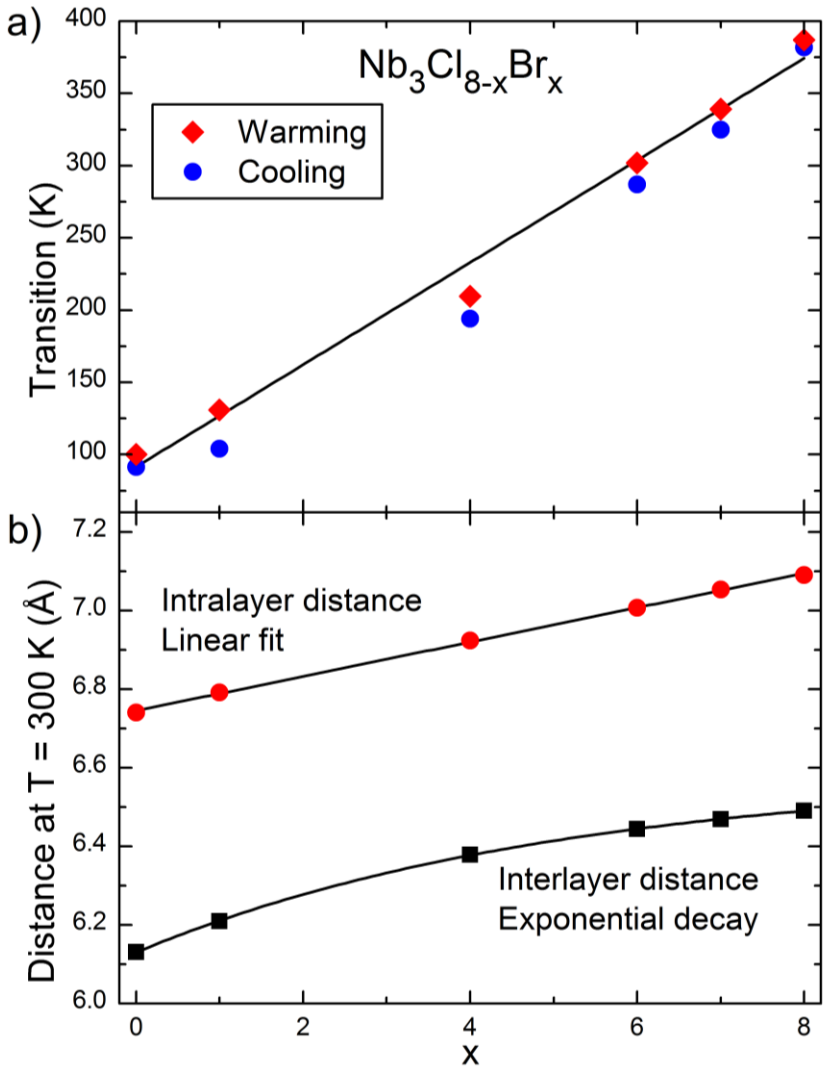

Figure 3.2.4 a) Transition temperature as a function of stoichiometry, data points mark where the transition occurs on warming (red diamonds) and cooling (blue circles). The temperature of the transition on warming is closer to linear and a line has been provided to guide the eye. b) Distance between the centers of each cluster within a layer is shown by the red circles and follows Vegard's law as shown by the included linear fit, d = 6.745(3) + 0.0436(6) x. The black squares show the average distance between layers which deviates from Vegard's Law and is best fit by an exponential decay, $d = 6.585(6) - 0.455(5)e^{(-x/5.11(12))}$. As the layers are VdW stacked this behavior is not unexpected.

of those two constituents should result in a lattice parameter that varies linearly between the end members of the series.

The average distance between layers, in the α-phase this is *c*/2 and in the beta *c*/6, deviates considerably from Vegard's law. Since these are VdW layered compounds, this is not unusual since Vegard's law only holds if there are no relevant differences between ions other than their size. Since the layers are not directly bonded to each other, the effective size of ions can change nonlinearly due to differences in polarizability of interacting ions; in particular, bromine is considerably more polarizable than chlorine. The initial bromines substituted for chlorine are constricted to an extent by the surrounding chlorines, which are less polarizable. This leaves the electronically softer bromine to distribute more of its partial charge into the gap between the fairly rigid layers to reduce strain, causing a larger than expected change in interlayer distance than if following Vegard's law. In this case, when a single bromine is substituted per unit cell, the change in *c* is twice what would be expected. As more bromine is substituted into the structure, both the *a* lattice parameter and the proportion of Br-Br interactions to Br-Cl interactions increase, resulting in a much smaller change in lattice parameter than would otherwise be expected. The difference between the change in the interlayer and intralayer distances between Nb_3Cl_8 and Nb_3Br_8 is ultimately less than 0.01 Å despite the deviations from Vegard's law for the interlayer distance of the intermediate compounds.

3.2.4 UV-Vis Spectroscopy

Crystals were exfoliated using a piece of 3M scotch tape. They were then thinned down by repeated exfoliation to average thicknesses around 200 nm, as determined through cross sectional SEM imaging of a similarly prepared sample on carbon tape. As $Nb_3Cl_2Br_6$ has a transition temperature less than room temperature (cooling) but greater than room temperature (warming), it is possible to stabilize both the high and low temperature forms in a room temperature UV-Vis measurement. This was done by placing the sample assembly in an oven at 50 °C or submerging the sample in liquid nitrogen respectively to switch between the two phases, then allowing the sample to return to room temperature before the measurement.

It was found that there were three absorbance peaks in the visible spectrum, the positions of which, for Nb_3Cl_8, are consistent with those previously re ported.[17] Peak positions appeared to be insensitive to sample thickness (between ~100 μm to ~100 nm) in experiments involving successive exfoliation. In addition to the three peaks in the visible spectrum the samples had a relatively flat absorbance background along with a broad peak centered in the UV range below the minimum wavelength that could be probed with the setup due to the opacity of 3M tape below 300 nm. To fit this background, it was assumed that the UV peak had a Gaussian form and that the three visible peaks would as well if the peak width, position and spectral weight of the UV peak were correctly defined. The UV peak and flat

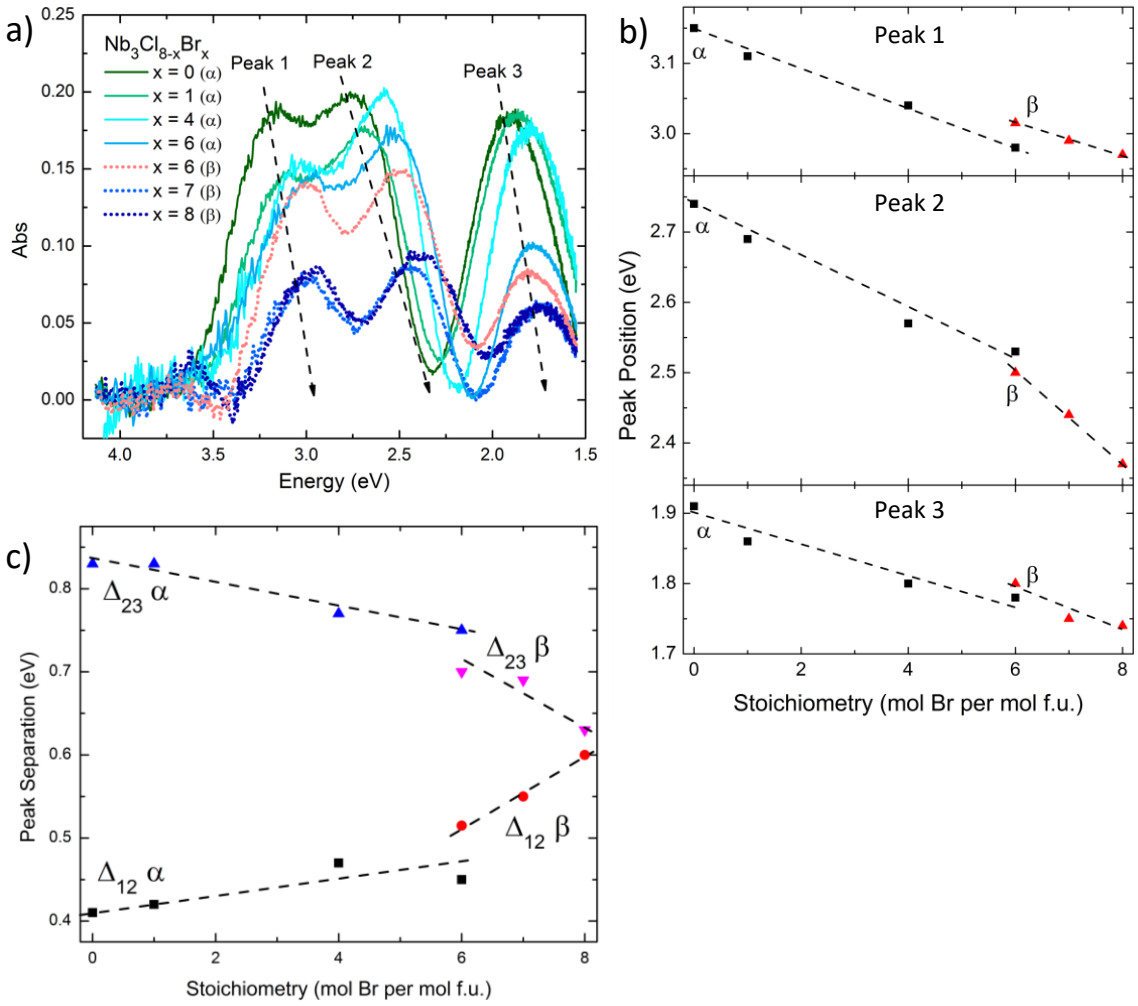

Figure 3.2.5 a) Absorbance corrected for background and a broad UV absorbance peak for the $Nb_3Cl_{8-x}Br_x$ (x = 0 to x = 8) series. Dashed lines show the general trend of peak locations with increasing x. For $Nb_3Cl_2Br_6$, which has its transition around room temperature, both the α and β phases are shown. b) Absorbance maxima for each of the three peaks in the visible range as a function of stoichiometry. Panels have been sized to provide a consistent scale for all three peaks and lines have been added to guide the eyes. c) Difference in energy of the 3 absorbance peaks in the visible spectrum as a function of stoichiometry with lines added to guide the eyes. Peak 1 is the highest energy peak while peak 3 is the lowest.

background have been subtracted out in Figure 3.2.5 (a), showing only the contribution from the peaks in the visible spectrum.

As bromine is substituted for chlorine in the structure, all three peaks continuously decrease in energy, which can be seen in Figure 6a and 6b. Upon transitioning from α-$Nb_3Cl_2Br_6$ to β-$Nb_3Cl_2Br_6$ there is a discontinuity for all three peaks, with the first and third peaks jumping to a slightly higher energy by 35 and 20 meV, respectively, and the second peak shifting to lower energies by 30 meV. The highest and lowest energy visible absorbance peaks shift in energy in a very similar way with increasing substitution, suggesting that they may be associated with a transition to or from the same band. The $Nb3X_8$ family is a multi-element compound with many band crossings at the gamma point making exact identification of the transitions difficult [72]. The middle peak is more sensitive to composition than the other two peaks, which can be seen clearly in Figure 6b as the scale for each panel is kept constant.

After the transition to the β-phase, the rate of change in the energy of the second peak as a function of stoichiometry significantly increases, while the rate of change of the first and third peaks remain effectively constant. The consequences of both the jump in the peak energies and the difference in behavior of the second peak can be seen in Figure 3.2.5 (c). In α-Nb_3Cl_8 the ratio Δ_{23}/Δ_{12} is 2.02 and in β-Nb_3Br_8 it is 1.05 as the peaks become almost equidistant from each other. Across the transition from α-$Nb_3Cl_2Br_6$ to β-$Nb_3Cl_2Br_6$ at room temperature the ratio changes from 1.67 to 1.36 as a result of the alternating direction of the discontinuity across the phase transition. There appeared to be a continuous transformation between the

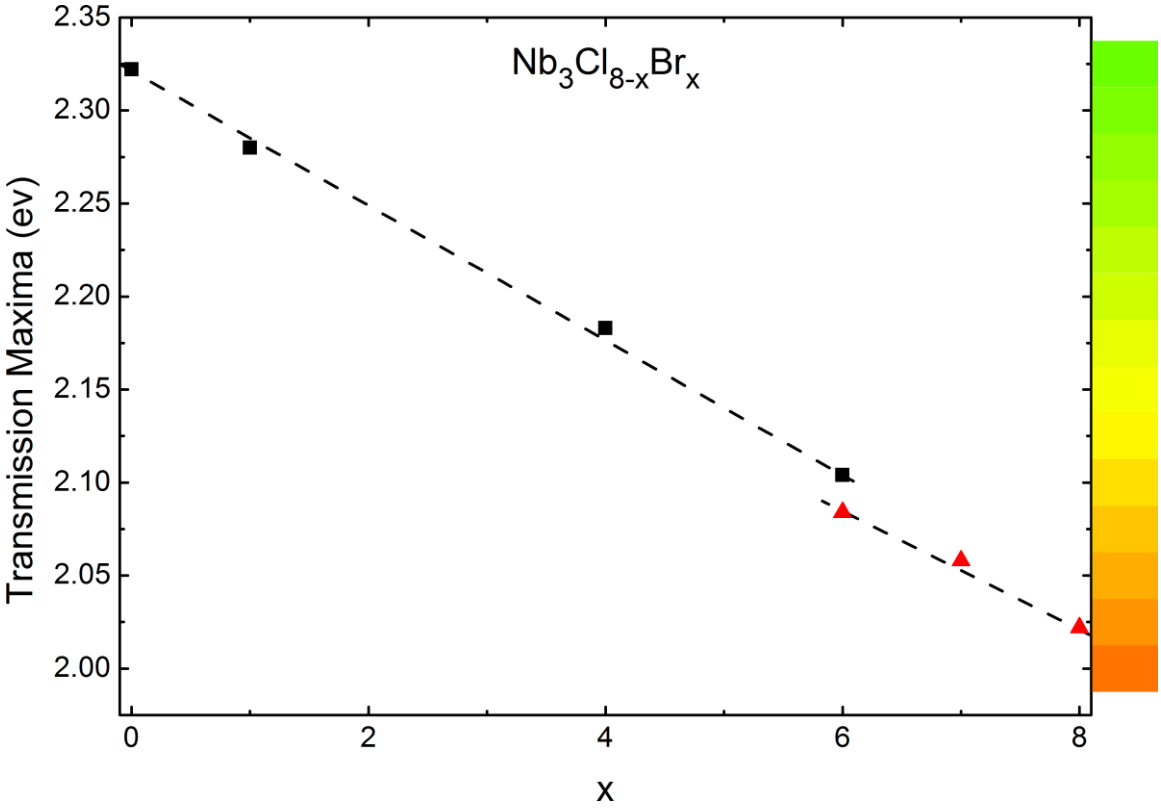

Figure 3.2.6 Location of the bulk transmission maxima for $Nb_3Cl_{8-x}Br_x$ as a function of stoichiometry. The pure color corresponding to this value is shown in the gradient.

optical absorbance of the high and low temperature phases when scanning in temperature, without major changes in absorptivity.

The actual color of the exfoliated samples appears to be primarily a function of the transmission maxima that occurs between the second and third absorbance peaks. This feature varies highly linearly with stoichiometry, as can be seen in Figure 3.2.6. This makes the value a good indicator of the stoichiometry of any given sample. This is useful in the field of device making where very thin samples are used, which may have a stoichiometry different from the average stoichiometry of crystals produced in that batch. Specifically, in the context of typical device

geometries this transmission maxima would be observed as a reflectance maxima, as can be seen in previous research on Nb_3Cl_8 which used diffuse reflectance rather than transmission to study its optical properties [72].

3.3 Conclusions

Nb_3Br_8 was found to undergo the same transition between a high temperature paramagnetic phase and a low temperature singlet ground state observed in Nb_3Cl_8. The temperature of this transition can be continuously tuned between that of the two end members by varying the Cl/Br ratio in $Nb_3Cl_{8-x}Br_x$.

There is a significant benefit to any study of the physics in the low temperature phase of this family from the fact that β-Nb_3Br_8 appears to share the same magnetic properties as β-Nb_3Cl_8. One example is that this allows us to postulate additional constraints on plausible descriptions of the character of the singlets in the low temperature phase which were not accessible when considering Nb_3Cl_8 alone. Any such descriptions should also extend to the $Nb_3Cl_{8-x}Br_x$ family as a whole. Previous works have postulated that a symmetry- breaking distortion involving localization of the diffuse $2a_1$ electron,[15] or charge disproportionation between clusters[18] might be responsible for the loss of magnetism observed in β-Nb_3Cl_8. Neither explanation seems likely when extended to include β-Nb_3Br_8, which, to the resolution limits of SXRD performed on β-Nb_3Br_8 here and in prior structural studies [68, 74] shows no apparent deviations from the ideal $R\bar{3}m$ structure, in which there is a single unique Nb site. This structure is consistent with that observed in atomic resolution STEM

imaging on β-Nb_3Br_8. Further work will be required to elucidate the nature of the low temperature singlet ground state in the context of this information.

In the context of devices, the $Nb_3Cl_{8-x}Br_x$ series of compounds possess a number of desirable features. They are 2-dimensional, readily exfoliatable semiconductors with a magnetic phase transition continuously tunable between T = 92 K and T = 387 K. The compounds are effectively air stable in the bulk on the timescale of years. In addition, the series hosts an optical bandgap continuously tunable with composition, with a small discontinuity across the transition between α and β phases when measured at room temperature. The synthesis method described in this paper allows for the rapid growth of large single crystals of any composition in the $Nb_3Cl_{8-x}Br_x$ series suitable for preparation in 2D form. Our work also demonstrates the extreme importance of heterostructure stacking sequence on physical properties in ostensibly 2D VdW layered materials.

3.4 Methods

3.4.1 Synthesis

All crystals used in this work were grown through chemical vapor transport. Stoichiometric mixtures of niobium powder (Alfa, 99.99%), $NbCl_5$ (Strem, 99.99%), and $NbBr_5$ (Strem, 99.9%) with a total mass of 1.5 grams were ground together and added to a 14 x 16 mm diameter fused silica tube in a glovebox and handled using standard air free techniques. The tubes were then sealed air free at a

length of approximately 30 centimeters, about 5 centimeters longer than the first two zones of a three-zone furnace. For Nb_3Cl_8 either 20 mg of NH_4Cl or 40 mg of $TeCl_4$ were added as a transport agent. For Nb_3Br_8 either NH_4Br or no transport agent was used with the primary difference being the overall yield of the reaction. The mixed halides were all grown with NH_4Br as the transport agent. A three-zone furnace was used with a temperature gradient of T = 840°C → 785°C → 795°C with all but the last few centimeters of the tube between the first two zones. This discouraged the formation of large intergrown clumps of crystals at the end of the tube. The furnace was held at temperature for 3-5 days before being cooled to room temperature over 7 hours.

Typical larger crystals of Nb_3Cl_8 formed with NH_4Cl as the transport agent were thin hexagonal plates with side lengths on the order of 1 cm and masses around 20 mg. Slightly thicker crystals could be obtained when using $TeCl_4$ as the transport agent, up to 40-50 mg. However, energy dispersive x-ray spectroscopy (EDS) indicated the inclusion of tellurium, likely as Nb_3TeCl_7. Most Nb_3Cl_8 crystals were smaller and growth limited by contact with other crystals being grown on the sides of the tube.

Crystals of Nb_3Br_8 are much thicker than those of Nb_3Cl_8 with a typical crystal being 2-3 mm thick. Average crystals of Nb_3Br_8 were around 60 to 100 mg with the largest crystals reaching masses around ~650 mg. Average crystal size of the

intermediate halides appeared to be continuously tuned between that of Nb_3Cl_8 and Nb_3Br_8 as a function of composition.

3.4.2 Characterization

Powder X-ray diffraction (PXRD) data were acquired at room temperature using a Bruker D8 Focus diffractometer with a LynxEye detector using Cu Kα radiation (λ = 1.5424 Å). Lattice parameters were extracted from the data using TOPAZ 4.2 (Bruker) [38].

Single crystal X-ray diffraction (SXRD) data were collected at room temperature and T = 110 K using the program CrysAlisPro (Version 1.171.36.32 Agilent Technologies, 2013) on a SuperNova diffractometer equipped with Atlas detector using graphite-monochromated Mo Kα (λ = 0.71073 Å). CrysAlisPro was also used to refine the cell dimensions and for data reduction. The temperature of the samples was controlled using the internal Oxford Instruments Cryojet. The structures were solved using SHELXS-86 and refined using SHELXL-97 [40], Visualization was done in Vesta [39].

Magnetic susceptibility data were collected using a Quantum Design Physical Properties Measurement System (PPMS) on either randomly oriented arrays of crystals using the standard option for measurements below T = 300 K, with the exception of $Nb_3Cl_2Br_6$, or perpendicular to the c-axis of single crystals using the Vibrating Sample Magnetometer (VSM) for the T < 300 K measurement of $Nb_3Cl_2Br_6$ and VSM Oven option for all measurements above T = 300 K.

SEM data were collected using a JEOL JSM IT100 scanning electron microscope at 20 keV with EDS option.

Backscattered Laue data were collected using an accelerating voltage of 15 keV and a beam diameter of 0.5 mm.

UV-Vis spectroscopy data were collected on an Agilent Technologies Cary 60 UV-Vis spectrometer.

STEM data was acquired using an aberration-corrected FEI Titan Themis operated at 300 kV. The convergence angle was 21.4 mrad and the collection inner-angle was 68 mrad. For sample preparation, flakes were first exfoliated from a bulk crystal using 3M scotch tape and transferred onto a SiO2/Si substrate. Cross-sectional samples were obtained using focused ion beam liftout. To avoid sample drift artifacts and increase signal to noise, stacks of STEM images were acquired in rapid succession (1 μs/pixel) and aligned using rigid registration methods [75].

3.5 Acknowledgements

We acknowledge stimulating discussions with Collin Broholm. We thank Maxime Siegler for assistance with SXRD measurements and analysis. We thank Hector Vivanco for assistance with collecting SEM images. Work at the Institute for Quantum Matter was supported by the U.S. Department of Energy, Office of Basic Energy Sciences, Division of Material Sciences and Engineering under Award No. DE-SC0019331. TMM acknowledges support

of the David and Lucile Packard Foundation. STEM measurements were supported by the National Sciences Foundation (NSF) through the Platform for the Accelerated Realization, Analysis, and Discovery of Interface Materials (DMR-1539918). This work made use of the Cornell Center for Materials Research Shared Facilities which are supported through the NSF MRSEC program (DMR-1719875). The FEI Titan Themis 300 was acquired through NSF-MRI-1429155, with additional support from Cornell University, the Weill Institute and the Kavli Institute at Cornell.

4. Further work on the Nb_3X_8 family of materials

4.1 Elucidating the nature of the layer rearrangement transition

4.1.1 Background

As covered in the previous section Nb_3Cl_8 and the other members of the family have a long history. The Nb_3X_8 (X = Cl, Br, I) was first reported in the 1960s over a period of a few years [66-68]. Originally only the α-phase of Nb_3Cl_8 was reported, and due to limitations in the measurements was described as a paramagnet. Two phases of Nb_3Br_8 were reported, the first defined as an α-phase which matched the observed structure of Nb_3Cl_8 and the second assigned as a β-phase which had a different stacking order. Whether the α and β-phases were linked by thermal phase transitions or were simply different polytypes of the structure were unknown. Around the same time a single phase of Nb_3I_8 was discovered, and with its structure matching that described as β-Nb_3Br_8 it was described as β-Nb_3I_8. Both Nb_3Br_8 and Nb_3I_8 were described as diamagnetic, and little more attention was paid to the family of materials for several decades with most additional work considering Nb_3X_8 complexes in solution. This changed to some extent in the 1990s when it was reported that Nb_3Cl_8 undergoes a magnetic phase transition around T = 90 K [69, 72] from a paramagnetic to diamagnetic state with an associated structural phase transition. During this phase transition layers rearrange from AB stacking to AA'BB'CC' stacking so that Nb_3 clusters in AA' directly overlap while in A'B the

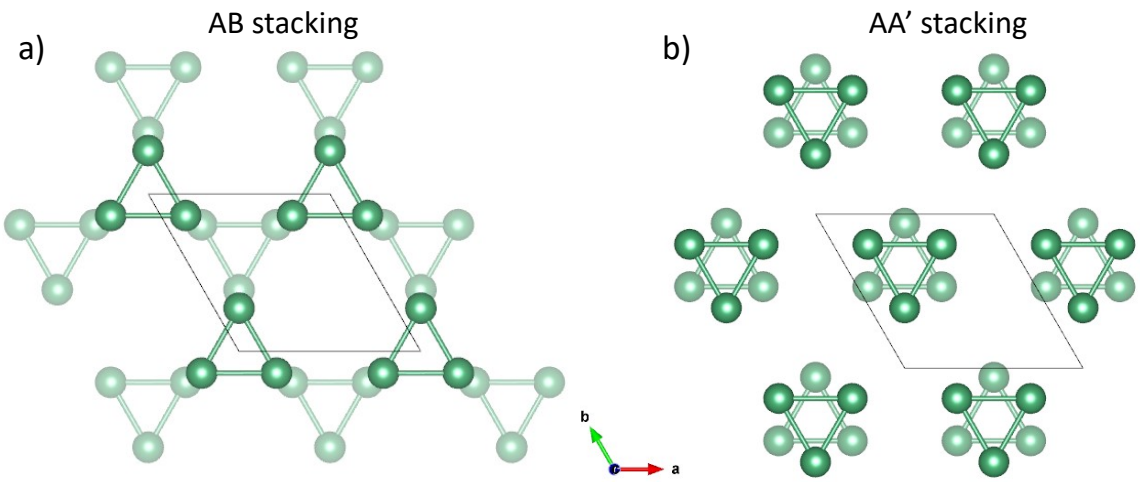

Figure 4.1.1 a) Stacking order for the α-phase, as well as for A'B layer pairs in the β-phase of Nb_3Cl_8 and Nb_3Br_8. There is no overlap of the clusters, rather they're arranged so that each cluster would map onto a point of a tetrahedra. b) The stacking arrangement for AA' layer pairs and primary structural difference between the low temperature diamagnetic phases and the high temperature paramagnetic phases. For both only the niobium atoms are shown for the sake of clarity.

layers retain the arrangement seen in the high temperature phase with each Nb_3 representing a point of a tetrahedra as seen in figure 4.1.1.

The exact identity of this low temperature structure in Nb_3Cl_8 remains contentious [70, 73], however previous models do agree on a layer stacking arrangement identical to β-Nb_3Br_8. The differences between the two previously reported low temperature structures of Nb_3Cl_8 lie in which symmetries of the standard β-phase are broken with either breaking the C_{3v} point group of the Nb_3 clusters along with a slight buckling of the halide layers to get a 3-layer *C2/m* structure [70] or breaking the rotoinversion and mirror symmetries of the $R\bar{3}m$ space group resulting in an $R3$ space group. These differences suggest potentially very different methods for relieving magnetic frustration for Nb_3Cl_8 with the first proposing either the formation of singlets between layers with the breaking of the

C_{3v} point group symmetry being incidental or the localizing the free electron between a pair of Nb ions in the Nb_3 cluster resulting in an Nb^{3+} and 2 $Nb^{2.5+}$ ions which then form one-dimensional spin singlet chains between the shortened Nb_2 pairs within the layers [70]. In both cases the magnetic exchanges would occur over unusually large length scales with interlayer singlets involving even more extreme separations (6.13 Å vs 4.01 Å) than the one-dimensional singlet chains. Despite the long distances neither is unreasonable since the exchange would be mediated either through halide bridges for the one-dimensional chains or halide-halide bridges for interlayer singlets in which case the strength of the super-exchange is determined primarily by the halide-halide bridge distance and angles (approximately 3.48 Å for LT-Nb_3Cl_8) [76], and would likely see contributions from all 3 pairs of halide ions making interlayer singlets surprisingly plausible despite the large separation distance. The second paper instead proposes charge disproportionation between clusters, transferring one electron to produce clusters of either Nb_3^{7+} or Nb_3^{9+} both of which would be diamagnetic as there are no unpaired electrons [73]. The reason this breaks the rotoinversion and *2/m* mirror symmetries is that the clusters would then have different sizes based on their charge. Because several aspects of this transition are fairly unique to the M_3X_8 family, it is important to understand how the transition actually occurs and what the ground state is. This is a prerequisite to exploring any novel physics which might exist in the system or exploiting the physical properties of either state of this system to make devices. [77, 78]

Both papers were based on the only known member of the Nb_3X_8 family to undergo a magnetic phase transition, however it has since been determined that Nb_3Br_8 also undergoes a transition between paramagnetic and diamagnetic phases, and unlike Nb_3Cl_8 its low temperature phase is not known to have any distortion from $R\bar{3}m$. Assuming that both structures relieve frustration through the same mechanism, the apparent high symmetry of the low temperature phase does not suggest that symmetry breaking was required to relieve magnetic frustration and that either one-dimensional chains or charge disproportionation between clusters inferred by symmetry breaking behavior are unlikely to explain the behavior of the overall family. From this a conclusion can be drawn that the mechanism accounting for the magnetic phase transition does not require symmetry breaking and thus that it is most likely that the non-magnetic ground state results from interlayer singlets. Though interlayer singlets would seem to be the most likely remaining answer, the distances involved in the magnetic super-exchange make it a difficult conclusion to accept without some form of direct evidence suggesting their presence.

4.1.2 Inelastic neutron scattering

Temporally, the first attempt to directly observe the presence of singlets in the ground state, whether they be one-dimensional intralayer chains, or interlayer singlets between clusters, was to attempt to observe singlet-triplet excitations in the ground state through the use of inelastic neutron scattering. At the time that inelastic neutron scattering was attempted on Nb_3Cl_8 there were no reliable estimates of the

Figure 4.1.2 Assembly to hold and co-align approximately 450 crystals for a total sample mass of around three grams. The leaves were machined from aluminum and the backs were thinned down, removing as much material as possible and leaving only a set of thicker ridges for support. Crystals on each leaf were aligned using Laue backscattering to adjust their rotation after initially being assembled on the leaves by eye, using their hexagonal symmetry as a guide. The leaves were then screwed into a custom sample holder at their base and tied together with cadmium wire. The total unshielded mass of aluminum was estimated around seven grams.

singlet to triplet excitation gap, so a range of neutron energies were selected. A magnetic feature should be observable in the inelastic spectrum as a peak at a specific energy change that decays with increasing momentum space vector Q.

Inelastic neutron scattering typically requires fairly large volumes of material, for preference in the range of several grams. This is a problem when working with Nb_3Cl_8 as due to how thin the as grown crystals are, the largest crystals are often on the order of 20 mg. In order to get a sample large enough to attempt inelastic neutron scattering on a sample holder, as shown in figure 4.1.2, had to be designed which could be used to assemble an array of approximately 450 coaligned crystals for a total of approximately three grams of Nb_3Cl_8. Crystals were attached to the leaves

of the holder with GE varnish, and cryogenic testing by lowering individual leaves of the assembly into liquid nitrogen showed no tendency for the crystals to move or detach from the sample holders. A rocking curve at the start of the experiment showed that all of the crystals were aligned with an in-plane mosaic of approximately 4 degrees (a, b axes), though a larger 8-10 degree mosaic out of plane (along c). This is within expectations as while we could adjust the rotation of the crystals within the holder, we could not adjust the angle they sat at on the holder.

In order to look for potential magnetic features the data was generally handled during the experiment as a powder averaged spectrum. This needed to be done since we did not know the correct energy range to search in and were thus looking for signatures of a magnetic transition that could be further confirmed to see if they matched the behavior and their crystallographic position in the single crystal diffraction data. High temperature intensity data with respect to Q from above the transition was subtracted from temperature corrected in order to both remove the background and highlight any changes in the spectrum from going through the transition, however there were several challenges with this process.

First because the data was taken above and below a structural transition, the energy spectrum of the phonons in the sample also shifted slightly preventing a simple background subtraction. Additionally, since the expected energy of the magnetic excitation was unknown, we collected datasets at several energy scales, looking at energy slices where something in the data might have been a feature of interest. Finally, both the large amount of aluminum in our sample holder and the

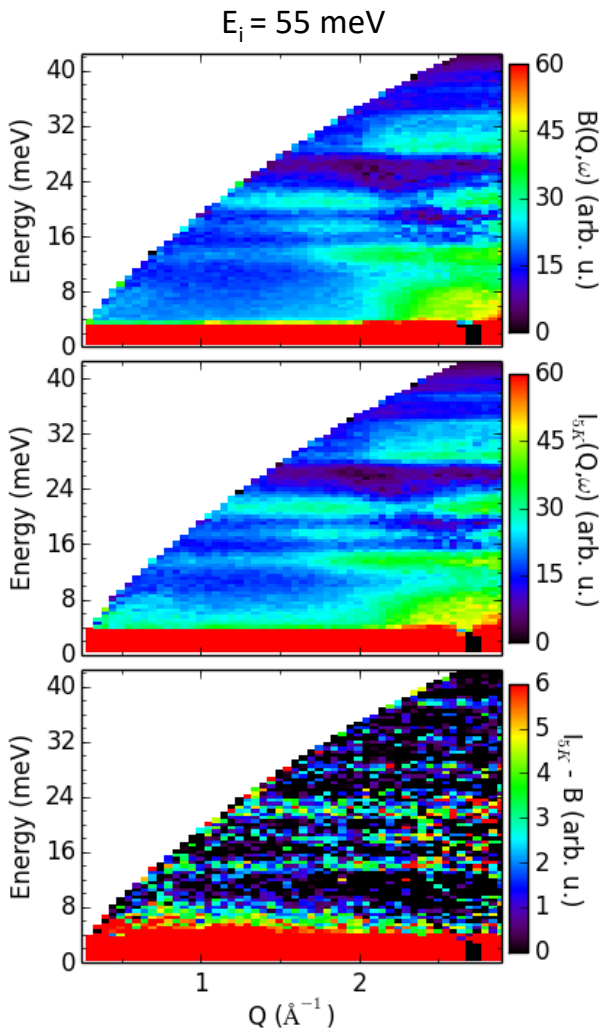

Figure 4.1.3 An example of powder averaged inelastic neutron data for an incident energy of 55 meV. At the top is the $T = 125$ K dataset, in the middle is the $T = 5$ K dataset, and at the bottom is the 5 K – corrected 125 K dataset. Due to the slight energy shift of the phonons, they can be seen clearly in the subtracted data set, making it difficult to identify any clear magnetic features.

large high incoherent scattering cross section of ^{35}Cl swamped any weak features we expected to see requiring long counting times. As a result, long counting times at each incident energy were required, and while some features might have been promising, considerable extra analysis was required to examine each one. Without a clear estimate of the singlet to triplet excitation gap the inelastic neutron scattering

data was set aside to be reexamined at a later date in concert with new data. Reanalysis of the data is underway using knowledge gained from later measurements and focusing on integrating only along special crystallographic directions to minimize the contributions of phonons and exaggerate the influence of any features the exist exclusively along those special directions.

4.1.3 Spin Peierls like ground state

One way the ground state of Nb_3X_8 might be described is like a spin Peierls state. Although none of the Nb_3X_8 materials undergo a traditional spin Peierls transition, their behavior on warming should correspond with a singlet-triplet excitation gap that can be modeled on what is observed in the spin Peirels state. In this state what should be observed for the low temperature magnetic susceptibility is an upturn upon warming before eventually reaching the structural transition, where the susceptibility should discontinuously rise to meet the paramagnetic curve of the high temperature phase. Earlier attempts to model this in Nb_3Cl_8 were hampered by the low transition temperature and apparently large gap between those states which resulted in no observable upturn in the magnetic susceptibility before reaching the transition temperature, and thus presented no good way to estimate the size of the gap through magnetic susceptibility beyond suggesting it was probably large [70].

Nb_3Br_8 was originally grown with thoughts of running a similar inelastic neutron scattering experiment on a material with a far lower incoherent scattering cross section, 5.3 barn for natural chlorine versus 0.1 barn for natural bromine.

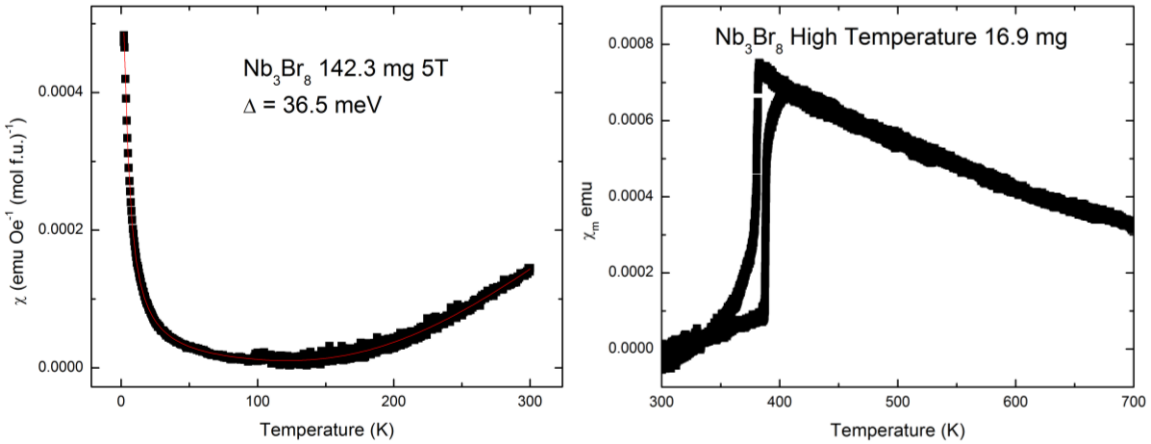

Figure 4.1.4 Magnetic susceptibility data collected for Nb_3Br_8. (Left) the data has been fit to $\chi_m = \chi_0 + C/T - C/T^2 + k\, e^{-2\Delta/T}$ to account for both the curie tail and the population of the excited magnetic state, giving an estimate for the singlet-triplet excitation gap of 36.5 meV. (Right) first high temperature measurement of magnetic susceptibility of Nb_3Br_8 revealing a familiar phase transition.

Another advantage of Nb_3Br_8 over Nb_3Cl_8 for the purposes of neutron scattering was that it was far easier to grow large crystals of, with the largest grown samples in our lab reaching masses up to 650 mg, compared to the largest Nb_3Cl_8 crystal grown of 23.1 mg which would allow a significant reduction in sample holder material contributing to the background. There was one major problem with Nb_3Br_8, namely that it wasn't known to undergo a transition like the one observed in Nb_3Cl_8. Tests of magnetic susceptibility quickly revealed Nb_3Br_8 to be far more interesting than revealing the upturn in magnetic susceptibility indicative of the thermal population of a spin triplet state from the spin singlet ground state that couldn't be seen in Nb_3Cl_8. This led to measuring the high temperature susceptibility, revealing a phase transition above room temperature that appeared to mirror the behavior of Nb_3Cl_8, all of which indicated that studying Nb_3Br_8 in parallel with Nb_3Cl_8 would aid in elucidating the underlying physics of the family as a whole. The same was

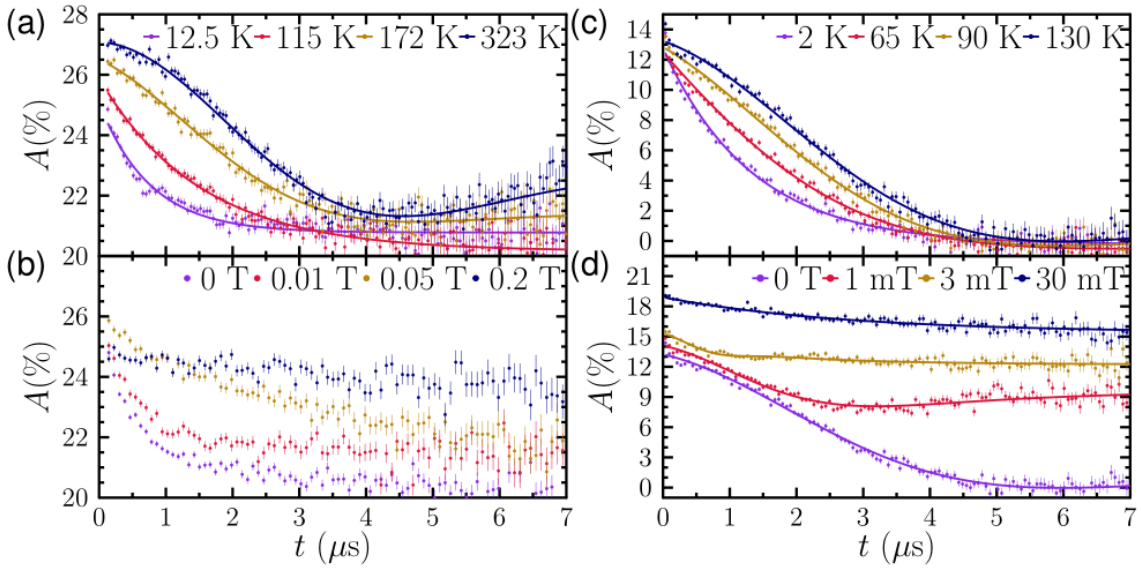

Figure 4.1.5 a) and c) show the zero-field muon asymmetry for Nb_3Br_8 and Nb_3Cl_8 respectively. Solid lines are fit to equation 12. b) and d) show the LF asymmetry of Nb_3Br_8 (well below its transition) and Nb_3Cl_8 (above its transition) respectively. The solid lines in d) represent fits to a generalization of equation 12 to include an external longitudinal field which yield excellent agreement with experimentally applied fields.

attempted for Nb_3I_8, however the material began to decompose before reaching a high temperature phase transition.

The low temperature data was best fit by an expanded version of the Curie fit for the Curie tail along with a fit for the behavior of a SP-state as:

$$\chi_m = \chi_0 + C/T - C/T^2 + k\, e^{-2\Delta/T} \qquad (11)$$

where χ_m is the molar susceptibility, χ_0 is a diamagnetic correction, C is the Curie constant, k is a constant that incorporates several additional constants, with Δ as the energy of the excitation gap in Kelvin. For Nb_3Br_8 this gave a gap of 424(5) K which corresponds to an energy of 36.5 meV. After making a solid solution series $Nb_3Cl_{8-x}Br_x$ it was found that the upturn in the low temperature data could be seen for all samples other than Nb_3Cl_8 with a minimum observed for $Nb_3Cl_4Br_4$ where

the excitation gap was 19.2 meV and the upturn began as low as $T = 75$ K. The gap began to increase again approaching Nb_3Cl_8, with the last estimate for Nb_3Cl_7Br being 20.7 meV and an upturn that began around $T = 90$ K. From this data it's estimated that the gap for Nb_3Cl_8 was likely around 21.4 meV, however it should be noted that any estimates made from magnetic susceptibility data are limited by the equations used to make the fits and are less accurate the closer the upturn is to the transition, and details such as disorder are expected to play a large role. This suggests that while Nb_3Br_8 is probably a good estimate, Nb_3Cl_7Br and Nb_3Cl_8 are probably not well estimated by this technique.

Another way to get data about a spin gap excitation is through muon spin relaxation (μSR). Both Nb_3Cl_8 and Nb_3Br_8 were measured revealing a consistent set of behaviors in which the low temperature portions of the asymmetry were dominated by rapid fluctuations described by simple exponential decay $e^{-\lambda t}$, and the high temperature portions were dominated by static spins fit by a Gaussian Kubo-Toyabe function with a width of Δ_{KT}/γ_μ. Overall, both could be fit to a combination of those regimes:

$$A(t) = A_B + A_R G(\Delta_{KT},t)e^{-\lambda t} \quad (12)$$

Above $T = 80$ K for Nb_3Cl_8 and $T = 150$ K for Nb_3Br_8 Δ_{KT} is approximately constant as can be seen in figure 4.1.6. There is no detectable change in the relaxation behavior at the structural transition in either Nb_3Cl_8 or Nb_3Br_8, rather the changes happen well below there the transition occurs. At low temperatures, the

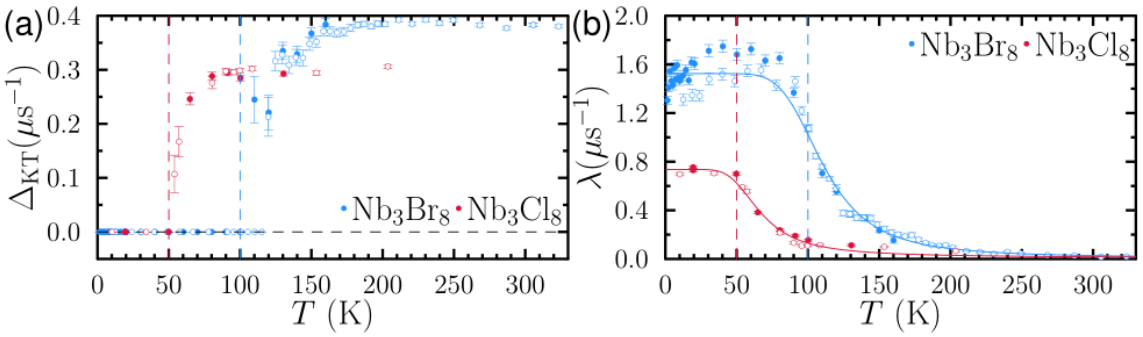

Figure 4.1.6 a) Results of fitting equation 12 to *A(t)*. The open and closed datapoints correspond to two separate experiments performed on the same sample. The solid lines in b) represent a fit to equation 13, with the vertical dashed lines indicating the temperatures below which Lorentzian relaxation dominates.

relaxation is dominated by electronic fluctuations with the relaxation rate becoming temperature independent below T = 30 K and T = 50 K respectively for the two materials, corresponding roughly with the region the curie tail begins to dominate the low temperature behavior of the materials. Another relaxation method involves spins being thermally excited across a spin gap, in which the behavior of λ can be fit to a spin-Peierls like model with the form:

$$\frac{1}{\lambda} = \frac{1}{\lambda(0)}(1 + Ce^{-2\Delta/k_B T}) \tag{13}$$

The results of this fit can be seen in figure 4.1.6 b. From this fit the temperature independent spin-excitation gap Δ can be extracted. For Nb_3Br_8 a spin gap of 32.5(3) meV is found from the μSR data, which is comparable to the 36.5 meV determined from magnetic susceptibility. The same fit applied to Nb_3Cl_8 gave a spin-excitation gap of 14.0(15) meV, considerably lower than the 21.4 meV estimated for Nb_3Cl_8, however, with fewer convoluting factors and a richer dataset,

the fit from μSR data should be considered more reliable for Nb_3Cl_8 than those from the magnetic susceptibility data.

4.1.4 Conclusions

While the identity of the spin singlets of the ground state in Nb_3Cl_8 could not be determined from the initial inelastic neutron scattering data. Further investigation into the family did however reveal useful information that may assist in pinpointing the exact energy scales of the spin-excitation gap in the various end members. The combination of both information from magnetic susceptibility and from μSR data provides guides for the reanalysis of previously collected inelastic neutron scattering data, as well as for any future investigations of the ground state of the Nb_3X_8 family. Furthermore, since Nb_3Br_8 shares the same type of transition as seen in Nb_3Cl_8, it is a good candidate to perform future scattering experiments on due to its incoherent scattering cross sections being roughly $1/50^{th}$ the size of those in natural chlorine and the ease of growing larger crystals allowing the background to be reduced and less labor-intensive alignment of those crystals. The only caveat to studying Nb_3Br_8 instead of Nb_3Cl_8 is that with a higher spin-excitation energy less of momentum space will be visible at that energy and magnetic peaks decay with Q, so it may be harder to observe that magnetic excitation peak despite the many benefits of using bromine over chlorine. An alternative plan given that caveat is to irradiate a sample of Nb_3Cl_8 in order to convert the chlorine to ^{37}Cl which has an incoherent scattering cross section of 0.001 barn as compared to the 5.3 barn of

chlorine at natural isotope abundance and should also make for much cleaner inelastic neutron scattering data, despite the additional background of the sample holder when working with the smaller Nb_3Cl_8 crystals.

4.2 Nb_3SCl_7 – A novel polar trimerized kagomé network

4.2.1 Background

The family of materials M_3QX_7 (M = Nb, Ta, Q = S, Se, Te, X = Cl, Br, I), shares a similar layer structure with Nb_3X_8 with the capping halide on the Nb_3 trimers replaced with a chalcogenide. These were originally predicted as the oxidized form of Nb_3X_8, in 1976 [79] and the first niobium version Nb_3TeBr7 was first reported in 1988 [80] with the other members of the bromides, the iodides as well as Nb_3TeCl_7 being synthesized over the course of the next decade [81-83]. The substitution of a chalcogenide for one halide ion in the structure removes the delocalized unpaired electron eliminating the $S = ½$ magnetic clusters. In 1998 it was reported that the substitution also stabilizes the tantalum versions of the structure, despite Ta_3X_8 having never been experimentally observed. There are no previous reports of Nb_3SeCl_7 or Nb_3SCl_7, however the tantalum analog Ta_3SeCl_7 was reported in 1998[83].

While the structure of each layer is generally identical to those of Nb_3X_8 compounds (with the sole exception of *o*-Nb_3SI_7), the ways in which those layers stack can be quite different. There are 7 known stacking variants for M_3QX_7 compounds, disregarding any defect stacking orders, which can either be in a

ferroelectric or antiferroelectric orientation depending on whether the capping anions alternate which side of the layer slab they are on, or if they are all on the same side of the individual layers. The α-Nb_3Cl_8 stacking type, which has an antiferroelectric orientation, is shared by all previously known M_3QCl_7 compounds and is thought to be the result of minimization of hardcore repulsion driving the stacking behavior of the chlorides which are electronically "hard" compared to the more polarizable bromides and iodides where stacking is more strongly influenced by the Madelung term [84]. From this it could be projected that the likely structures of Nb_3SeCl_7 and Nb_3SCl_7 would be naively expected to fit in this same $P\bar{3}m1$ structure type assuming the same hardcore repulsion term dominated their stacking energetics.

Whether the absence of these two niobium compounds was due to a limitation in the chemistry of these niobium systems or due to a lack of sustained synthetic effort was unknown. Answering this question helps to further establish the allowed chemistries of the niobium ternary chalcogenide halide systems and either a positive or negative result would have value in the synthetic community. This is an open question due to the typical lack of reporting negative results, though the failure to synthesize Ta_3SCl_7 was documented in the same 1998 dissertation discussing the synthesis of the other Ta_3QX_7 compounds. Meanwhile the existence of Ta_3SeCl_7 in the same report suggests that at least one of the missing Nb_3QCl_7 compounds should be accessible. As the synthetic conditions used to grow Nb_3X_8 compounds in this work are different than those previously reported and allowed the facile formation

of solid solutions of Cl/Br, an attempt was made to grow the missing Nb_3QCl_7 compounds under roughly the same conditions.

4.2.2 Experiment and Results

The only major difference in the initial conditions used for the first experiment were that the chalcogenide served as the transport agent as well as reactant, rather than incorporating NH_4X as a transport agent, to limit the scenario where the formation of the binary halide might result in off stoichiometry crystals. The first growth with a temperature gradient of 840 ºC to 785 ºC was successful in producing both single crystals of Nb_3SeCl_7 and a material which was compositionally Nb_3SCl_7 however, was not single crystalline.

The as grown Nb_3SeCl_7 was very similar in morphology to Nb_3TeCl_7 growing as thin hexagonal plates with typical dimensions of a few millimeters in each

Table 4.2.1 Refinement of SXRD data for Nb_3SeCl_7

Space group		$P\bar{3}m1$		ρ_{calc}(g/cm^3)		4.097
Color		black		Z		2
$a = b$ (Å)		6.8067 (2)		Total reflections		5939
c (Å)		12.2351(4)		Unique Reflections		850
α (°)		90		Parameters		26
β (°)		90		R_{int}		0.045
γ (°)		120		GooF		1.305
Temperature		110 K		$R(F_0)$		0.0322
Crystal Size (μm)		6x6x1		$R_w(F_o)^2$		0.0815
Atom	Site	x	y	z	U_{iso} (Å^2)	Occ.
Nb	6*i*	0.52677	0.053532	0.75109	0.00326	1
Se	2*d*	2/3	1/3	0.597245	0.00358	0.784
Cl(1)	2*d*	2/3	1/3	0.597245	0.00358	0.216
Cl(2)	2*d*	1/3	2/3	0.861636	0.00482	1
Cl(3)	6*i*	1/3	1/6	0.880571	0.00459	1
Cl(4)	6*i*	0.670690	0.835345	0.643596	0.00429	1

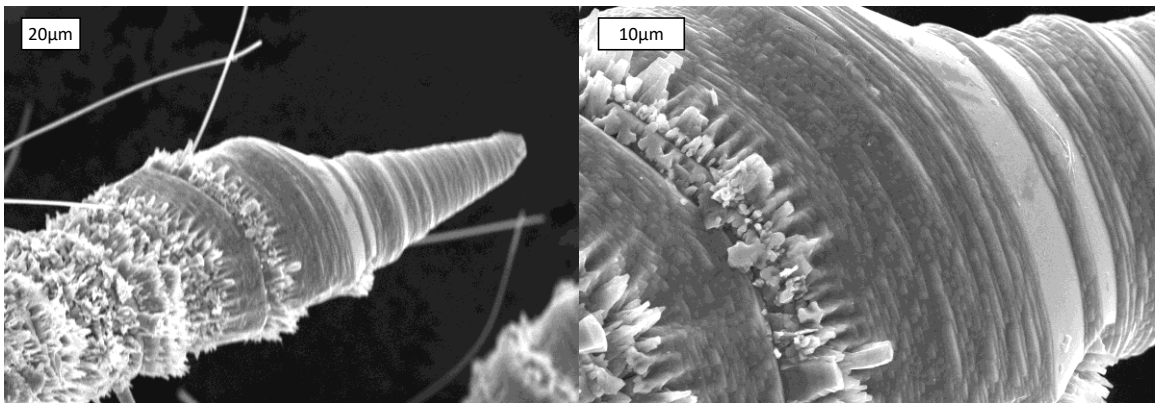

Figure 4.2.1 SEM images of Nb_3SCl_7 grown at T = 785 ºC. The spikes are made of cones stacked together, which can be most clearly seen when there is a large size mismatch between layers. Both the needles and the rough growths on the column are not Nb_3SCl_7, but are rather other Nb-S-Cl compounds likely deposited on cooling.

direction in plane and several tenths of a millimeter in thickness. Single crystal XRD revealed that it had an identical structure to Nb_3TeCl_7 as was previously expected and reported in table 4.2.1. No further attempts were made to make a variant in which the capping site was fully substituted with Se as the basic structure was identical to expectations.

$NbSCl_7$ grew only with small yields on the order of a couple tens of milligrams per growth, whereas typical yields for other M_3QX_7 compounds under the same conditions are around 500-1000 mg per growth. All initial products of Nb_3SCl_7 resembled columns of inverted cones stacked together as shown under SEM in figure 4.2.1. Attempts were made to separate out layers from the cones and flatten them to perform SXRD, which suggested that the original shape of the crystals may have been hexagonal layers stacked as a column, but this process likely induced further defects and no useable data was obtained from these initial samples.

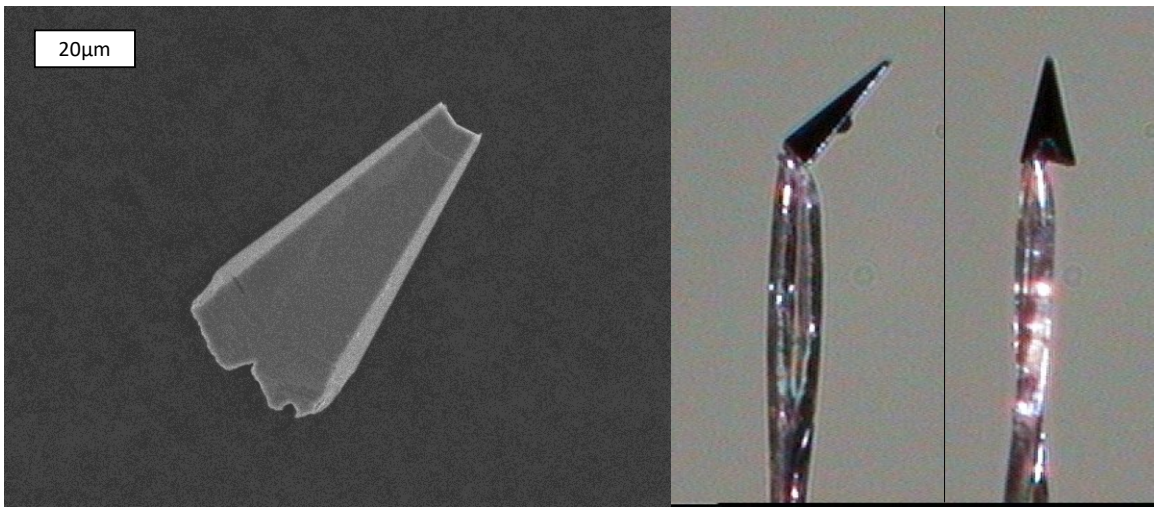

Figure 4.2.2 (left) SEM image of a Nb_3SCl_7 crystal grown at 775 ºC, though slightly damaged the characteristic kite like shape can be easily seen. (Right) Images of a Nb_3SCl_7 crystal used for SXRD.

The problem was ultimately solved by reducing the temperature of the cold zone by a further 10 ºC to 775 ºC. Although the yields weren't improved, at this temperature the result was a series of kite shaped crystals strong together from nose to tail examples of which can be seen in figure 4.2.2, rather than the typical hexagonal plates for other compounds in this series. SXRD revealed these crystals to be monoclinic in space group 8, which was unexpected, but consistent with the morphology of the as grown crystals. When considered as *Cm* the structure describes the single slab stacking order and this centering was previously used to describe the other M_3QX_7 material with this structure, however the structure was actually solved in *Im* and will be reported as such. This space group is shared by only one other M_3QX_7 compound, Ta_3SBr_7 and is one of only two possible single slab stacking types, the other of which is seen in Nb_3SBr_7. The structure itself has a ferroelectric orientation which might explain the origin of the inverted cones

Table 4.2.2 Refinement of SXRD data for Nb_3SCl_7

Space group		*Im*		ρ_{calc}(g/cm^3)	3.852
Color		black		Z	2
a (Å)		8.3561(2)		Total reflections	6787
b (Å)		6.7267(17)		Unique Reflections	2101
c (Å)		8.5016(2)		Parameters	58
α (°)		90		R_{int}	0.029
β (°)		91.653(2)		GooF	1.094
γ (°)		90		$R(F_0)$	0.0215
Temperature		110 K		$R_w(F_o)^2$	0.0550
Atom	Site	*x*	*y*	*z*	U_{iso} (Å^2)
Nb(1)	4*b*	0.2808	0.29092	0.86814	0.00410
Nb(2)	2*a*	0.572457	0	0.157828	0.00407
S	2*a*	0.859292	0	0.156785	0.00555
Cl(1)	2*a*	0.244673	1/2	0.09402	0.00870
Cl(2)	4*b*	0.494604	0.250477	0.341333	0.00468
Cl(3)	4*b*	0.574619	0.747848	0.939407	0.00494
Cl(4)	2*a*	0.265825	0	0.04206	0.00555
Cl(5)	2*a*	0.321594	0	0.68433	0.00791

observed when the material is grown at higher temperatures. This deviates from the naïve expectations of the likely space group $P\bar{3}m1$, but fits the observed pattern of sulfur resulting in different behavior from other chalcogenides in these structures.

4.2.3 Discussion

It is noted that the structure of Nb_3SCl_7 has a ferroelectric orientation of the slabs, at least in the monoclinic version of the structure that could be solved by SXRD. Two crystals from separate growths were measured, one of which had a 180º twin, and one which was untwinned. The kite shaped morphology of the crystals grown at slightly lower temperatures is very different from the morphology that led to the spikes constructed out of cones observed for the higher temperature growths. One

possible explanation for this is a high temperature ferroelectric to non-ferroelectric transition somewhere between 775 ºC and 785 ºC.

It's proposed that the high temperature non-ferroelectric structure is likely hexagonal, though it's not clear whether it would be non-polar or have an antiferroelectric orientation of the sulfur capping anions. The Nb_3 clusters should increase in separation with temperature, potentially making a large space for sulfur to pass through the clusters to migrate which side of the slabs they are on. Certain stacking polytypes of M_3QX_7 compounds tend to produce crystal morphologies better described by hexagonal pillars than flat plates as is more typical. The transition to the ferroelectric low temperature structure from a non-ferroelectric hexagonal structure would create massive transient electrostatic potentials across each slab, which could result in their warping to the observed morphology at room temperature of the materials grown at 785 ºC. Since the kite shaped crystals grown at 775 ºC do not pass through a ferroelectric transition, they aren't warped and remain highly crystalline at room temperature. The high temperature of this proposed transition makes it difficult to study directly.

References

[1] T.M. McQueen, Materials Lifecycle https://occamy.chemistry.jhu.edu/research/index.php (accessed May 1, 2020)

[2] A. Tari. *The Specific Heat of Matter at Low Temperatures*; Imperial College Press: London, (2003).

[3] N.W. Ashcroft and N.D. Mermin. *Solid State Physics;* Holt, Rinehart and Winston, (1976).

[4] I.N. Levine. *Quantum Chemistry,* 6th ed.; Pearson Education: London, (2009).

[5] D.B. Williams and B.C. Carter. *Transmission Electron Microscopy*; Springer Science: New York, (2009).

[6] L. N´eel. Influence des fluctuations du champ mol´eculaire sur les propri´et´es magn´etiques des corps. *Ann. de Physique*, **17**, 5–105, (1932).

[7] P. Anderson. Resonating valence bonds: A new kind of insulator? *Materials Research Bulletin* **8**, 153–160, (1973).

[8] G.G. Libowitz, and N.B. Hannay. *Defect Equilibria in Solids;* Springer US: New York, (1973).

[9] *Fundamentals of Quantum Materials;* Ed. J.P. Paglione, In Press. (2021)

[10] https://www.ncnr.nist.gov/resources/n-lengths/ (accessed Oct 1, 2020)

[11] *International Tables for Crystallography, Volume A, 6th Edition, Space-group Symmetry;* Ed. M.I. Aroyo, Wiley, (2017).

[12] S. Parsons. Introduction to twinning. *Acta Cryst. D* **59**, 1995-2003, (2003)

[13] P.W. Anderson. The resonating valence bond state in La2CuO4 and superconductivity. *Science* **235**, 1196 (1987).

[14] L. Balents. Spin liquids in frustrated magnets. *Nature* **464**, 199 (2010).

[15] A. Kitaev and J. Preskill. Topological Entanglement Entropy. *Phys. Rev. Lett.* **96**, 110404 (2006).

[16] M. Levin and X.G. Wen. Detecting Topological Order in a Ground State Wavefunction. *Phys. Rev. Lett.* **96**, 110405 (2006).

[17] P.A. Lee. An End to the Drought of Quantum Spin Liquids. *Science* **321**, 1306 (2008)

[18] M.R. Norman. Herbertsmithite and the Search for the Quantum Spin Liquid *Rev. Mod. Phys.* **88** 041002 (2016).

[19] P. Mendels and F. Bert. Quantum kagome frustrated antiferromagnets: one route to quantum spin liquids. *C. R. Physics* **17**, 455 (2016).

[20] M.P. Shores, E.A. Nytko, B.M. Bartlett, and D.G. Nocera. A Structurally Perfect $S = {}^1/_2$ Kagomé Antiferromagnet. *J. Am. Chem. Soc.* **127**, 13462 (2005).

[21] J.S. Helton, K. Matan, M. P. Shores, E. A. Nytko, B.M. Bartlett, Y. Yoshida, Y. Takano, A. Suslov, Y. Qiu, J.H. Chung, D.G. Nocera and Y.S. Lee. Spin Dynamics of the Spin-1/2 Kagome Lattice Antiferromagnet $ZnCu_3(OH)_6Cl_2$. *Phys. Rev. Lett.* **98**, 107204 (2007).

[22] P. Mendels, F. Bert, M.A. de Vries, A. Olariu, A. Harrison, F. Duc, J.C. Trombe, J.S. Lord, A. Amato, C. Baines. Quantum Magnetism in the Paratacamite Family: Towards an Ideal Kagomé Lattice. *Phys. Rev. Lett.* **98**, 077204 (2007).

[23] M.A. de Vries, K.V. Kamenev, W.A. Kockelmann, J. Sanchez-Benitez, and A. Harrison. Magnetic Ground State of an Experimental S = ½ Kagomé Antiferromagnet. *Phys. Rev. Lett.* **100**, 157205 (2008).

[24] S. Chu, P. Muller, D.G. Nocera, and Y.S. Lee. Clinoatacamite, paratacamite, and herbertsmithite. *Appl. Phys. Lett.* **98**, 092508 (2011).

[25] T.-H. Han, J.S. Helton, S. Chu, D.G. Nocera, J. A. Rodriguez-Rivera, C. Broholm, Y.S. Lee. Fractionalized excitations in the spin-liquid state of a kagome-lattice antiferromagnet. *Nature* **492**, 406-410 (2012).

[26] M. Fu, T. Imai, T.-H. Han, Y.S. Lee. Evidence for a Gapped Spin-Liquid Ground State in a Kagome Heisenberg Antiferromagnet. *Science* **350**, 655 (2015).

[27] J.S. Helton, K. Matan, M.P. Shores, E.A. Nytko, B.M. Bartlett, Y.Qiu, D.G. Nocera, Y.S. Lee. Dynamic Scaling in the Susceptibility of the Spin-1/2 Kagome Lattice Antiferromagnet Herbertsmithite. *Phys. Rev. Lett.* **104**, 147201 (2010).

[28] T.H. Han, M.R. Norman, J.J. Wen, J. A. Rodriguez-Rivera, J.S. Helton, C. Broholm, Y. S. Lee. Correlated impurities and intrinsic spin-liquid physics in the kagome material herbertsmithite. *Phys. Rev. B* **94**, 060409(R) (2016).

[29] D.E. Freedman, T.-H. Han, A. Prodi, P. Mueller, Q.-Z. Huang, Y.-S. Chen, S.M. Webb, Y.S. Lee, T.M. McQueen, D.G. Nocera. Site Specific X-ray Anomalous Dispersion of the Geometrically Frustrated Kagomé Magnet, Herbertsmithite, $ZnCu_3(OH)_6Cl_2$. *J. Am. Chem. Soc.* **132**, 16185-90 (2010)

[30] G.J. Nilsen, M.A. de Vries, J.R. Stewart, A. Harrison, H.M. Rønnow. Low energy spin dynamics of the s = ½ kagome system herbertsmithite. *J. Phys. Condens. Matter* **25**, 106001 (2013).

[31] T.-H. Han, J. Singleton, J.A. Schlueter. Barlowite: A Spin-1/2 Antiferromagnet with a Geometrically Perfect Kagome Motif. *Phys. Rev. Lett.* **113**, 227203 (2014).

[32] H.O. Jeschke, F. Salvat-Pujol, E. Gati, N.H. Hoang, B. Wolf, M. Lang, J.A. Schlueter, and R. Valenti. Barlowite as a canted antiferromagnet: Theory and experiment. *Phys. Rev. B* **92**, 094417 (2015).

[33] T.-H. Han, E.D. Isaacs, J.A. Schlueter, J. Singleton. Anisotropy: Spin order and magnetization of single-crystalline $Cu_4(OH)_6FBr$ barlowite. *Phys. Rev. B* **93**, 214416 (2016).

[34] D. Guterding, R. Valentí, H.O. Jeschke. Reduction of magnetic interlayer coupling in barlowite through isoelectronic substitution. *Phys. Rev. B* **94**, 125136 (2016).

[35] Z. Liu, X. Zou, J.-W. Mei, and F. Liu. Selectively doping barlowite for quantum spin liquid: A first-principles study. *Phys. Rev. B* **92**, 220102(R) (2015)

[36] Z. Feng, Z. Li, X. Meng, W. Yi, Y. Wei, J. Zhang, Y.-C. Wang, W. Jiang, Z. Liu, S. Li, Z. Y. Meng, J.-W. Mei, Y. Shi. Gapped Spin-1/2 Spinon Excitations in a New Kagome Quantum Spin Liquid Compound $Cu_3Zn(OH)_6FBr$. *Chin. Phys. Lett.* **34**, 077502 (2017)

[37] Z. Feng, Y. Wei, R. Liu, D. Yan, Y.C. Wang, J. Luo, A. Senyshyn, C. Cruz, W. Yi, J.W. Mei, Z.Y. Meng, Y. Shi, S. Li. Effect of Zn doping on the antiferromagnetism in kagome $Cu_{4-x}Zn_x(OH)_6FBr$ *arXiv*:1712.06732v1

[38] Bruker AXS (2008): TOPAS V4: General profile and structure analysis software for powder diffraction data. - User's Manual, Bruker AXS, Karlsruhe, Germany.

[39] K. Momma, VESTA: Visualization for Electronic and Structural Analysis, http://jp-minerals.org/vesta/en/

[40] G.M. Sheldrick. Crystal structure refinement with SHELXL. *Acta Cryst.* **A64**, 112 (2008).

[41] A.C. Larson, R.B. Von Dreele. General Structure Analysis System (GSAS). *Los Alamos National Laboratory Report LAUR* 86-748 (2000).

[42] B.H. Toby. EXPGUI, a graphical user interface for GSAS. *J. Appl. Cryst.* **34**, 210-213 (2001).

[43] A.J. Schultz, M.R.V. Jørgensen, X. Wang, R.L. Mikkelson, D. J. Mikkelson, V.E. Lynch, P. F. Peterson, M. L. Green, C. M. Hoffmann. Protein Crystallography at the Spallation Neutron Source. *J. Appl. Crystallogr.* **47**, 915 (2014).

[44] G. Jogl, X. Wang, S.A. Mason, A. Kovalevsky, M. Mustyakimov, Z. Fisher, C. Hoffmann, C. Kratky, P. Langan. High-resolution neutron crystallographic studies of the hydration of the coenzyme cob(II)alamin. *Acta Crystallogr.* **D67**, 584-591 (2011).

[45] J. Zikovsky, P.F. Peterson, X.P. Wang, M. Frost, C. Hoffmann. CrystalPlan: an experiment-planning tool for crystallography. *J. Appl. Crystallogr.* **44**, 418 (2011).

[46] J. Taylor, O. Arnold, J. Bilheaux, A. Buts, S. Campbell, M. Doucet, J. Zikovsky. Mantid, A high performance framework for reduction and analysis of neutron scattering data. *Bulletin of the Am. Phys. Soc.* 57 (2012).

[47] D. Mikkelson, A.J. Schultz, R. Mikkelson, T. Worlton. Integration of neutron time-of-flight single-crystal Bragg peaks in reciprocal space. *IUCr Commission on Crystallographic Computing Newsletter* **5**, pp. 32 (2005).

[48] O.Arnold, J.C.Bilheux, J.M.Borreguero, A.Buts, S.I.Campbell, L.Chapon, M.Doucet, N.Draper, R.Ferraz Leal, M.A.Gigg, V.E.Lynch, A.Markvardsen, D.J.Mikkelson, R.L.Mikkelson, R.Miller, K.Palmen, P.Parker, G.Passos, T.G.Perring, P.F.Peterson, S.Ren, M.A.Reuter, A.T.Savici, J.W.Taylor, R.J.Taylor, R.Tolchenov, W.Zhou, J.Zikovsky. Mantid – Data Analysis and Visualization

Package for Neutron Scattering and μSR. *Nucl. Instr. & methods, in Physics Research A,* **764**, 156 (2014).

[49] C.A. Schneider, W.S. Rasband, K.W. Eliceiri (2012). NIH Image to ImageJ: 25 years of image analysis. *Nature methods* **9**, 671-675 (2012).

[50] M. I. Aroyo, J. M. Perez-Mato, D. Orobengoa, E. Tasci, G. de la Flor, A. Kirov "Crystallography online: Bilbao Crystallographic Server" *Bulg. Chem. Commun.* **43(2),** 183-197 (2011).

[51] W. Petter, V. Gramlich, and F. Hulliger. The structure of $SmFe(CN)_6 \cdot 4H_2O$ and the problem of pseudo-hexagonal symmetry. *J. Solid State Chem.* **82**, 161-167 (1989).

[52] T. Malcherek, J. Schlüter. Structures of the pseudo-trigonal polymorphs of $Cu_2(OH)_3Cl$. *Acta Cryst.* **B65**, 334-341 (2009).

[53] M. Alla, E. Lippmaa. Resolution limits in magic-angle rotation NMR spectra of polycrystalline solids. *Chem. Phys. Lett.*, **87**, 30 (1982).

[54] X.G. Zheng, T. Kawae, Y. Kashitani, C.S. Li, N. Tateiwa, K. Takeda, H. Yamada, C.N. Xu, Y. Ren. Unconventional magnetic transitions in the mineral clinoatacamite $Cu_2Cl(OH)_3$. *Phys. Rev. B* **71**, 052409 (2005).

[55] J.R. Morey, K.W. Plumb, C.M. Pasco, B.A. Trump, T.M. McQueen, S.M. Koohpayeh. Growth and Characterization of Iron Scandium Sulfide ($FeSc_2S_4$). *J. Cryst. Growth* **454**, 128-33 (2016)

[56] K.E. Arpino, B.A. Trump, A.O. Scheie, T.M. McQueen, S.M. Koohpayeh. Impact of stoichiometry of $Yb_2Ti_2O_7$ on its physical properties. *Phys. Rev. B* **95**, 094407 (2017)

[57] A.R. Bassindale, M. Pourny, P.G. Taylor, M.B. Hursthouse, M.E. Light. Fluoride-ion encapsulation within a silsequioxane cage. *Angewandte Chemie* **42**, 3488-3490 (2003).

[58] S. Manzeli, D. Ovchinnikov, D. Pasquier, O.V. Yazyev, A. Kis. 2D Transition Metal Dichalcogenides. *Nat. Rev. Mat.* **2**, 17033 (2017).

[59] B. Damski, H. Gehrmann, H.-U. Everts, M. Baranov, L. Santos, M. Lewenstein. Quantum Gases in Trimerized Kagomé Lattices. *Phys. Rev. A* **72**, 053612 (2005).

[60] E. Pytte. Peierls Instability in Heisenberg Chains. *Phys. Rev. B* **10**, 4637 (1974).

[61] N. Sivada, S. Okamoto, X. Xu, C.J. Fennie, D. Xiao. Stacking-Dependent Magnetism in Bilayer CrI_3. *ACS Nano Lett.,* **18**, 7658-7664 (2018).

[62] Q. Li, M. Yang, C. Gong, R.V. Chopdekar, A.T. N'Diaye, J. Turner, G. Chen, A. Scholl, P. Shafer, E. Arenholz, A.K. Schmid, S. Wang, K. Liu, N. Gao, A.S. Admasu, S. W. Cheong, C. Hwang, J. Li, F. Wang, X. Zhang, and Z. Qiu. Patterning-Induced Ferromagnetism of Fe_3GeTe_2 Van der Waals Materials beyond Room Temperature. *ACS Nano Lett.* **18**, 5974-5980 (2018).

[63] A. Banerjee, J. Yan, J. Knolle, C. Bridges, M. Stone, M.D. Lumsden, D.G. Mandrus, D.A. Tennant, R. Moessner, S.E. Nagler. Neutron Scattering in the Proximate Quantum Spin Liquid α-$RuCl_3$. *Science* **356**, 1055-1059 (2017).

[64] J.P. Sheckelton, J.R. Neilson, D.G. Soltan, T.M. McQueen. Possible Valence-Bond Condensation in the Frustrated Cluster Magnet $LiZn_2Mo_3O_8$, *Nat. Mat.* **11**, 493-496 (2012).

[65] J. Carrasquilla, G. Chen, R.G. Melko. Tripartite Entangled Plaquette State in a Cluster Magnet. *Phys. Rev. B* **96**, 054405 (2017).

[66] H. Schäfer, H.G. Schnering. Metall-Metall-Bindungen bei niederen Halogeniden, Oxyden und Oxyhalogeniden schwerer Übergangsmetalle. *Angew. Chem.* **20**, 833 (1964).

[67] H. Schäfer, K.-D. Dohmann. Niobtetrabromid und die Niobtribromid-Phase. *Z. Anorg. Allg. Chem.* **3-4**, 134-139 (1961).

[68] A. Simon, H.G. Schnering. β-Nb_3Br_8 und β-Nb_3J_8 Darstellung, Eigenschaften und Struktur. *J. Less-Common Metals* **11**, 31 (1966).

[69] J. Kennedy, A. Simon. γ-Nb_3Cl_8 – A New Stacking Variant Formed from the Thermal Decomposition of Intercalated β'-$NaNb_3Cl_8$. *Materials Science Forum* **91-93,** 183-188 (1992).

[70] J.P. Sheckelton, K.W. Plumb, B.A. Trump, C.L. Broholm, T.M. McQueen. Rearrangement of Van der Waals Stacking and Formation of a Singlet State at T = 90 K in a Cluster Magnet. *Inorg. Chem. Front.* **4**, 481 (2017).

[71] G.J. Miller. Solid State Chemistry of Nb_3Cl_8: Nb_3TeCl_7, Mixed Crystal Formation, and Intercalation. *J. Alloys Compounds* **217**, 5-12 (1995).

[72] J.R. Kennedy, P. Adler, R. Dronskowski, A. Simon. Experimental and Theoretical Electronic Structure Investigations on α-Nb_3Cl_8 and the Intercalated Phase β'-$NaNb_3Cl_8$. *Inorg. Chem.* **35**, 2276-2282 (1996).

[73] Y. Haraguchi, C. Michioka, M. Ishikawa, Y. Nakano, H. Yamochi, H. Ueda, K. Yoshimura. Magnetic-Nonmagnetic Phase Transition with Interlayer Charge Disproportionation of Nb_3 Trimers in the Cluster Compound Nb_3Cl_8. *Inorg. Chem.* **56**, 3483-3488 (2017).

[74] K. Habermehl, G. Meyer. Triniobiumoctabromide, Nb_3Br_8, Revisited. *Z. Naturforsch.* **65b**, 770-772 (2010)

[75] B.H. Savitzky, I. El Baggari, C.B. Clement, E. Waite, B.H. Goodge, D.J. Baek, J.P. Sheckelton, C. Pasco, H. Nair, N.J. Schreiber, J. Hoffman, A.S. Admasu, J. Kim, S-W. Cheong, A. Bhattacharya, D.G. Schlom, T.M. McQueen, R. Hovden, and L.F. Kourkoutis. Image Registration of Low Signal-to-Noise Cryo-STEM Data. *Ultramicroscopy* **191**, 10.1016 (2018).

[76] L.O. Snively, G.F. Tuthill, J.E. Drumheller. Measurement and calculation of the superexcahnge interaction through the two-halid bridge in the eclipsed layered compounds $[NH_3(CH_2)_nNH_3]CuX$ for n = 2-5 and X = Cl_4 and Cl_2Br_2. *Phys. Rev. B* **24**, 9, 5349-5355 (1991).

[77] J. Jiang, Q. Liang, R. Meng, Q. Yang, C. Tan, X. Sun, X, Chen. Exploration of new ferromagnetic, semiconducting and biocompatible Nb_3X_8 (X = Cl, Br, or I) monolayers with considerable visible and infrared light absorption. *Nanoscale*, **9**, 2992-3001 (2017).

[78] J. Yoon, E. Lesne, K. Sklarek, J. Sheckelton, C. Pasco, S.S.P. Parin, T.M. McQueen, M.N. Ali. Anomalous thickness-dependent electrical conductivity in van der Waals layered transition metal halide, Nb_3Cl_8. *J. Phys.: Condens. Matter* **32**, 304004, (2020).

[79] F. Hulliger, *Structural Chemistry of the Layer-Type Phases*, Reidel, Dordecht (1976).

[80] G.J. Miller. Chemistry and properties of novel niobium cluster compounds. *J. Alloys Compounds* **229**, 1, 93-106 (1995).

[81] S. Furuseth, W. Hönle, G.J. Miller, H.-G. von Schnering, *9th Int. Conf. on Solid Compounds of Transition Elements, Abstracts,* Royal Society of Chemistry, London, 1988.

[82] G.V. Khvorykh, A.V. Shevelkov, V.A. Dolgikh and B.A. Popvkin. Niobium Thiobromide, Nb_3SBr_7, with Traingle Nb_3 Cluster: Structure and Bonding. *J. Solid State Chem.,* **120**, 311 (1995).

[83] M.D. Smith. The synthesis and characterization of new tantalum chalcogenide halide cluster compounds. (1998) *Retrospective Theses and Dissertations*. Paper 11838.

[84] J. Beck, New Forms and Functions of Tellurium: From Polycations to Metal Halide Tellurides. *Angew. Chem. Intl. Ed. Eng.*, **33**, 163 (1994).

Biography

Christopher Medard Pasco was born in Hartford, Connecticut to parents Brian and Vikki on October 31, 1990. Subsequently living in Hillsborough, Missouri, and Blythewood, SC, he graduated from Spring Valley High School in May of 2009. In September 2009 he enrolled as a freshman at The University of South Carolina as a student of chemistry and physics, ultimate receiving a degree in each in 2013. While at The University of South Carolina Chris initially contributed to a project exploring the biogenic nanowires produced by bacteria capable of reducing metals as part of their metabolism, as well as later working on printed supercapacitors incorporating carbon nanotubes and polyaniline. After a brief stint in industry Chris started his graduate studies at The Johns Hopkins University in the fall of 2014 as part of a shared student of the Broholm group and the McQueen lab. Chris's dissertation research has focused on the synthesis and characterization of two-dimensional materials with interesting magnetic properties. Chris earned his Master of Arts degree in May 2018 and his Doctor of Philosophy in December 2020 in solid-state chemistry.